PhD Thesis

An X-ray Study of Very High Energy Gamma-ray Selected Pulsar Wind Nebulae and Related Objects

Takahisa Fujinaga

Department of Physics,
Graduate School of Science and Engineering,
Tokyo Institute of Technology

12 February 2013

Abstract

Pulsar wind nebulae (PWNe) are nebulosity powered by the central pulsar through the wind of electron-positron pair plasma. Electrons are accelerated at the termination shock to relativistic speed, and radiation from them is observed as diffuse emission in a wide range of electromagnetic wave from radio through very high energy (VHE) gamma-ray bands. Recent development of ground-based Cherenkov telescopes leads to discovery of about 50 new sources in the VHE gamma-ray band especially along the Galactic plane. Because energetic particles are involved in the emission process of VHE gamma-rays, these new sources are suspected to be related to the cosmic ray acceleration sites, such as supernova remnants. In order to search for a counterpart and to study their nature, many X-ray follow-up observations have been performed so far, and unexpectedly a half of them were identified as PWNe. In this thesis, I carried out follow-up observations of two unidentified sources. Furthermore, because the two unID sources may be related to the PWNe and the nature and evolution of the PWNe are not well understood yet, I tried systematic analysis of the PWNe detected in the VHE gamma-ray band using data available in the literature.

Firstly, I studied two unidentified VHE gamma-ray sources with Suzaku. Although a long exposure was obtained for HESS J1702–420, no significant X-ray emission was detected. Thus, this source may be one of the dark particle accelerators. On the other hand, an extended X-ray source was detected at the sky region positionally coincident to HESS J1427–608. The source was identified as an X-ray counterpart of HESS J1427–608 and was designated as Suzaku J1427–6051. Considering the X-ray properties, I concluded that HESS J1427–608 may be either a PWN or a supernova remnant.

Secondly, I tried to reproduce the spectra in the X-ray and the VHE gamma-ray bands simultaneously for 16 PWNe with a model as simple as possible. The parameters of the spectra were obtained by combining available data from the literature. Many calculations of X-ray and VHE gamma-ray spectra published so far are based on a simple "one-zone" model (called "type 1" in this thesis). However, this model does not reproduce the observed spectra properly. Furthermore, most sources has smaller X-ray emission region than the VHE gamma-ray emission region, which is difficult to reproduce with the one-zone model. The size difference leads two possibilities, one is that the maximum energy of electrons is different, and the other that the magnetic field strength is different. Because I found the latter cannot reproduce the energy spectra, I adopt the former as "type 2" model, in which the maximum energy of electrons are different between the X-ray and VHE gamma-ray emission regions. However, the type 2 model did not work for a few sources. Thus, I introduced type 3 model, in which both the maximum

electron energies and the magnetic field strength are different in the two regions. As the result of the calculation, 11 sources showed good agreement with the type 2 model and two sources with the type 3 model. I had to use the type 1 model for 3 sources, because the source is not resolved in the VHE gamma-ray band. The success of the type 2 model for most of the sources means that electrons propagate with losing their energy from the termination shock. Because the X-ray emitting electrons (via synchrotron radiation) have higher energy and shorter lifetime than the VHE emitting ones (via inverse Compton scattering), X-rays are emitted from the electrons which are accelerated recently, whereas older electrons still be able to emit VHE gamma-rays. The difference of the lifetime appears as the size difference of emission regions, and the maximum energy of electrons is different for each region.

Using the obtained parameters characterizing electrons and magnetic field, and the size of emission regions, total energies of electrons and magnetic field are calculated. The magnetization parameter σ, which is expressed by the ratio of the magnetic field energy to the total electron energy, is expected to increase with the age of the PWNe. However, the estimated value showed that it has no significant correlation with the characteristic age of the central pulsar. On the other hand, I could obtain a marginal evidence that the magnetic field strength decreases with the age of PWNe. If this is true, the dark particle accelerators may be explained by old PWNe. Because most of the spin down energy of the pulsar may be accumulated in the relativistic electrons and magnetic field, calculation of these energies enables us to estimate a pulsar's initial spin period and the age. Most of the pulsars are found to have initial spin periods of $\sim 20 - 90$ ms. I finally compared the properties of the two unID sources with that of 16 PWNe, and discussed their nature in the context of the PWNe.

Contents

1 Introduction **1**

2 Review **3**

2.1 Particle Acceleration in Shock Wave . . . 3

2.2 Emission from Relativistic Particles . . . 5

2.2.1 Electrons (Leptonic Origin) . . . 5

2.2.2 Protons (Hadronic Origin) . . . 9

2.3 Pulsar Wind Nebulae . . . 11

2.3.1 Spin-down of Pulsar . . . 12

2.3.2 Pulsar Wind . . . 14

2.3.3 Emission from Pulsar Wind Nebulae . . . 16

2.4 Evolution of PWNe . . . 16

2.4.1 Size of Nebula . . . 17

2.4.2 Energy Spectra . . . 17

2.5 H.E.S.S. Survey and VHE Gamma-ray Sources on the Galactic Plane . . . 19

3 Instruments **23**

3.1 Suzaku . . . 23

3.1.1 XRT . . . 23

3.1.2 XIS . . . 26

3.1.3 HXD . . . 29

3.2 XMM-Newton . . . 30

3.2.1 X-ray telescope . . . 31

3.2.2 EPIC . . . 33

3.3 Chandra . . . 33

3.3.1 HRMA . . . 34

3.3.2 ACIS . . . 35

3.3.3 HRC . . . 36

3.4 H.E.S.S. 37
3.4.1 Telescope 37
3.4.2 Camera 38
3.5 VERITAS 39

4 X-ray Follow-up Observations of the unID VHE sources 41
4.1 HESS J1702–420 41
4.1.1 Analysis 42
4.1.2 Discussion 47
4.2 HESS J1427–608 49
4.2.1 Analysis of Suzaku 49
4.2.2 Analysis of XMM-Newton Archive Data 55
4.2.3 Discussion 57
4.3 Conclusion of These Two Follow-up Observations 60

5 X-ray and VHE Gamma-ray Spectral Analysis of PWNe 63
5.1 Properties of the VHE Gamma-ray and X-ray emitting PWNe 63
5.2 Method 66
5.3 Results 72
5.3.1 Vela X 72
5.3.2 The Crab Nebula 74
5.3.3 HESS J1356–645 76
5.3.4 HESS J1809–193 77
5.3.5 HESS J1825–137 79
5.3.6 HESS J1718–385 79
5.3.7 MSH 15–52 80
5.3.8 Kookaburra/Rabbit 82
5.3.9 Kookaburra/K3 83
5.3.10 G0.9+0.1 85
5.3.11 HESS J1837–069 85
5.3.12 HESS J1708–443 86
5.3.13 G54.1+0.3 88
5.3.14 Kes 75 90
5.3.15 HESS J1813–178 92
5.3.16 G21.5–0.9 92
5.3.17 HESS J1427–608 95
5.3.18 HESS J1702–420 96

6 Discussion **97**
6.1 Interpretation of the Type 2 and 3 Models 97
6.2 Evolution of Electron and Magnetic Field Energies 98
6.3 Evolution of Magnetic Field Strength 102
6.4 Estimation of Initial Spin Periods 104
6.5 The Two unID Sources in the Context of PWNe 106
6.5.1 HESS J1427–608 106
6.5.2 HESS J1702–420 107

7 Conclusion **109**

A Correlation Coefficient **111**
A.1 Pearson's Correlation Coefficient 111
A.2 Spearman's Rank Correlation Coefficient 111

List of Figures

2.1 A schematic view of the shock front 4
2.2 The function $F(x)$ describing the spectrum of synchrotron emission 8
2.3 Example of the gamma-ray spectra originated from relativistic protons 11
2.4 Distribution of pulsars in Galactic coordinate 12
2.5 Schematic view of magnetosphere around a pulsar 14
2.6 The multi-wavelength image of Crab nebula 15
2.7 Schematic view of a pulsar and its PWN 16
2.8 Wide-band spectral energy distribution of the Crab nebula 17
2.9 Correlation between the characteristic age and the X-ray physical size of PWNe 18
2.10 Evolution of VHE gamma-ray and X-ray luminosities of PWNe 19
2.11 The Galactic plane survey by H.E.S.S. 21

3.1 A schematic side view of Suzaku 24
3.2 An example image of a point source with the PSF and the EFF 26
3.3 Total effective area of XRT-I 26
3.4 A picture of camera body and its cross section 27
3.5 The QE curves of XIS as a function of incident X-ray energy 28
3.6 Comparison of the background spectra of X-ray CCD cameras 28
3.7 A schematic view of HXD 30
3.8 HXD background count rate as a function of energy 31
3.9 A schematic view of XMM-Newton 32
3.10 Pictures of CCDs installed to EPIC cameras 33
3.11 A schematic view of HRMA 35
3.12 Arrangement of ACIS and HRC 36
3.13 The H.E.S.S. array in Namibia 38
3.14 A schematic view of H.E.S.S. telescope 38
3.15 Mechanics of the H.E.S.S. camera 39
3.16 The telescope array of VERITAS 39

4.1 The Molongo radio image of the HESS J1702–420 field 42
4.2 XIS images of the HESS J1702–420 field 44
4.3 XIS FI spectra of HESS J1702–420 and background 1+2 46
4.4 The spectral energy distribution of HESS J1702–420 48
4.5 XIS images of the HESS J1427–608 field 50
4.6 The spectral regions for the analysis of HESS J1427–608 52
4.7 XIS spectra in the off-source region of HESS J1427–608 52
4.8 Comparison of the observed and estimated spectra 53
4.9 The radial profiles of XIS in the 2–8 keV band 54
4.10 The background-subtracted spectra of Suzaku J1427–6051 55
4.11 The summed MOS images of the HESS J1427–608 field 57
4.12 Spectral energy distribution of HESS J1427–608 59

5.1 The assumed structures of PWNe for the spectrum calculation 69
5.2 Assumed electron spectra of HESS J1837–069 71
5.3 SED of Vela X 75
5.4 SED of Crab nebula 76
5.5 SED of HESS J1356–645 77
5.6 SED of HESS J1809–193 78
5.7 SED of HESS J1825–137 80
5.8 SED of HESS J1718–385 81
5.9 SED of MSH 15–52 82
5.10 SED of Rabbit 83
5.11 SED of Kookaburra/K3 84
5.12 SED of G0.9+0.1 86
5.13 SED of HESS J1837–069 87
5.14 SED of HESS J1708–443 89
5.15 SED of G54.1+0.3 90
5.16 SED of Kes 75 91
5.17 SED of HESS J1813–178 93
5.18 SED of G21.5–0.9 94
5.19 SED of HESS J1427–608 95
5.20 SED of HESS J1702–420 96

6.1 The distribution of the total magnetic and electron energies 99
6.2 Evolution of the estimated total energies 100
6.3 σ evolution of 11 PWNe 101

6.4 Evolution of the estimated total energies as a function of $\dot{E}$ 103
6.5 Evolution of the magnetic field strength 104

List of Tables

3.1 Characteristics of Suzaku 25
3.2 Characteristics of XMM-Newton 32
3.3 Characteristics of Chanrda 34

4.1 Journal of the source and background observations 43
4.2 The best-fit parameters of the HESS J1702–420 and the background spectra . . 46
4.3 Journal of the X-ray observations pointing at HESS J1427–608 50
4.4 The best-fit parameters of the observed XIS spectrum in the off-source region . . 53
4.5 The best-fit parameters of the background-subtracted XIS spectrum 56
4.6 The best-fit parameters of EPIC spectra 58

5.1 List of sources selected for the X-ray and VHE gamma-ray analysis 65
5.2 Properties of the pulsars associated to the selected sources 66
5.3 VHE gamma-ray and X-ray properties of the selected sources 67
5.4 Summary of the assumed and obtained model parameters 73
5.5 Total energies of the electrons and magnetic field 74

6.1 Spearman's rank correlation coefficients between the energy parameters and $\tau_{\rm c}$ or $\dot{E}$ 102
6.2 Estimation of the initial rotation energy of PWNe 105
6.3 Estimation of initial spin periods 106

A.1 Example data for the estimation of Spearman's rank correlation coefficient . . . 112

Chapter 1

Introduction

A pulsar wind nebula (PWN) is a nebula surrounding an active pulsar, i.e. a rapidly spinning, highly magnetized neutron star. A rapid rotation of a neutron star in the strong magnetic field produces large electric field to accelerate electrons. The accelerated electrons produce curvature radiation, which create electron/positron pairs in the magnetic field. The pairs produce curvature radiation again; thus the numbers of pairs increase rapidly. Finally the pair plasma flows out from the magnetosphere of the neutron star at relativistic speed. The flow is thus called a pulsar wind, which collides with the ambient matter to form the termination shock. The electrons are reaccelerated and thermalized at the termination shock, and generates synchrotron radiation in the magnetic field and gamma-ray emission through inverse Compton scattering of ambient photons. However, nature of PWNe and their evolution still remain unclear. The most famous PWN, the Crab nebula, is best studied as a prototype of a young, active PWN. However, nature of other PWNe especially middle aged and old ones are not well understood yet.

Ground-based gamma-ray astronomy with the air-Cherenkov telescopes developed rapidly in these twenty years. One of such very high energy (VHE) gamma-ray telescope, High Energy Stereoscopic System (H.E.S.S.), carried out survey observations along the Galactic plane in 2000s (Aharonian et al., 2005a, 2006a). The surveys aimed to search for new cosmic ray accelerators, however, they led to the discovery of more than 50 VHE gamma-ray sources. Because of their distribution along the Galactic plane, they are considered to be located in the Milky Way Galaxy. If relativistic electrons are involved in the emission process of the gamma-rays, they can be traced through the observations of synchrotron X-ray emission. In addition, information of thermal plasma may be obtained from X-ray observation. Thus, many follow-up observations of the VHE gamma-ray sources have been performed so far. Amazingly, a half of them are identified as PWNe. They includes not only young sources (less than 10 kyr) but also old PWNe, up to $\simeq$ 100 kyr. A tenth of the VHE gamma-ray sources are classified as dark

particle accelerators, whose counterpart is not detected in other wavebands, and their nature is still unknown. On the other hand, 20 % of the sources have not been observed in the X-ray band yet. To reveal the nature of the VHE gamma-ray sources, X-ray follow-up observations for individual sources are essential.

Recently, a systematic study of PWNe selected in the VHE gamma-rays became possible because the number of identified sources and the follow-up observations have increased enough. Combining the X-ray and VHE gamma-ray spectrum, parameters of the PWNe, such as the electron density and the magnetic field strength can be estimated. These parameters are essential to understand the energy budget of the PWNe and how it changes with the evolution of the PWNe. However, past studies which combined VHE gamma-rays and X-ray observations mostly focused on individual sources. Thus, a systematic study of PWNe with the VHE gamma-ray and X-ray data combined is waited for the better understanding of the PWNe.

In this thesis, I studied two unidentified (unID) VHE gamma-ray sources with Suzaku to search for their X-ray counterparts. In addition, I performed systematic analysis of the VHE gamma-ray selected PWNe combining the X-ray data available in the literature. In chapter 2, I review the properties of PWNe and related phenomena. In chapter 3, I describe instruments used for X-ray and VHE gamma-ray observations. In chapter 4, I describe the analysis results of the two unID sources. In chapter 5, the spectral analysis of selected PWNe are summarized. The results are discussed in chapter 6. Finally, I summarize the conclusion of these studies in chapter 7.

Chapter 2

Review

In this chapter, properties of pulsar wind nebulae (PWNe) are reviewed. As electrons/positrons are accelerated to the relativistic speed in the PWNe, I first summarize the mechanism of particle acceleration in shock wave. It is followed by the explanation of emission mechanisms from relativistic particles, which coveres not only electrons but also protons for later convenience. Then, I review the characteristics of pulsars and its nebulae, based on the review by Gaensler & Slane (2006). A very high energy (VHE) gamma-ray emission is sometimes detected from a PWN. The results of the Galactic plane survey in the VHE gamma-ray band is also reviewed. Finally I give a short summary on the observational results of the evolution of PWNe.

2.1 Particle Acceleration in Shock Wave

The most plausible particle acceleration mechanism in the shock wave is the first-order Fermi acceleration (Bell, 1978). Suppose that a strong shock propagates at a supersonic velocity $v_{\rm s}$, and a particle energy is constant in the rest frame of the shock while the particle stays in the upstream or downstream regions. Figure 2.1 shows a schematic diagram of the shock front. In the rest frame of the shock, $u_{\rm u}$ is the bulk velocity of plasma in the upstream (unshocked region), while $u_{\rm d}$ is the bulk velocity of plasma in the downstream (shocked region), which is referred to as advection velocity. Let me define the energy of a relativistic particle as E_k which passed the shock from upstream to downstream and back to upstream k times. The energy increment in this process is

$$E_{k+1} = E_k \left(\frac{1 + v_{k\rm u}(u_u - u_d)\cos\theta_{k\rm u}/c^2}{1 + v_{k\rm d}(u_u - u_d)\cos\theta_{k\rm d}/c^2} \right), \tag{2.1}$$

where $v_{k\rm u}$ is the velocity at which the particle crosses from upstream to downstream with an angle $\theta_{k\rm u}$ with respect to the normal direction of the shock front, and $v_{k\rm d}$ and $\theta_{k\rm d}$ are the respective quantities for the return crossing. Assuming that the scattering is isotropic and

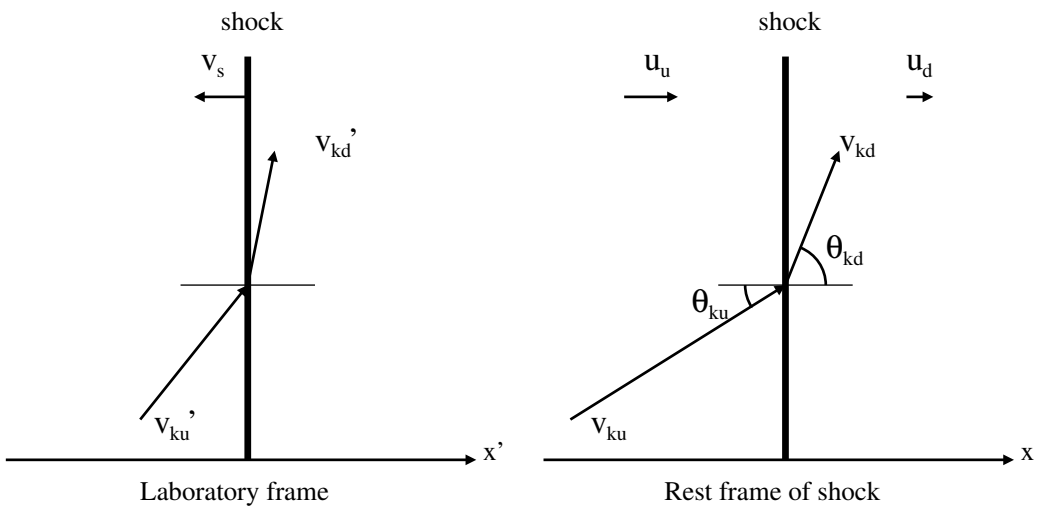

Figure 2.1: A schematic view of the shock front in laboratory frame (left) and the rest frame of the shock (right). $v_{\rm s}$ is the shock velocity. $u_{\rm u}$ and $u_{\rm d}$ is the bulk velocity in upstream and downstream, respectively. $v_{k\rm u}$ is the velocity at which the particle crosses from upstream to downstream with an angle $\theta_{k\rm u}$ with respect to the normal direction of the shock front, and $v_{k\rm d}$ and $\theta_{k\rm d}$ are the respective quantities for the return crossing.

$(u_{\rm u} - u_{\rm d}) \ll c$, the energy of a particle after n times of scattering with respect to the energy when the particle injected into the system, E_0, is

$$\begin{aligned} \ln\left(\frac{E_n}{E_0}\right) &= n\left[\ln\left(1+\frac{u_{\rm u}-u_{\rm d}}{c}\cos\theta_{k\rm u}\right) - \ln\left(1+\frac{u_{\rm u}-u_{\rm d}}{c}\cos\theta_{k\rm d}\right)\right] \\ &\simeq \frac{4}{3}n\frac{u_{\rm u}-u_{\rm d}}{c}\left[1+O\left(\frac{u_{\rm u}-u_{\rm d}}{c}\right)\right]. \end{aligned} \tag{2.2}$$

Note that E_0 is assumed to be much greater than its rest mass energy, that is, $v_{k\rm u} \sim v_{k\rm d} \sim c$.

Bell (1978) calculated the escape probability of a particle from the acceleration region for each round trip as

$$\eta = 4\frac{u_{\rm d}}{v_{\rm p}}, \tag{2.3}$$

where $v_{\rm p}$ is velocity of the particle. The probability of a particle completing at least n round trip is

$$\begin{aligned} \ln P_n &= n\ln(1-\eta) = n\ln(1-4\beta_{\rm d}) \\ &= -\left[\frac{3u_{\rm d}}{u_{\rm u}-u_{\rm d}} + O\left(\frac{u_{\rm u}-u_{\rm d}}{c}\right)\right]\ln\left(\frac{E_n}{E_0}\right). \end{aligned} \tag{2.4}$$

Note that the particle is assumed to be relativistic ($v_{\rm p} \sim c$, $\beta_{\rm d} = u_{\rm d}/v_{\rm p}$). Using equation (2.4), the differential energy spectrum is derived as

$$N(E)dE \propto E^{-\frac{u_{\rm u}+2u_{\rm d}}{u_{\rm u}-u_{\rm d}}}dE. \tag{2.5}$$

Considering the conservation of mass, energy and momentum, we obtain the relation for ideal gas of monoatomic molecules in the strong shock wave,

$$u_{\rm d} = \frac{u_{\rm u}}{4}. \tag{2.6}$$

Equation (2.5) is then

$$N(E)dE \propto E^{-2}dE. \tag{2.7}$$

The energy spectrum undergoing first-order Fermi acceleration takes a power-law with the index of $\alpha = 2$.

2.2 Emission from Relativistic Particles

In the Milky Way Galaxy, charged particles can not travel straight because of the Galactic magnetic field. Thus, we cannot obtain information of the acceleration site with the direct detection of accelerated particles. However, they radiate electromagnetic wave, whose traveling direction is not disturbed. To search for a particle accelerator, the observation of the electromagnetic wave is the most straightforward method. In this section, emission mechanism of the electromagnetic radiation from relativistic particles is reviewed.

2.2.1 Electrons (Leptonic Origin)

If relativistic electrons are present, inverse Compton (IC) scattering of low energy photons, and synchrotron emission through interstellar/circumstellar magnetic field are expected. Spectral shapes of these radiation are explained in Rybicki & Lightman (1979), which are summarized below.

Inverse Compton Scattering

We consider the Compton scattering of a single photon off a single electron. Here we show average formulas for a case of a given isotropic distribution of photons scattered by a given isotropic distribution of electrons.

Here we consider the case that the incident photon energy in the electron rest frame is significantly lower compared with the rest energy of electron, implying Thomson scattering in the rest frame (Thomson limit). The power per unit frequency emitted by each electron is given as

$$P = \frac{4}{3}\sigma_{\rm T} c \gamma^2 \beta^2 U_{\rm ph} \tag{2.8}$$

where $\sigma_{\rm T} = 8\pi r_0^2/3$ is the Thomson's cross section, $\gamma^{-1} = \sqrt{1-(v/c)^2}$ is the Lorentz factor of the electron, and $U_{\rm ph}$ is the initial photon energy density.

Particles accelerated at the shock are distributed according to a power-law distribution as explained in §2.1. Let me assume that the number density of particles with energies between E and $E + dE$ is described by a power-law distribution in the form

$$N(E)dE \propto E^{-p}dE, \tag{2.9}$$

or

$$N(\gamma)d\gamma \propto \gamma^{-p}d\gamma. \tag{2.10}$$

Suppose the incident photon field is isotropic and monoenergetic:

$$I(\epsilon) = F_0\delta(\epsilon - \epsilon_0) \tag{2.11}$$

where F_0 is the number of incident photons per unit area, per unit time per steradian. We consider only the case that electrons are relativistic, or $\beta \sim 1(\gamma \gg 1)$. Under these assumptions, the emission function is given by

$$j(\epsilon_1) = \frac{3N\sigma_{\rm T}F_0}{4\gamma^2\epsilon_0}f(x) \tag{2.12}$$

where ϵ_1 is the photon energy after scattering, and

$$f(x) \equiv \frac{2}{3}(1-x),\ 0 < x < 1, \tag{2.13}$$

where

$$x \equiv \frac{\epsilon_1}{4\gamma^2\epsilon_0}. \tag{2.14}$$

The initial photon number density $n_{\rm ph}(\epsilon)$ related to the isotropic intensity by $n_{\rm ph}(\epsilon) = 4\pi c^{-1}I(\epsilon)$. Then the total power per volume per energy resulting from the scattering of an arbitrary initial spectrum off a power-law distribution of relativistic electron is

$$\begin{aligned} \frac{dE}{dVdtd\epsilon_1} &= 4\pi\epsilon_1 j(\epsilon_1) \\ &= 3c\sigma_{\rm T}C2^{p-2}\epsilon_1^{-(p-1)/2}\int d\epsilon\ \epsilon^{(p-1)/2}n_{\rm ph}(\epsilon)\int_{x_1}^{x_2} dx\ x^{(p-1)/2}f(x), \end{aligned} \tag{2.15}$$

where $x_1 \equiv \epsilon_1/(4\gamma_1^2\epsilon)$ and $x_2 \equiv \epsilon_1/(4\gamma_2^2\epsilon)$. Integrating over all ϵ_1, we obtain the spectral index s,

$$s = \frac{p-1}{2}. \tag{2.16}$$

Thus the Compton up-scattered photons have a power-law spectrum whose index is determined by that of electrons, when the seed photons have a narrow energy distribution, e.g. a blackbody radiation, than that that of electrons.

Synchrotron Radiation

Relativistic particles interacting with a magnetic field radiate synchrotron emission. Consider the case that a particle of a mass $m_{\rm e}$ and charge q is moving at a velocity v in a uniform magnetic field B. The power per unit frequency emitted by each electron with a frequency ω is given as

$$P(\omega) = \frac{\sqrt{3}}{2\pi}\frac{q^3 B \sin\alpha}{m_{\rm e}c^2} F\left(\frac{\omega}{\omega_{\rm c}}\right), \tag{2.17}$$

and

$$\omega_{\rm c} = \frac{3\gamma^2 eB\sin\alpha}{2m_{\rm e}c}, \tag{2.18}$$

where α is the pitch angle, which is the angle between magnetic field and velocity. The function $F(x)$ is a non-dimensional function, defined as

$$F(x) \equiv x\int_x^\infty K_{\frac{5}{3}}(\eta)d\eta \tag{2.19}$$

where $K_{\frac{5}{3}}$ is the modified Bessel function of 5/3 order. Figure 2.2 plots $F(x)$ as a function of x, which has a peak at $x \simeq 0.29$. Asymptotic forms for small and large value of x are

$$F(x) \simeq \frac{4\pi}{\sqrt{3}\,\Gamma(\frac{1}{3})}\left(\frac{x}{2}\right)^{1/3},\ x \ll 1, \tag{2.20}$$

$$F(x) \simeq \left(\frac{\pi}{2}\right)^{1/2} e^{-x}x^{1/2},\ x \gg 1. \tag{2.21}$$

Integrating the power per unit frequency described in equation (2.17) over all frequencies or ω, we obtain the total power as

$$P = \frac{4}{3}\sigma_{\rm T} c\beta^2\gamma^2 U_{\rm B}, \tag{2.22}$$

where $U_{\rm B} = B^2/8\pi$ is the magnetic energy density.

Now we assume the electron energy distribution as described in equation (2.10) again, the total power per unit volume per unit frequency is given by the integral of $N(\gamma)d\gamma$ multiplied by the single particle radiation formula over all energies or γ,

$$P_{\rm tot}(\omega) \propto \int P(\omega)\gamma^{-p}d\gamma \propto \int F\left(\frac{\omega}{\omega_{\rm c}}\right)\gamma^{-p}d\gamma. \tag{2.23}$$

Let us change variables of integration to $x \equiv \omega/\omega_{\rm c}$, noting $\omega_{\rm c} \propto \gamma^2$;

$$P_{\rm tot}(\omega) \propto \omega^{-(p-1)/2}\int F(x)x^{(p-3)/2}dx. \tag{2.24}$$

As the definite integral becomes a constant, we obtain

$$P_{\rm tot}(\omega) \propto \omega^{-(p-1)/2}. \tag{2.25}$$

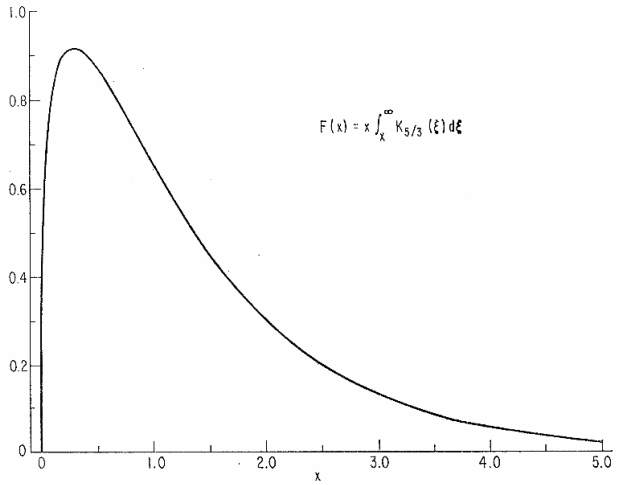

Figure 2.2: A total power spectrum of synchrotron emission as a function of $x = \omega/\omega_{\rm c}$ (Blumenthal & Gould, 1970).

Thus, the spectral index s is written with the particle distribution index p as

$$s = \frac{p-1}{2}, \tag{2.26}$$

which is same as equation (2.16).

In the X-ray and gamma-ray bands, the emission is often described as a photon-number spectrum rather than the energy spectrum, e.g.

$$N_E dE \propto E^{-\Gamma} dE, \tag{2.27}$$

where N_E is the number of photons emitted between E and $E + dE$, and $\Gamma \equiv 1 + s = (1+p)/2$ is the photon index. In this case, when $p = 2$ from equation (2.7), Γ becomes 1.5.

Electron Energy Scale

The characteristic energy of the synchrotron emission is $\epsilon_{\rm syn} \simeq \hbar\omega_{\rm c}/3$, where $\omega_{\rm c}$ is an angular frequency defined in equation (2.18). In the case of isotropic pitch angle ψ, the photon energy is

$$\epsilon_{\rm syn} \simeq 0.2\left(\frac{B}{10\ \mu{\rm G}}\right)\left(\frac{E_{\rm e}}{1\ {\rm TeV}}\right)^2\ {\rm eV}. \tag{2.28}$$

For inverse Compton scattering in the Thomson limit, the characteristic energy of IC emitted photons is $\epsilon_{\rm IC} \simeq (4/3)h\nu_0(E_{\rm e}/m_{\rm e}c^2)^2$, where $h\nu_0$ is the energy of the target photons. Thus,

$$\epsilon_{\rm IC} \simeq 5\left(\frac{h\nu_0}{10^{-3}\ {\rm eV}}\right)\left(\frac{E_{\rm e}}{1\ {\rm TeV}}\right)^2\ {\rm GeV}. \tag{2.29}$$

Solving equation (2.28) and (2.29) for the energy of electron, we obtain

$$E_{\rm e}^{\rm syn} = 70 \times \left(\frac{B}{10\ \mu{\rm G}}\right)^{-1/2} \left(\frac{\epsilon_{\rm syn}}{1\ {\rm keV}}\right)^{1/2}\ {\rm TeV}, \tag{2.30}$$

$$E_{\rm e}^{\rm IC} = 0.5 \times \left(\frac{h\nu_0}{1\ {\rm eV}}\right)^{-1/2} \left(\frac{\epsilon_{\rm IC}}{1\ {\rm TeV}}\right)^{1/2}\ {\rm TeV}. \tag{2.31}$$

If we assume the cosmic microwave background (CMB, $T = 2.7$ K) as the seed photons, the mean energy of the target photon is $h\nu_0 = kT = 6 \times 10^{-4}$ eV, thus the production of the IC gamma-ray photon of $\epsilon_{\rm IC} \simeq 1$ TeV requires the electron energy of $E_{\rm e}^{\rm IC} \simeq 20$ TeV, which is lower than that required energy of $E_{\rm e}^{\rm syn} \simeq 70$ TeV to produce a synchrotron photon of $\epsilon_{\rm syn} \simeq 1$ keV. If far-infrared photons originated from interstellar radiation field (ISRF: Porter et al. 2006) with the temperature of $\simeq 40$ K and the starlight photons with the temperature of $\simeq 5000$ K are considered as seed photons, the electron energies are required to be $E_{\rm e} \simeq 2$ TeV and 0.5 TeV in order to produce 1 TeV gamma-rays through the inverse Compton scattering, respectively.

Electron Lifetime

The lifetime of electrons in a magnetic field B and a photon field of energy density $U_{\rm ph}$, which is defined as $\tau = E_{\rm e}/P$, is

$$\begin{aligned} \tau(E_{\rm e}) &= \left(\frac{4}{3}\frac{\sigma_{\rm T} c U_0 E_{\rm e}}{m_{\rm e}^2 c^4}\right)^{-1} \\ &= 3.1 \times 10^5 \times \left(\frac{E_{\rm e}}{1\ {\rm TeV}}\right)^{-1} \left(\frac{U_0}{1\ {\rm eV\ cm^{-3}}}\right)^{-1}\ {\rm yr}, \end{aligned} \tag{2.32}$$

where $U_0 = U_{\rm B} + U_{\rm ph}$. If we assume that the target photon is CMB, the photon energy density becomes $U_{\rm ph} = 0.25$ eV cm^{-3}. In the case of low magnetic fields comparable to the interstellar magnetic field, $B \simeq 3\ \mu$G, both synchrotron and IC processes with $U_0 \simeq 0.5$ eV cm^{-3} equally contribute to the total energy loss. Typical lifetime is estimated as $\tau \simeq 30$ kyr for the electrons with the energy of $E_{\rm e}^{\rm IC} \simeq 20$ TeV, while $\tau \simeq 9$ kyr for those with the energy of $E_{\rm e}^{\rm syn} \simeq 70$ TeV.

2.2.2 Protons (Hadronic Origin)

Relativistic protons and nuclei produce high energy gamma-rays in inelastic collisions with ambient gas through the production and decay of secondary pions, kaons and hyperons. The main channel to convert the kinetic energy of protons to high energy gamma-rays is that via the neutral π^0 mesons. For the production of π^0 mesons the kinetic energy of protons should exceed

$$E_{\rm th} = 2m_\pi c^2(1 + m_\pi/4m_{\rm p}) \simeq 280\ {\rm MeV}, \tag{2.33}$$

where $m_\pi = 134.97$ MeV is the mass of the π^0 meson. The lifetime of π^0, $t_{\pi^0} = 8.4 \times 10^{-17}$ s, is significantly shorter than that of charged π mesons ($\simeq 2.6 \times 10^{-8}$ s). Thus, a neutral

pion immediately decays to two gamma-rays. In summary, gamma-rays production scheme by relativistic protons is written as:

$$\mathrm{p} + \mathrm{p} \rightarrow \pi^0 \rightarrow 2\gamma. \tag{2.34}$$

When protons have a power-law energy distribution, the differential spectrum of this radiation $J(E)$ has a distinct maximum at 100 MeV, which is shifted to $\sim$ 1 GeV in the $\nu F_\nu = E^2 J(E)$ presentation. Thus relativistic protons can produce the so-called "GeV bump" in the spectral energy distribution (SED), provided that the spectrum of protons is steeper than E^{-2}. Figure 2.3 shows the SED of π^0 decay gamma-rays calculated for power-law cosmic ray spectrum, assuming the product of the cosmic ray energy density w_p and the hydrogen column density N_H to be $w_\mathrm{p} N_\mathrm{H} = 2.5 \times 10^{22}$ eV/cm^5. The fluxes produced by protons are multiplied by a factor of 1.5 to take into account the overall contribution from nuclei both in cosmic rays and the interstellar medium. The dashed line in figure 2.3 is diffuse gamma-ray flux calculated for the local cosmic ray flux which is described by a power-law energy distribution with a spectral index of $\Gamma = 2.75$:

$$J(E) = 2.2 E_\mathrm{GeV}^{-2.75} \mathrm{cm}^{-2}\ \mathrm{s}^{-1}\ \mathrm{str}^{-1}\ \mathrm{GeV}^{-1}. \tag{2.35}$$

The dot-dashed line shows the case of a hard power-law, $\Gamma = 2.3$, for cosmic rays in the Galactic disk. The solid line indicates a steep spectrum of protons with $\Gamma \simeq 2.5$.

A cut-off in the energy spectrum of protons sometimes provides better fit to the data. Such energy spectrum of protons may be formulated as:

$$n_\mathrm{p}(E_\mathrm{p}) \propto E_\mathrm{p}^{-\Gamma_0} \left[1 + \left(\frac{E_\mathrm{p}}{E_\mathrm{cut}} \right)^\delta \right]^{-1}. \tag{2.36}$$

Below E_cut, the index is almost $\Gamma_\mathrm{p} \simeq \Gamma_0$. However, it gradually steepens to $\Gamma_\mathrm{p} \simeq \Gamma_0 + \delta$ at higher energies, $E \gg E_\mathrm{cut}$. An example of the gamma-ray spectrum due to the cut-off power-law of protons is shown in the right panel of figure 2.3.

The characteristic cooling time of relativistic protons due to inelastic pp interactions in the hydrogen medium with number density n_0 is almost independent of energy. Assuming an average cross-section at very high energy ($\sigma_\mathrm{pp} \simeq 40$ mb), and taking into account that on average the proton loses about a half of its energy per interaction ($f \simeq 0.5$), the cooling time would be

$$t_\mathrm{pp} = (n_0 \sigma_\mathrm{pp} f c)^{-1} \simeq 5.3 \times 10^7 \left(\frac{n}{1\ \mathrm{cm}^{-3}} \right)^{-1} \mathrm{yr}. \tag{2.37}$$

Since t_pp is almost energy independent above 1 GeV, where the nuclear losses well dominate over ionization losses, the initial (acceleration) spectrum of protons remains unchanged.

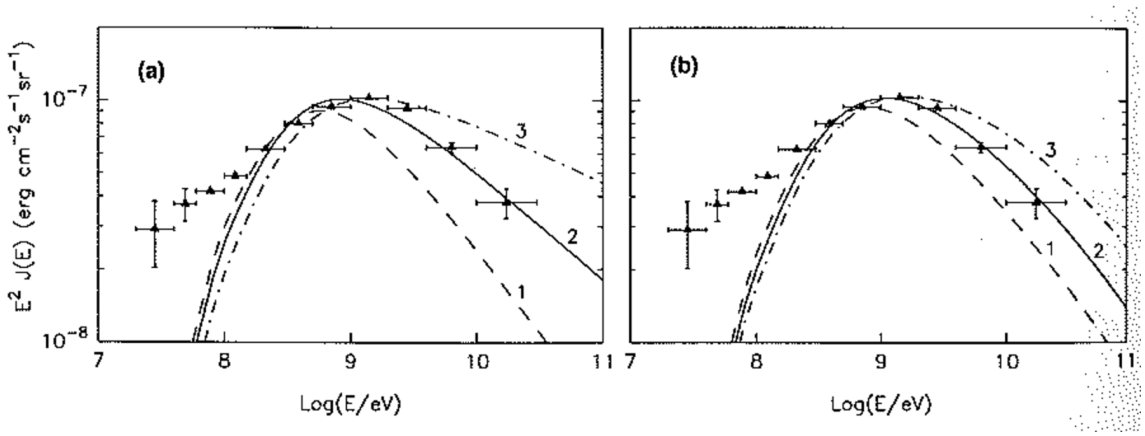

Figure 2.3: Examples of the gamma-ray spectra originated from relativistic protons, adopted from Aharonian (2004c). Left: a power-law with 3 different indices: $\Gamma_{\rm p} = 2.75$ (curve 1), 2.5 (curve 2), and 2.3 (curve 3) (see equation (2.36) for the formula of cut-off). Right: a cut-off is considered in the proton spectrum with $\Gamma_0 = 2.1$, $\delta = 0.65$, $E_{\rm cut}$ =3 GeV (curve 1), 20 GeV (curve 2), and 100 GeV (curve 3). The data points are the fluxes detected by EGRET from the inner Galaxy.

2.3 Pulsar Wind Nebulae

The most famous example of pulsar wind nebulae (PWNe) is the Crab nebula. It is certainly associated with a supernova explosion observed in 1054 (Stephenson & Green, 2002). Most of supernova remnants (SNRs) show a shell morphology (e.g. Tycho's and Kepler's SNRs). Although the Crab nebula is also born by a supernova explosion, it has a centrally filled structure at all wavelength. Thus, the Crab nebula is different from shell-type SNRs and its energetics dominated by continuous injection of magnetic fields and relativistic particles from a central source. In 1960s, 33 msec pulsations were detected from the central source of the Crab nebula in the radio and optical bands (Staelin & Reifenstein, 1968; Cocke et al., 1969), and the pulsations were shown to be slowing down at a rate of 36 nsec per a day (Richards & Comella, 1969). These observational results imply that the Crab nebula contains a rapidly rotating neutron star or "pulsar", formed in the supernova explosion in 1054. The observed rate of spin-down implies that the pulsar's rotation energy is lost at a rate of 5×10^{38} erg s^{-1}, a value similar to the inferred rate at which energy is being supplied to the nebula (Gold, 1969). Following these discovery, a theoretical understanding was developed in which the central pulsar generates a magnetized particle wind, whose ultrarelativistic electrons and positrons radiate synchrotron emission across the electromagnetic spectrum (Pacini & Salvati, 1973; Rees & Gunn, 1974). The Crab pulsar has steadily released about a third of its total rotation energy

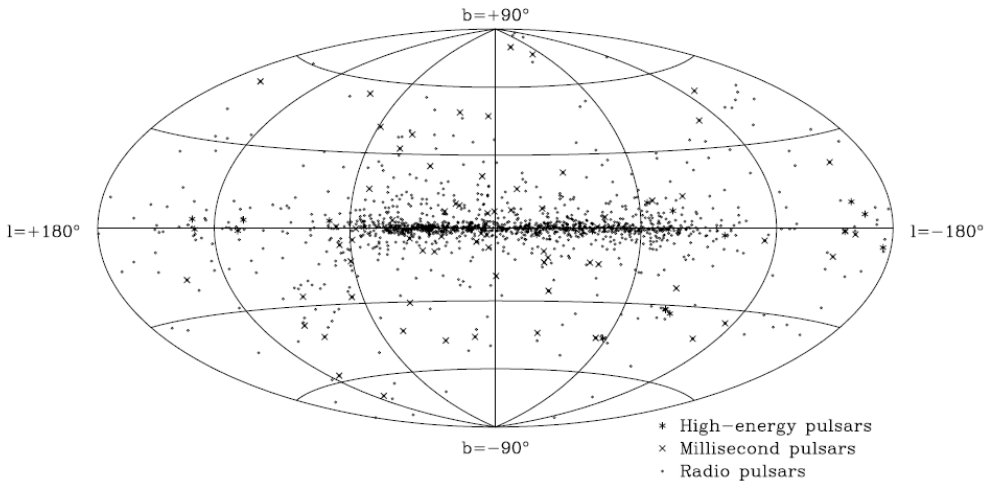

Figure 2.4: Distribution of pulsars in Galactic coordinate (Manchester et al., 2005).

of $\simeq 5 \times 10^{49}$ erg into its surrounding nebula since its birth.

In our Galaxy, observations over the past several decades have identified more than 40 sources with similar properties to those of the Crab nebula (Kaspi et al., 2006; Green, 2004). These sources are known as "pulsar wind nebulae". A PWN is sometimes surrounded by a shell-like SNR. Such an SNR is often referred to as "composite" type.

2.3.1 Spin-down of Pulsar

Neutron stars are formed through the supernova explosion of a massive star (≥ 8 $M_\odot$). They are highly compact (radius of ~ 10 km), yet having a mass comparable to the Sun (mass of $\simeq 1.4$ $M_\odot$). Pulsars are highly magnetized, rapidly rotating neutron stars, which emit beams of radiation in the energy range from radio through gamma-ray. Because the emission is observed only when the beam points to us, the signals detected are pulsed, which leads its name of "pulsar". Since the discovery of the first pulsar, the number of known pulsars has increased to more than 1600. Figure 2.4 shows the distribution of pulsars in Galactic coordinate. Most of them are young (median characteristic age of $\simeq 20$ kyr) and are concentrated along the Galactic plane (Manchester et al., 2005).

A rotation-powered pulsar is powered by the release of the neutron star's rotation energy. The energy loss causes the pulsar's spin-down. The pulsar's spin-down is described as

$$\dot{\Omega} = -k\Omega^n, \tag{2.38}$$

where n is the braking index. If we assume k to be a constant and $n \neq 1$, the age of the pulsar

is derived as (Manchester & Taylor, 1977)

$$\tau = \frac{P}{(n-1)\dot{P}}\left[1 - \left(\frac{P_0}{P}\right)^{n-1}\right], \tag{2.39}$$

where P_0 is the initial spin period of the pulsar at birth. The braking index has been measured securely only for several pulsars (e.g. Livingstone et al. 2005), in each case falling in the range $2 < n < 3$. Assuming $n = 3$, which corresponds to spin-down via magnetic dipole radiation, and $P_0 \ll P$, equation (2.39) is approximated as

$$\tau \simeq \tau_c = \frac{P}{2\dot{P}}, \tag{2.40}$$

which is called the characteristic age of a pulsar. Although equation (2.40) often overestimates the true age, it is widely used as a representative age of the pulsar. For example, the characteristic age of the Crab nebula is $\simeq 1.3$ kyr, which is close to the true age of 950 yr.

The spin-down luminosity of the pulsar, $\dot{E} = -dE_{\rm rot}/dt$, is the rate of the rotational kinetic energy loss,

$$\dot{E} = -I\Omega\dot{\Omega} = 4\pi^2 I\frac{\dot{P}}{P^3}. \tag{2.41}$$

For example, $\dot{E}$ of Crab pulsar is 5×10^{38} erg s^{-1}, which is the largest among the known pulsars. Relatively young and energetic pulsars with $\dot{E} \geq 4\times10^{33}$ erg s^{-1} acompanies prominent PWNe (Kargaltsev et al., 2008).

It is known that the energy loss rate of a pulsar can be well approximated by the magnetic dipole radiation. Using the formula of the magnetic dipole radiation, we can estimate an equatorial surface magnetic field strength as

$$B_{\rm s} = \left(\frac{3\mu_0 c^3 IP\dot{P}}{32\pi^3 R_{\rm N}^6}\right)^{1/2} = 3.2\times10^{19}\left(\frac{P}{1\ {\rm s}}\right)^{1/2}\dot{P}^{1/2}\ {\rm G}, \tag{2.42}$$

where μ_0 is the permeability of vacuum, $R_{\rm N}$ is the radius of the neutron star, and I is the neutron star's moment of inertia. Here we assume $R_{\rm N} = 10$ km and $I = 10^{45}$ g cm^2. Magnetic field strength inferred from equation (2.42) range between 10^8 G for millisecond pulsars up to $> 10^{15}$ G for magnetars. Most pulsars with prominent PWNe have inferred magnetic fields in the range 1×10^{12} to 5×10^{13} G.

A pulsar begins its life with an initial spin-down luminosity of $\dot{E}_0$. If n is constant, spin-down luminosity evolves with its age τ as (Pacini & Salvati, 1973):

$$\dot{E} = \dot{E}_0\left(1 + \frac{\tau}{\tau_0}\right)^{-\frac{n+1}{n-1}}, \tag{2.43}$$

where

$$\tau_0 \equiv \frac{P_0}{(n-1)\dot{P}_0} = \frac{2\tau_c}{n-1} - \tau \tag{2.44}$$

is the initial spin-down timescale of the pulsar.

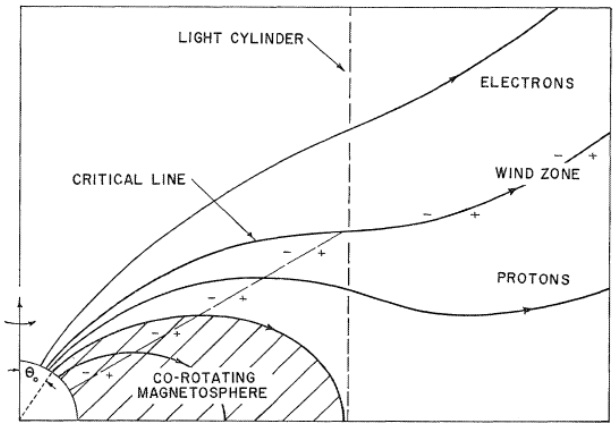

Figure 2.5: Schematic view of magnetosphere around a pulsar (Goldreich & Julian, 1969).

2.3.2 Pulsar Wind

A neutron star rotating in the strong magnetic field induces large electric field. Charged particles are accelerated by the electric field and move close to the speed of light. They move along the curved magnetic field lines, and emit gamma-rays called curvature radiation. These gamma-rays interact with surrounding magnetic field and produce electron-positron pairs. The produced electron-positron pairs are accelerated again, move along the magnetic field, and emit gamma-rays. These sequences are repeated and the electron-positron pairs flow out as an energetic pair plasma. This flow is called a pulsar wind.

Figure 2.5 shows the poloidal magnetic field structure of a pulsar. Particles confined in closed magnetic field lines corotate with the pulsar. The velocity of corotating magnetosphere with the pulsar equals the velocity of light at the light cylinder. A radius of the light cylinder is

$$R_{\rm LC} \equiv \frac{c}{\Omega} = 5 \times 10^9 \left(\frac{P}{1\ {\rm s}}\right)\ {\rm cm}, \tag{2.45}$$

where $\Omega \equiv 2\pi/P$, and the magnetic field strength at the light cylinder is given by

$$B_{\rm LC} = B_{\rm s}\left(\frac{R_{\rm N}}{R_{\rm LC}}\right)^3 = 3.0 \times 10^8 \left(\frac{P}{1\ {\rm s}}\right)^{-5} \dot{P}^{1/2}\ {\rm G}. \tag{2.46}$$

The magnetic field lines which pass through the light cylinder are open, and charged particles stream out along them as the pulsar wind.

In some of rotation powered pulsars, diffuse emission from the region surrounding the pulsar is observed as a PWN. This emission is understood to be produced by the interaction between the pulsar wind and the surrounding material. Figure 2.6 shows the Crab nebula in X-ray, optical, and radio bands surrounding the pulsar at the center of the image. Figure 2.7 shows a schematic view of a pulsar and its PWN. Because the relativistic bulk velocity of the wind

Figure 2.6: Color composite of the Crab synchrotron nebula showing Chandra X-ray image in blue, optical mosaic taken by HST in green, and radio image by VLA in red (Hester, 2008). The pulsar is seen as the bright blue point source at the center of the image.

leaving the pulsar magnetosphere is obviously supersonic with respect to the ambient medium, such a wind produces a termination shock at the distance $R_{\rm TS}$ from the pulsar where the bulk wind pressure, $P_{\rm w} \simeq \dot{E}/(4\pi c R_{\rm TS}^2)$, is equal to the ambient pressure $P_{\rm amb}$. The ambient pressure is roughly estimated as the pressure of interstellar gas. If we assume the density, and temperature of the gas as $n \sim 1$ cm^{-3} and $T \simeq 5000$ K respectively, the pressure would be $P_{\rm amb} = nRT \simeq 7\times10^{-11}$ g cm^{-2} s^{-1}, where R is the gas constant. The radius of the termination shock is estimated as

$$R_{\rm TS} \simeq \sqrt{\frac{\dot{E}}{4\pi c P_{\rm amb}}} \simeq 0.05\left(\frac{\dot{E}}{10^{36}\ {\rm erg\ s^{-1}}}\right)^{1/2}\left(\frac{P_{\rm amb}}{7\times10^{-11}\ {\rm g\ cm^{-2}\ s^{-1}}}\right)^{-1/2}\ {\rm pc}. \tag{2.47}$$

Upstream of the termination shock, particles do not radiate, but flow relativistically along with the magnetic field. At the shock, particles are thermalized and re-accelerated, producing synchrotron emission in the magnetic field and inverse Compton up-scattered photons. Particles flow in the downstream with the advection speed to the outer boundary of the nebula, where the relativistic flow is confined by the supernova remnant (Kennel & Coroniti, 1984).

The emission from PWNe is powered by pulsar's rotation energy. The wind leaving the pulsar magnetosphere is dominated by the Poynting flux, $F_{E\times B}$, with a much smaller contribution from the particle energy, $F_{\rm particle}$. The magnetization parameter σ is defined as (e.g., Kennel & Coroniti 1984):

$$\sigma \equiv \frac{F_{E\times B}}{F_{\rm particle}} = \frac{B^2}{4\pi\rho\gamma c^2}, \tag{2.48}$$

where B, ρ and γ are the magnetic field, mass density of particles, and Lorentz factor in the wind, respectively. When the wind flows from the pulsar's light cylinder, σ is typically $> 10^4$

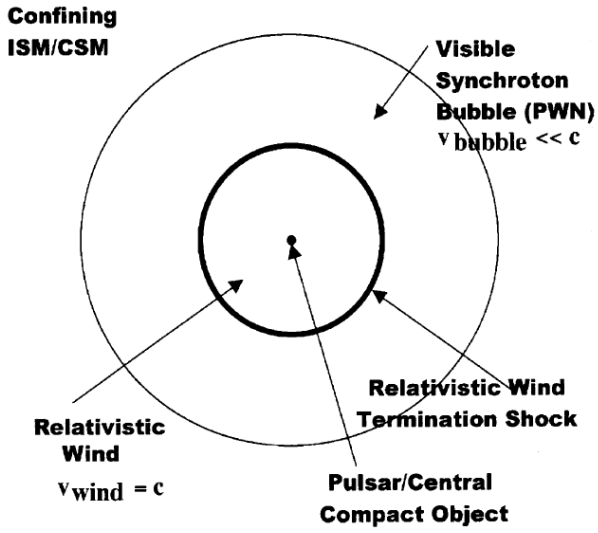

Figure 2.7: Schematic view of a PWN, for which the pulsar space velocity is small compared to the bubble's expansion speed (Arons, 2004).

(Arons, 2002). However, Crab nebula require $\sigma \ll 1$ just behind the termination shock in order to meet flow and pressure boundary conditions at the outer edge of the PWN. Between the light cylinder and the termination shock, the nature of the wind may change dramatically, although the mechanism is unclear yet (Melatos, 1998; Arons, 2002)

2.3.3 Emission from Pulsar Wind Nebulae

The electron and positron pairs are produced by the pulsar to flow out as the pulsar wind. As explained in section 2.2.1, these particles radiate synchrotron emission and IC up-scattered photons. Figure 2.8 shows the wide-band spectral energy distribution of the Crab nebula (Aharonian & Atoyan, 1998). The synchrotron and IC mechanisms provide a reasonable explanation of the overall non-thermal radiation of the Crab nebula. Compared to other PWNe, synchrotron emission of the Crab is much stronger than the Compton up-scattered emission. This is because the Crab nebula has higher magnetic field in the nebula than other PWNe. The seed photons for the IC scattering are synchrotron and far-infrared, CMB photons, in the case of the Crab nebula (Atoyan & Aharonian, 1996).

2.4 Evolution of PWNe

In this section, I review evolutions of PWNe mainly revealed from systematic studies of VHE gamma-ray and X-ray data.

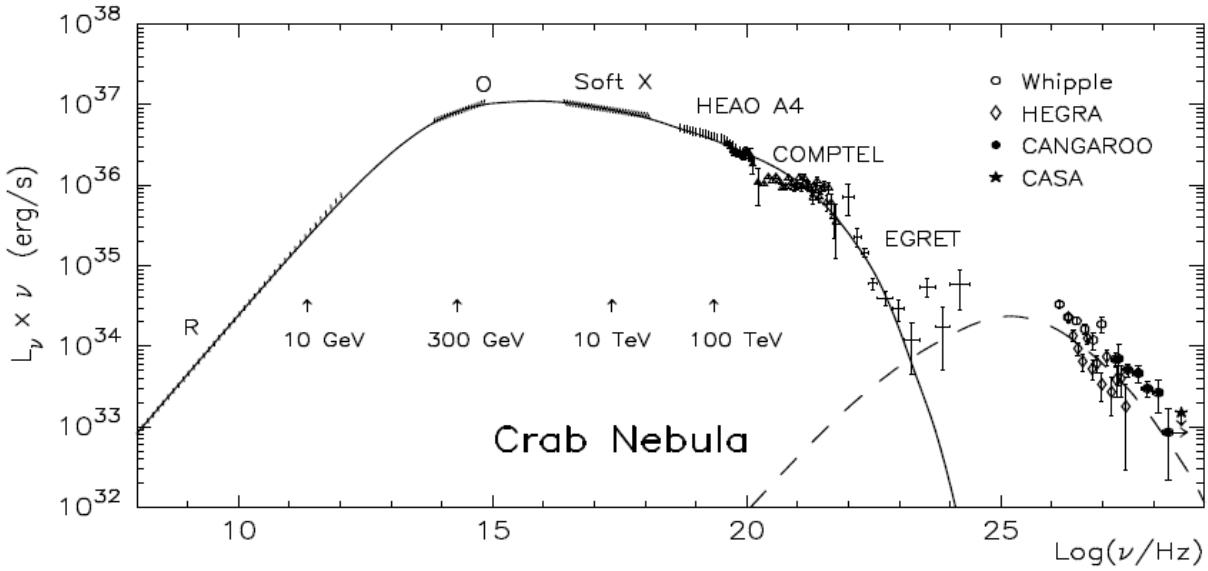

Figure 2.8: Wide-band spectral energy distribution of the Crab nebula (Aharonian & Atoyan, 1998). The solid and dashed lines correspond to the calculated synchrotron and IC radiation, respectively.

2.4.1 Size of Nebula

Recent development of imaging capabilities in both X-ray and VHE gamma-ray bands enables us to study how the size of the emission regions evolves with age. Figure 2.9 shows the correlation between the charactristic ages of host pulsars and X-ray sizes of the PWNe (Bamba et al., 2010). The X-ray nebula keeps expanding up to $\simeq$ 100 kyr. Even if the nebula is filled with a weak magnetic field of 3 μG similar to the interstellar values, the cooling time scale of electrons emitting synchrotron X-rays is only $\sim$ 10 kyr. Thus, electrons seem to escape from the PWNe without losing most energies. Such a large extent can be achieved if the magnetic field strength decays below 1 μG, or the advection speed of electrons is very fast due to large magnetization parameter of σ defined at equation (2.48).

2.4.2 Energy Spectra

Mattana et al. (2009) studied correlation between VHE gamma-ray and X-ray luminosities with the spin-down luminosity and the characteristic age. Figure 2.10 shows the correlation. The VHE gamma-ray luminosities appear correlated with neither $\dot{E}$ nor τ_c. On the other hand, X-ray luminosities show correlation with $L_{\rm X} \propto -\tau_c^{2.49}$. The flux ratio of VHE gamma-ray to X-ray also show correlation with $F_\gamma/F_{\rm X} \propto \tau_c^{2.1}$, and $F_\gamma > F_{\rm X}$ after $\simeq$ 5 kyr since the birth of pulsar. Thus, the VHE gamma-ray emission remains efficient, while X-ray luminosity decreases following the

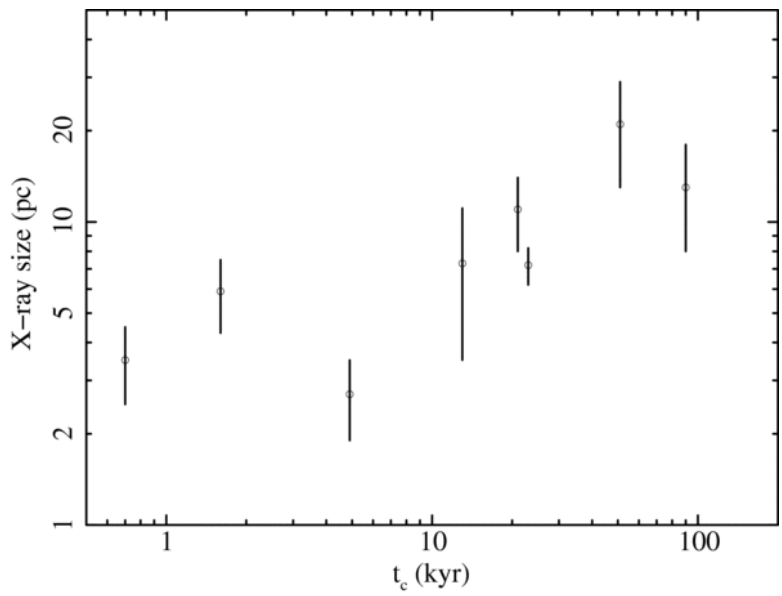

Figure 2.9: Correlation between the characteristic age of pulsar t_c and the X-ray physical size of PWNe above 2 keV. Adopted from Bamba et al. (2010).

pulsar's spin-down. Considering these results, two regime of electrons are necessary, which are named "cooled" and "uncooled". As reviewed in section 2.2.1, VHE gamma-ray is produced by long-lived electrons ("uncooled"), whereas X-ray is by younger electrons ("cooled") injected in the last thousands of years. After $\simeq$ 10 kyr since its birth, the difference of electron population may reflect the evolution of VHE gamma-ray and X-ray emission.

Tanaka & Takahara (2010, 2011) modeled evolution of spectral energy distribution for young PWNe ($\leq$ 10 kyr). They solved evolution of the particle distribution considering time-dependent injection from the pulsar and cooling by radiative and adiabatic losses. Also they assumed the shape of the nebula is a uniform sphere expanding at a constant velocity, and then the magnetic field strength depends on the radius of the nebula and the pulsar's spin-down luminosity. The constructed model is applied to the 5 PWNe including Crab nebula, and the calculated spectrum shows good agreement with the observational data from radio to VHE gamma-ray. The spectral evolution also shows that the flux ratio of VHE gamma-ray to X-ray increases with time. They concluded the increase of the flux ratio is because the magnetic field strength decreases with time, not because of the rapid cooling of X-ray emitting electrons. However, their model is difficult to apply to PWNe older than $\simeq$ 10 kyr because the size of VHE gamma-ray and X-ray emission regions should not be approximated to be same.

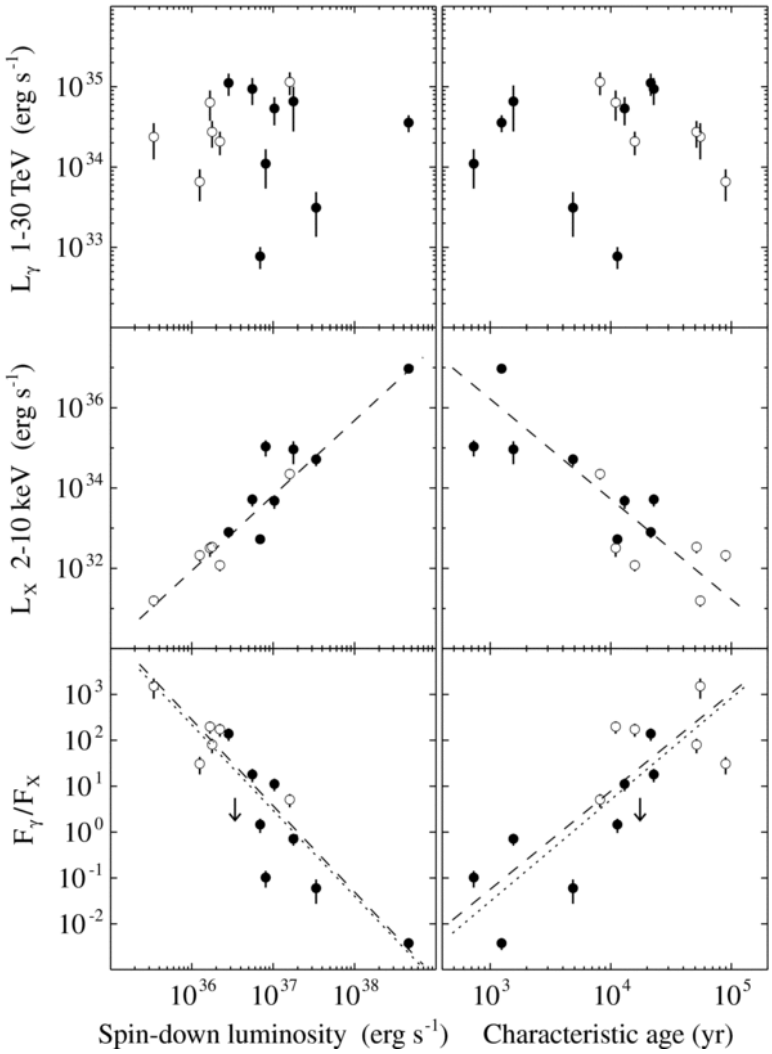

Figure 2.10: VHE gamma-ray luminosity, X-ray luminosity, and VHE gamma-ray to X-ray flux ratio versus pulsar's spin-down luminosity (left column), and characteristic age (right column). Filled and open circles indicate identified and candidate PWNe, respectively. Adopted from Mattana et al. (2009).

2.5 H.E.S.S. Survey and VHE Gamma-ray Sources on the Galactic Plane

In the 1980s, a ground-based gamma-ray imaging telescope was constructed, named Whipple Observatory. The telescope detected gamma-ray signal from the Crab Nebula for the first time in 1989 (Weekes et al., 1989). Since the detection, ground-based technique has improved to be the most successful approach in the gamma-ray astronomy. It is based on the detection of the Cherenkov light produced by photon, which initiate cascades in the Earth's atmosphere. This technique can also reject a large fraction of the cosmic ray background based on the shape of

the Cherenkov images. Multiple Cherenkov telescopes allows stereoscopic reconstruction of the shower, which provides a further breakthrough in sensitivity and angular resolution.

High Energy Stereoscopic System (H.E.S.S.) is a system of four imaging atmospheric Cherenkov telescopes located in the Khomas highlands of Namibia. Until the completion of H.E.S.S. in early 2004, no VHE gamma-ray survey of comparable sensitivity of the southern sky of the central region of the Galaxy had been performed.

The Galactic plane survey with H.E.S.S. revealed the presence of tens of new VHE gamma-ray sources (Aharonian et al., 2005a, 2006a). This survey covers essentially the whole inner Galaxy: $-85° < l < 60°$, $-2.5° < b < 2.5°$, while the positive Galactic latitude extent of this survey is limited by zenith angle constraints. Figure 2.11 shows the detected VHE gamma-ray sources in the survey. Most of the VHE gamma-ray sources are extended. Relativistic particles are surely involved in these sources due to the presence of VHE gamma-ray emission. A tenth of them are identified as SNRs. Although the survey was carried out to search for cosmic ray accelerators, a half of them are identified as PWNe. On the other hand, significant fraction of the sources have no clear counterpart in other wavelengths. These sources are called "dark" particle accelerators (Matsumoto et al., 2007; Fujinaga et al., 2011). Absence of X-ray emission may be interpreted that the source has already lost the higher energy electrons, which can emit synchrotron X-ray. VHE gamma-rays could be explained either hadronic or leptonic origin. Among the known kinds of sources, old PWNe or old SNRs may conform the observed properties of the dark particle accelerator. Study of dark particle accelerators and follow-up observations of VHE gamma-ray sources may also give some clues to understand the properties of the PWNe and their evolution.

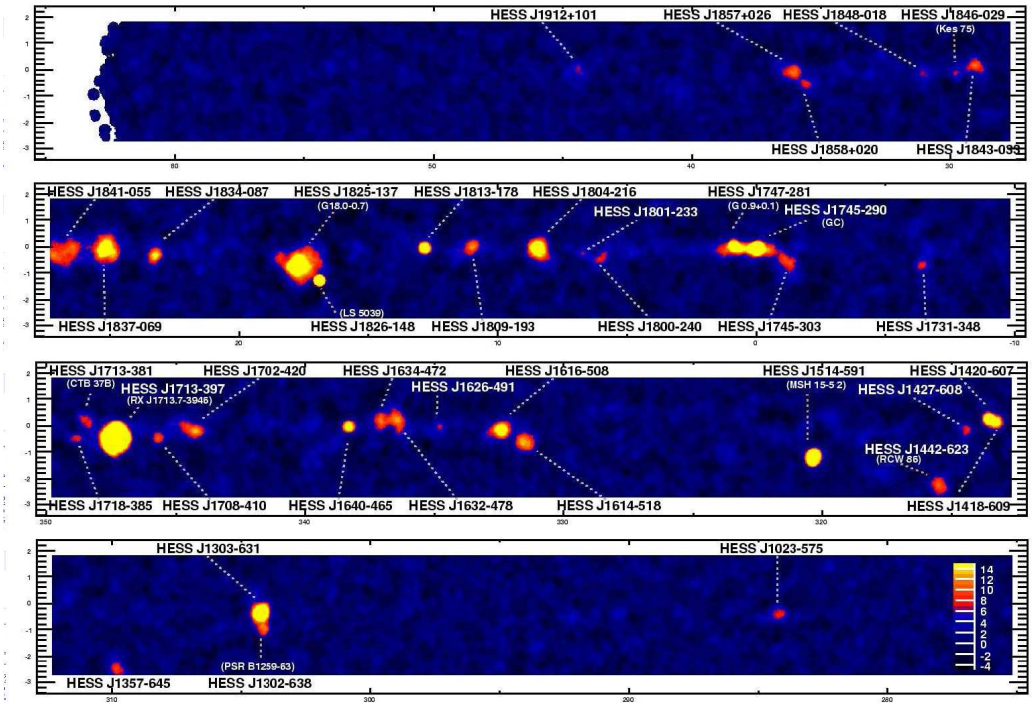

Figure 2.11: The H.E.S.S. survey image of the inner Galaxy in the VHE gamma-ray band. The gray scale indicates the statistical significance of extended sources. Adopted from Hinton (2007).

Chapter 3

Instruments

In this chapter, the X-ray observatories and the VHE gamma-ray telescopes used in this thesis are overviewd; namely, Suzaku, XMM-Newton, Chandra, H.E.S.S., and VERITAS. Suzaku (Mitsuda et al., 2007), XMM-Newton (Jansen et al., 2001), Chandra (Weisskopf et al., 2000a) are X-ray satellites, whereas High Energy Stereoscopic System (H.E.S.S.; Hofmann 2001) and Very Energetic Radiation Imaging Telescope Array System (VERITAS; Holder et al. 2008) are ground-based Cherenkov telescopes.

3.1 Suzaku

Suzaku is the 5th Japanese X-ray observatory. It was launched on July 10, 2005, and was successfully put into a near-circular orbit at an altitude of $\simeq$ 570 km and an inclination of 32 degrees. Three types of mission instruments are equipped, which are Suzaku is equipped with three types of mission instruments: X-ray Imaging Spectrometer (XIS: Koyama et al. 2007), Hard X-ray Detector (HXD: Takahashi et al. 2007; Kokubun et al. 2007) and X-ray micro-calorimeter (XRS). However, XRS is not operational due to sudden loss of the liquid helium just after the launch. XIS is installed at the foci of X-ray Telescopes (XRTs: Serlemitsos et al. 2007). Figure 3.1 shows a schematic side view of Suzaku on orbit. This figure is adopted from Suzaku Technical Description[1]. The characteristics of the instruments are listed in table 3.1.

3.1.1 XRT

A total of five light-weight thin-foil X-ray Telescopes (XRTs) are installed on Suzaku. It approximates the Walter-I optics with two conical reflectors made of thin aluminum foil. This makes it possible to produce a light-weighted telescope, yet having a large effective area. How-

[1] http://www.astro.isas.jaxa.jp/suzaku/doc/suzaku_td/

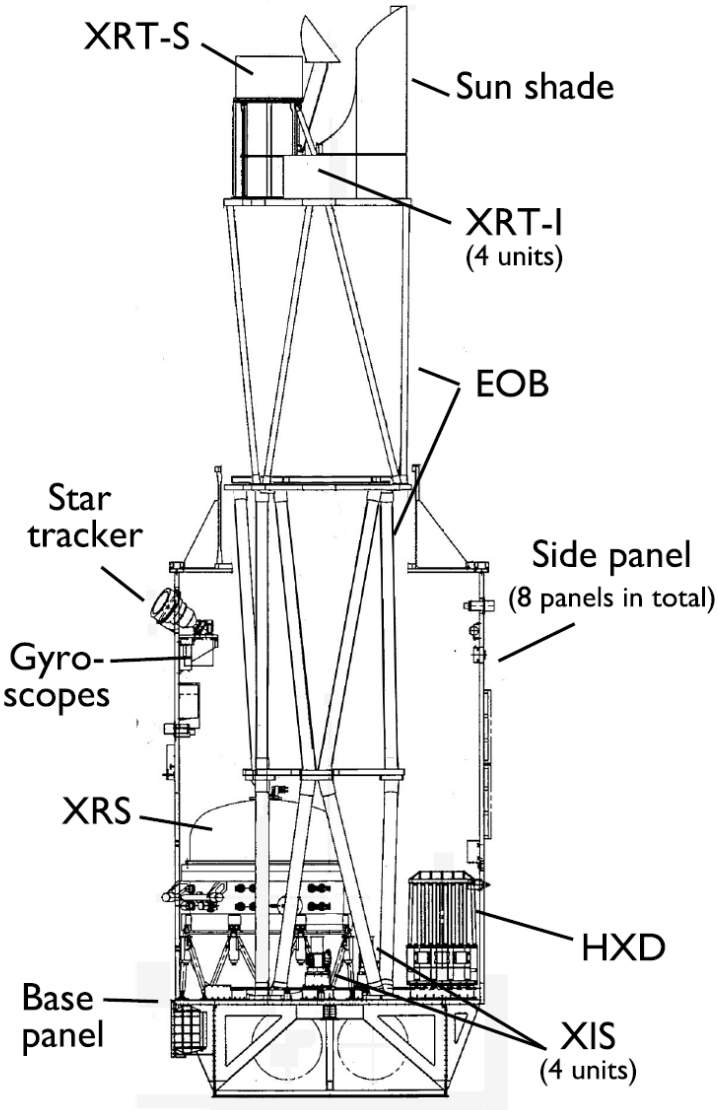

Figure 3.1: A schematic cross-section view of Suzaku with the optical bench extended showing the internal structures. The figure is adopted from Suzaku Technical Description[1]

ever, its angular resolution remains moderate compared to the currently working other X-ray telescopes. Suzaku XRTs are equipped with the pre-collimators to reduce the stray light. This is especially useful when observing a dim source near the bright one. Furthermore, the pre-collimator helps to reduce the contamination of the cosmic X-ray background. This is essential to observe dim and extended sources.

Among the five XRTs, four XRTs (XRT-I) are for XIS whereas the other XRT (XRT-S) for XRS. As explained above, XRS and XRT-S are not operational. The focal length of XRT-I is 4.75 m and the half power diameter (HPD) is $\simeq 2'.0$. Figure 3.2 shows the point spread function

Table 3.1: Characteristics of Suzaku

XRT	Focal Length	4.75 m
	Field of View	$20'$ at 1 keV
		$14'$ at 7 keV
	Geometrical Area/telescope	873 cm^2
	Weight/telescope	19.3 kg
	Effective Area/telescope	450 cm^2 at 1.5 keV
		250 cm^2 at 7.0 keV
	Angular Resolution	$2'.0$ (Half Power Diameter)
XIS	Field of View	$17'.8 \times 17'.8$
	Bandpass	0.2–12 keV
	Number of Pixels/CCD	1024×1024
	Pixel Size	24 μm $\times$ 24 μm
	Energy Resolution	$\simeq$ 2 % at 6 keV
	Effective Area	340 cm^2 (FI), 390 cm^2 (BI) at 1.5 keV
		150 cm^2 (FI), 100 cm^2 (BI) at 8 keV
	Time Resolution	8 s (Normal mode), 7.8 ms (P-Sum mode)
HXD	Field of View	$4^\circ.5 \times 4^\circ.5$ ($\geq$ 100 keV)
		$34' \times 34'$ ($\leq$ 100 keV)
	Bandpass	10–600 keV
		(PIN) 10–70 keV
		(GSO) 40–600 keV
	Energy Resolution	(PIN) $\simeq$ 4.0 keV (FWHM)
		(GSO) $7.6/\sqrt{E_{\rm MeV}}$ % (FWHM)
	Effective Area	$\simeq$ 160 cm^2 at 20 keV
		$\simeq$ 260 cm^2 at 100 keV
	Time Resolution	61 μs

and encircled energy function of XRT-I0. Although the angular resolution is moderate, its angular response has a sharp cusp, which helps to locate an X-ray source accurately. Figure 3.3 shows the total effective area of Suzaku (sum of four sets of XRT and XIS) in comparison with those of other working satellites. As seen in the figure, the effective area of Suzaku is much larger than that of Chandra and is comparable to XMM-Newton above 5 keV.

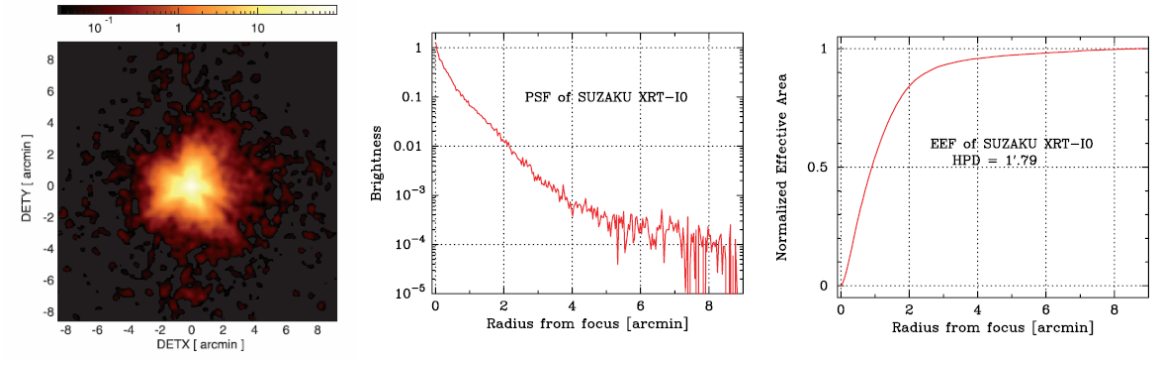

Figure 3.2: An example image of a point source (in left) with the point spread function (PSF, in middle) and the encircled energy function (EFF, in right) of XRT-I0 (Serlemitsos et al., 2007).

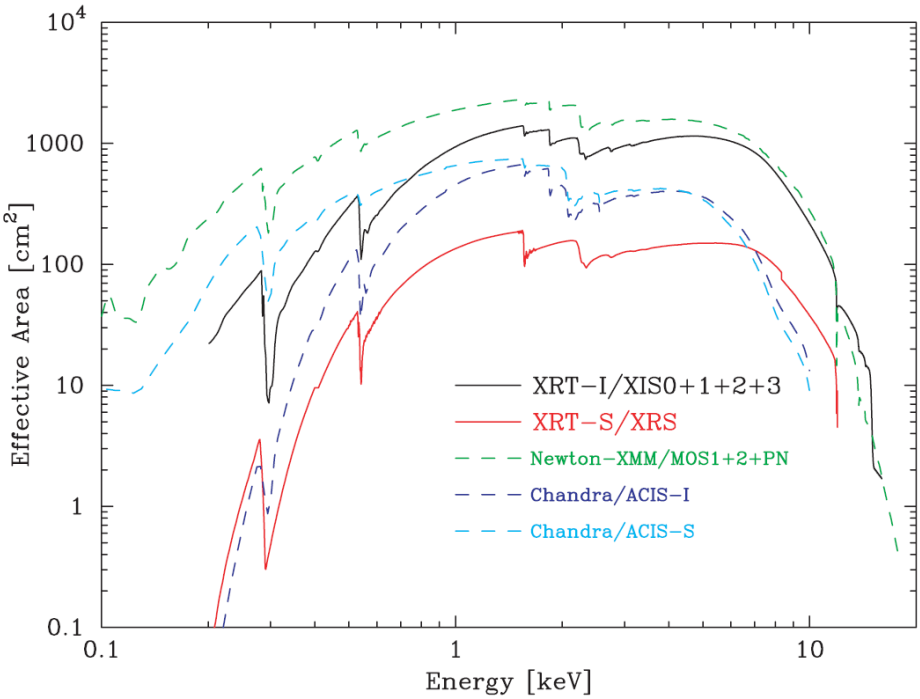

Figure 3.3: Total effective area of the four XRT-Is compared with that of XMM-Newton and Chandra (Serlemitsos et al., 2007).

3.1.2 XIS

Suzaku carries four sets of XIS located at the focal plane of XRT-I. An XIS employs an X-ray charge-coupled device (CCD), which is operated in a photon-counting mode. Figure 3.4 shows a picture of the camera body and a schematic view of the cross section. Each set of XIS is named XIS0, 1, 2 and 3. XIS1 uses a back-illuminated (BI) CCD, whereas other three

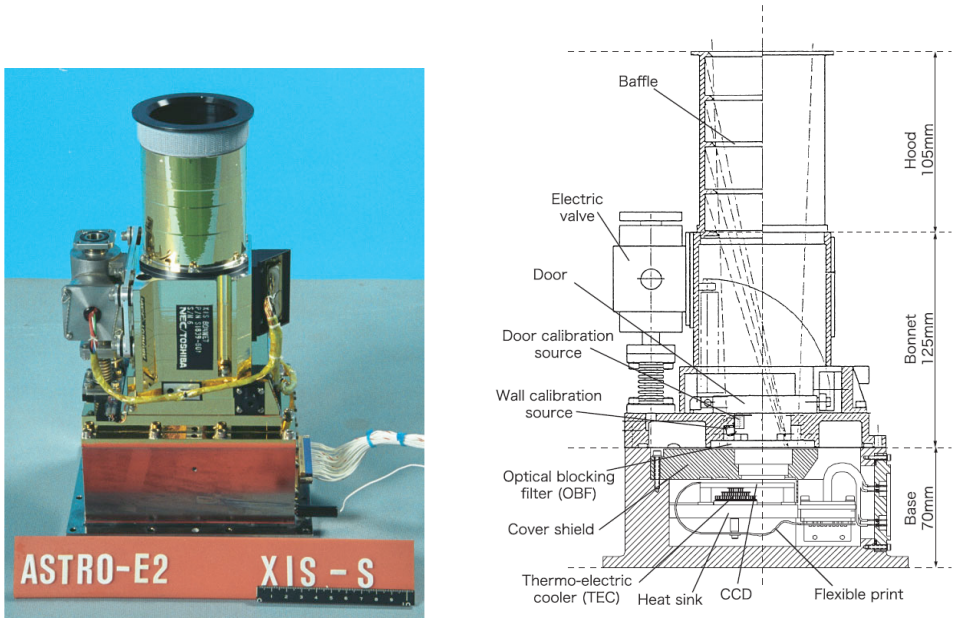

Figure 3.4: A picture of camera body and its cross section (Koyama et al., 2007).

front-side illuminated (FI) CCDs. Figure 3.5 shows the quantum efficiency (QE) curve of both the FI and BI CCDs. The BI CCD has superior QE below 1 keV because there is no gate structures at the incident surface. However, the QE at higher energies is limited because of the relatively thin depletion layer. Figure 3.6 shows the background count rate as a function of energy. The non X-ray background (NXB) of XIS, which is induced by charged particles and gamma-rays, is lower than other X-ray CCD cameras currently in operation. Each XIS sensor has ^{55}Fe calibration sources to illuminate the two corners of the CCD chip. Among the four XISs, XIS2 has not been operated since November 2006 due to its anomaly, which was probably caused by the micro-meteoroid hit. Also, a part of XIS0 has not been used since July 2009 due to the excess dark current, again probably caused by the micro-meteoroid hit.

XIS has large flexibility in operating the CCD. In normal clocking mode, which is used most often, the whole imaging area are read out regularly every 8 seconds. Thus, the exposure time and the time resolution of normal clocking mode is 8 sec. When observing a bright point sources, an 8 sec exposure may be too long and could cause significant photon pile-up. This situation is mitigated by using an window option, in which a smaller region than the full frame is read out frequently. Two types of window options are available, i.e. 1/4 window and 1/8 window options. When 1/4 window option is applied, a 1/4 area (256 $\times$ 1024 pixels) of the CCD is read out every 2 sec. The area is further redued to 128 $\times$ 1024 pixels in the 1/8 window option, and the exposure time becomes 1 sec. Thus, if a window option is applied, effective image size is reduced corresponding to the exposure time. The burst option enables us to reduce

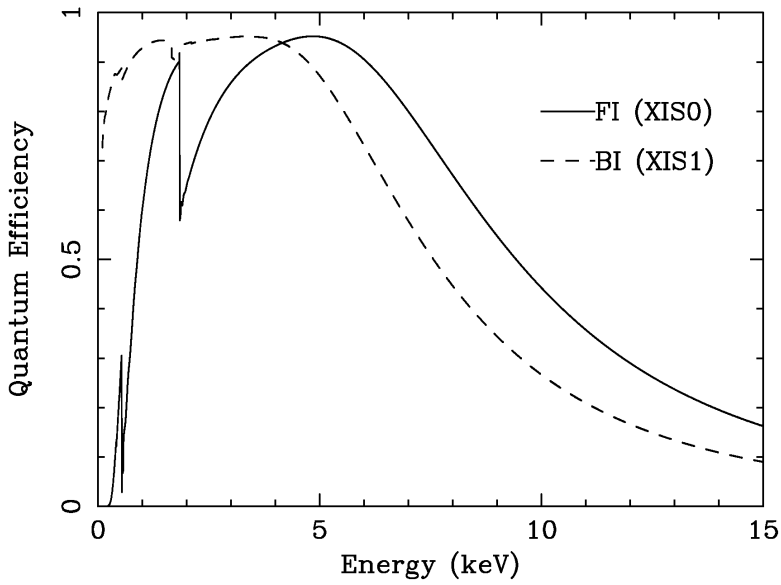

Figure 3.5: The QE curves of XIS as a function of incident X-ray energy (Koyama et al., 2007). The BI CCD has higher efficiency than FI CCD especially below 1 keV.

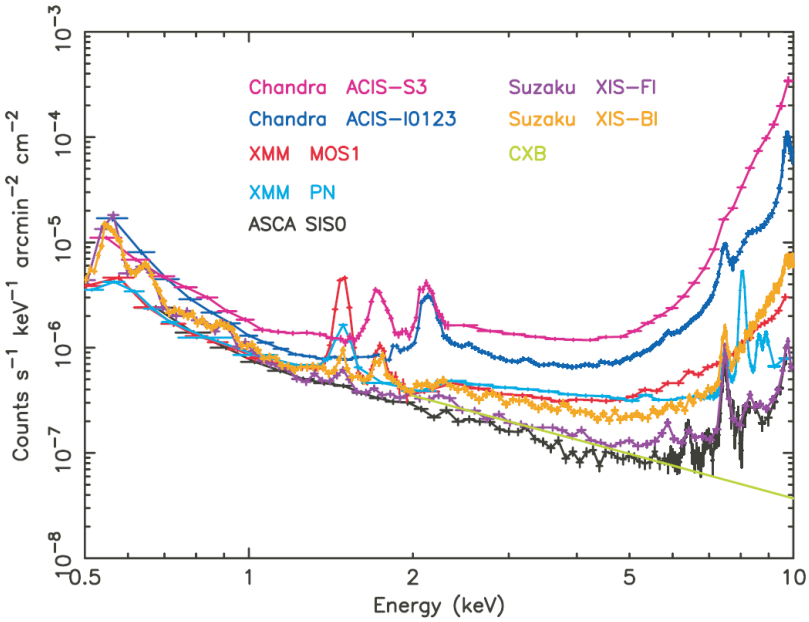

Figure 3.6: Comparison of the background spectra of XIS with those of other X-ray CCD cameras so far flown in space (Mitsuda et al., 2007). The background rate is normalized with the effective area and the field of view. Lower energy part is dominated by the CXB, thus almost same for all the CCD cameras, while the higher energy part is dominated by the NXB.

the exposure time keeping the original image size. Instead, a dummy exposure of, for example 7 sec is inserted to reduce the effective exposure to 1 sec. The burst option is used for bright, extended sources, and can be applied with a window option simultaneously.

Because an X-ray CCD is sensitive to the radiation damage, its performance gradually degrades in the space environment. In the case of XIS, the effect appeared most clearly in the decrease of the charge transfer efficiency. A charge packet produced by the photo-electric absorption of an X-ray photon cannot be transferred completely to the read out gate. Some electrons are lost in the charge traps during the transfer, which are defects in the lattice produced by the bombardment of the high energy particles. Because the electrons are lost stochastically, decrease of the charge transfer efficiency increases the uncertainty of the original number of electrons. This means that the energy resolution is degraded. In order to reduce the effect of the radiation damage, spaced-row charge injection (SCI: Prigozhin et al. 2008; Uchiyama et al. 2009a) has been adopted in the operation of XIS since September 2006. In this method, artificial charge is injected at the top of the imaging region every 54 rows during the frame-store transfer. The charge works to fill the traps produced by the radiation damage. XIS almost recovered the original performance just after the launch. Thus, SCI has been used basically for all observations after late 2006.

3.1.3 HXD

HXD is a compound-eye detector consisting of 16 main units (arranged as a 4×4 array) and the surrounding 20 crystal scintillators for active shielding. Each unit actually consists of two types of detectors, which are a GSO/BGO counter, and 2 mm-thick PIN silicon diodes located inside the well. Relatively soft X-rays are detected by the PIN diodes, which covers 10–70 keV. On the other hand, harder X-rays go through the diodes and are detected by the GSO, which locates just beneath the PIN diodes and covers 40–600 keV. Figure 3.7 shows a schematic view of HXD.

The field of view (FOV) of HXD is restricted by two types of collimators. One is the well-structure made by the BGO scintillator. This restricts the HXD FOV to $4^\circ.5$ in full-width at half maximum (FWHM). The other is the fine collimator installed inside the BGO well. It is made of thin phosphor bronze sheet to form 300 mm length, 3 mm width square collimator arranged in 8×8 array. The fine collimator restricts the FOV to $34'$ below 100 keV, whereas it becomes more or less transparent above 100 keV. Thus, the transmission of the HXD (as a function of the offset angle of the source) is energy dependent above 100 keV.

HXD is designed to achieve low detector background and hence very high sensitivity. This is realized by the active shield in three stages. The 1st stage is a well structure of the unit counter. The X-ray sensitive parts, PIN diode and GSO scintillator, are installed in the bottom

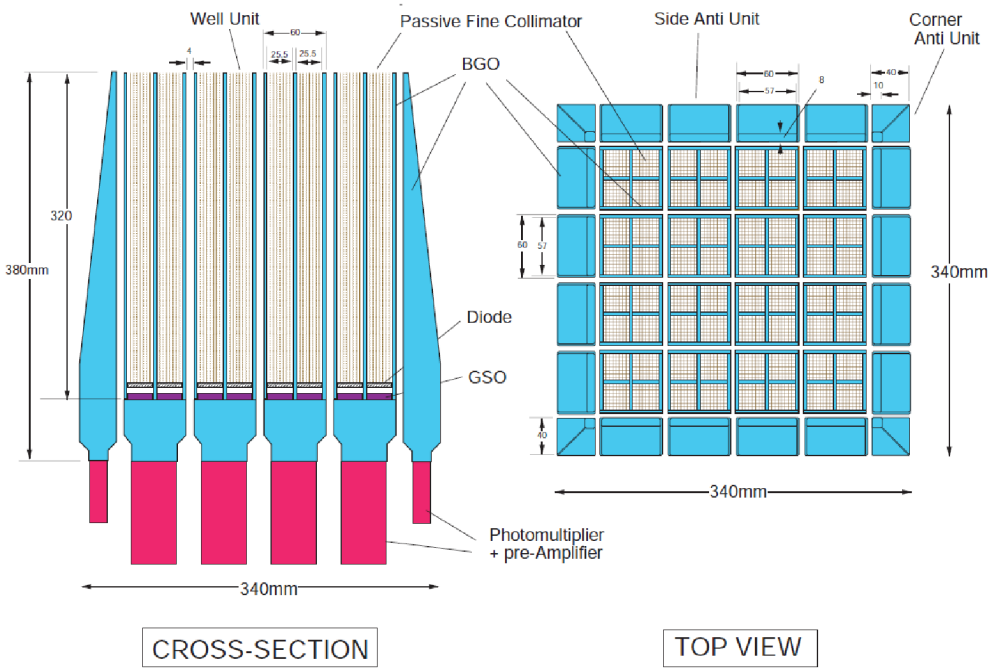

Figure 3.7: A schematic view of HXD (Takahashi et al., 2007).

of the deep well structure, which shield PIN and GSO from the background particles. The 2nd stage is the 4×4 configuration of the unit counters. Each unit can also work as an active shield of adjacent units. The last shield is the tightly arranged thick active shield surrounding the 4×4 counters. Figure 3.8 shows the detector background of HXD compared with other satellites.

Because HXD is a non-imaging detector, a background spectrum cannot be obtained simultaneously during the observation of the target. Thus, it is crucial to estimate and to subtract the background as accurate as possible to achieve the high sensitivity. Based on the satellite orbit, attitude, monitor date and so on, a model background is calculated and provided by HXD team for each observation. Details of the calculation method are described in Fukazawa et al. (2009).

3.2 XMM-Newton

XMM-Newton was developed by the European Space Agency (ESA) and was launched on December 10th, 1999. It carries three X-ray telescopes, which contain 58 high-precision concentric mirrors. Also, it carries three X-ray CCD cameras, named the European Photon Imaging Camera (EPIC). Two of them are metal oxide semiconductor (MOS) CCD arrays (referred to as the MOS cameras) (Turner et al., 2001). Two of the X-ray telescopes equipped with the MOS

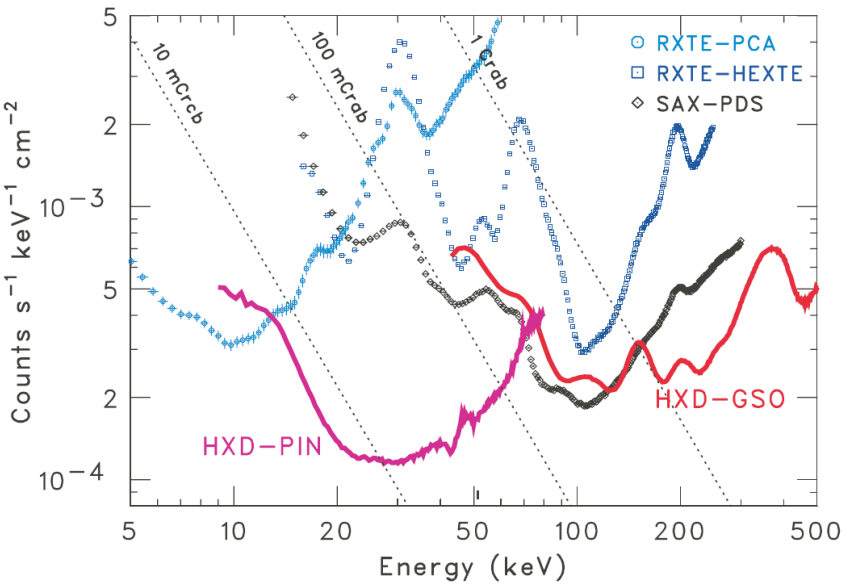

Figure 3.8: HXD background count rate as a function of energy (Mitsuda et al., 2007). The background rate is normalized with the effective area. Background spectra of RXTE and Beppo-SAX are also plotted for comparison.

camera are also equipped with the gratings, named Reflection Grating Spectrometers (RGS). The gratings divert about half of the telescope incident flux towards the RGS detectors such that about 44 % of the original incoming flux reaches the MOS cameras. The third X-ray telescope has an unobstructed beam; the EPIC instrument at the focus of the telescope uses pn CCDs and is referred to as the pn camera (Strüder et al., 2001).

Figure 3.9 shows a schematic view of one of the XMM-Newton telescopes on orbit. The characteristics of the instruments are listed in table 3.2. In this section, all of the figures are taken from the homepage of XMM-Newton technical description[2]. Below, only the X-ray telescope and EPIC are overviewed, whose data are analyzed in the thesis.

3.2.1 X-ray telescope

Each of the X-ray telescopes consists of 58 Wolter I grazing-incidence mirrors. The design of the optics was to achieve the highest possible effective area over a wide range of energies. Thus, the mirror system have to use a very shallow grazing angle of 30′ in order to provide sufficient reflectivity at high energies. The focal length is 7.5 m and the diameter of the largest mirror is 70 cm. Each telescope includes baffles for visible and X-ray stray-light suppression and an electron deflector for diverting soft electrons.

[2]http://xmm.esac.esa.int/external/xmm_user_support/documentation/technical/

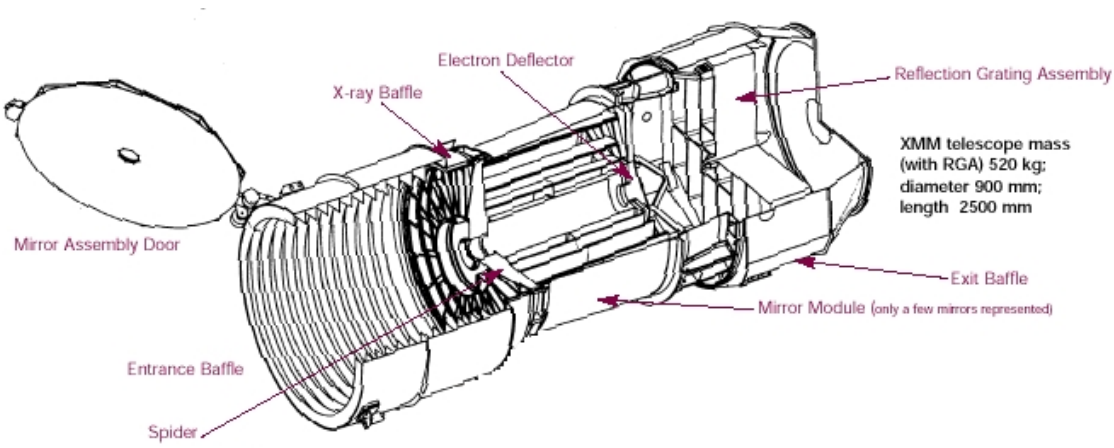

Figure 3.9: A schematic view describing one of the XMM-Newton telescopes on orbit. The figure is adopted from XMM-Newton technical description[2]

Table 3.2: Characteristics of XMM-Newton

Telescopes	Focal Length	7.5 m
	Field of View	30′ diameter
	Geometrical Area/telescope	1145 cm^2
	Weight/telescope	520 kg
	Effective Area/telescope	1500 cm^2 at 2 keV, 900 cm^2 at 7 keV,
		350 cm^2 at 10 keV
	Angular Resopution	15″ (Half Power Diameter)
EPIC	Field of View	30′ diameter
	Bandpass	0.15–12 keV (MOS), 0.15–15 keV (pn)
	Number of Pixels/CCD	600×600 (MOS), 200×64 (pn)
	Pixel Size	40 μm $\times$ 40 μm (MOS),
		150 μm $\times$ 150 μm (pn)
	Energy Resolution	$\simeq$ 2 % at 6.4 keV
	Effective Area	100 cm^2 (MOS), 500 cm^2 (pn) at 0.5 keV
		400 cm^2 (MOS), 1000 cm^2 (pn) at 1.5 keV
		100 cm^2 (MOS), 500 cm^2 (pn) at 8.0 keV
	Time Resolution	2.6 s (MOS; full frame), 73.4 ms (pn: full frame)

Figure 3.10: Pictures of CCDs installed to the MOS cameras (left) and the pn camera (right), adopted from the XMM-Newton technical description[2]

3.2.2 EPIC

EPIC is the main focal plane instrument onboard XMM-Newton, providing imaging and spectroscopic capabilities. As explained above, two of the cameras carries MOS CCDs and are named EPIC MOS. The other does pn CCD, and is named EPIC pn.

Each of the MOS camera carries 7 front-illuminated CCD chips. Figure 3.10 shows a picture of CCDs installed on the focal plane assembly. The CCDs are less sensitive than the pn CCDs in hard X-rays due to the relatively thin depletion layer ($\simeq 40$ μm).

The pn camera has a single silicon wafer with 12 back-illuminated CCD chips integrated. Figure 3.10 also shows the configuration of the pn CCDs. The CCDs are fully depleted (280 μm of the depletion depth) so that the detector efficiency in the high energy band becomes large. The parallel readout of 768 independent channels enables the camera to be operated very fast; only 80 ms are necessary to acquire one frame. Special readout modes allow the observation of transient objects with a time resolution of only 40 ms.

3.3 Chandra

Chandra X-ray Observatory (CXO or Chandra) was developed by the National Aeronautics and Space Administration (NASA), and was launched on July 23rd, 1999. The orbit of Chandra is highly elliptical and varies with time. As of December 2007 the apogee height was $\simeq 126,800$ km and the perigee height was $\simeq$ $22,000$ km. Chandra is equipped with the mirrors with four science instruments. The incoming X-rays are focused by the mirrors (HRMA: High Resolution Mirror Assembly) to a tiny spot on the focal plane. The focal plane instruments, ACIS (Advanced CCD Imaging Spectrometer; Garmire 1997) and HRC (High Resolution Camera), are well matched to capture the sharp images formed by the mirrors and to provide information

Table 3.3: Characteristics of Chanrda

HRMA	Focal Length	10 m
	Field of View	$30'$
	Geometrical Area/telescope	1145 cm^2
	Weight	1484 kg
	Effective Area	800 cm^2 at 0.25 keV, 400 cm^2 at 5 keV,
		100 cm^2 at 8 keV
	Angular Resoption	$0''.5$ (Half Power Diameter)
ACIS	Field of View	$16'.9 \times 16'.9$ (ACIS-I)
		$8'.3 \times 50'.6$ (ACIS-S)
	Bandpass	0.1–10 keV (pn)
	Number of Pixels/CCD	1024×1024
	Pixel Size	24 μm $\times$ 24 μm
	Energy Resolution	$\simeq$ 2 % at 6 keV
	Effective Area	110 cm^2 at 0.5 keV, 600 cm^2 at 1.5 keV
		40 cm^2 at 8.0 keV
	Time Resolution	3.2 s (full frame)
HRC	Field of View	$30' \times 30'$ (HRC-I), $6' \times 99'$ (HRC-S)
	Bandpass	0.08–10.0 keV
	Energy Resolution	$\simeq$ 1 keV at 1 keV
	Effective Area	133 cm^2 at 0.277 keV (HRC-I)
		227 cm^2 at 1 keV (HRC-I)
	Time Resolution	16 μs

about the incoming X-rays: their number, position, energy and time of arrival. Here I will overview HRMA, ACIS and HRC. Chandra is also equipped with other instruments, which are not related in this thesis. Table 3.3 lists the characteristics of the instruments. In this section, all of the figures are adopted from the Chandra Proposers' Observatory Guide[3].

3.3.1 HRMA

Chandra consists of four sets of concentric thin-walled, grazing-incidence Wolter Type-I mirrors called the High Resolution Mirror Assembly (HRMA). The front mirror of each pair is a paraboloid and the back a hyperboloid. The eight mirrors were fabricated from Zerodur

[3]http://cxc.harvard.edu/proposer/POG/html/index.html

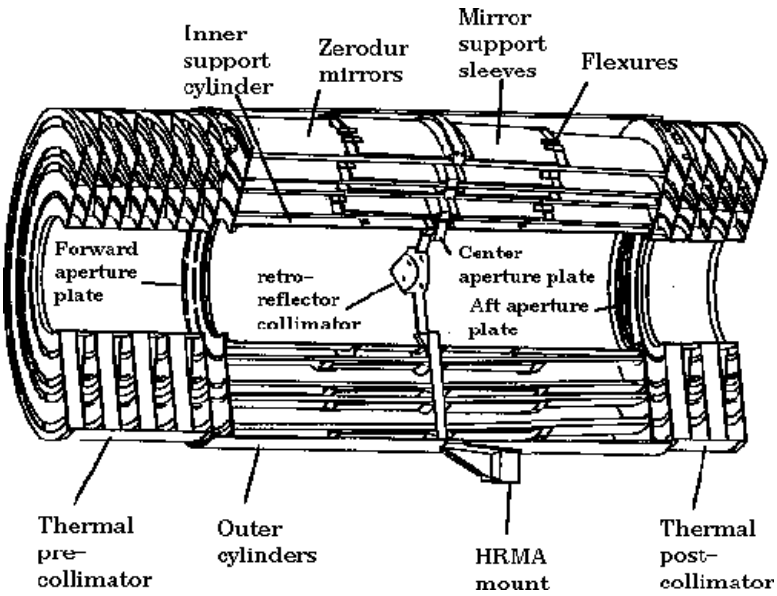

Figure 3.11: A schematic view of HRMA.

glass, polished, and coated with iridium on a binding layer of chromium. Figure 3.11 shows a schematic view of HRMA.

3.3.2 ACIS

ACIS is one of two focal plane instruments. It is comprised of two CCD arrays, a 4-chip array, ACIS-I; and a 6-chip array, ACIS-S. The CCDs are flat, however, the chips in each array are tilted to approximate the relevant focal surface. ACIS-I was designed for CCD imaging and spectroscopic capabilities, while ACIS-S can be used both for CCD imaging spectroscopy and high-resolution spectroscopy in conjunction with the HETG grating.

There are two types of CCD chips. ACIS-I is comprised of front-illuminated (FI) CCDs. On the other hand, ACIS-S is comprised of 4 FI and 2 back-illuminated (BI) CCDs, one of which is at the best focus position. The efficiency of ACIS has been discovered to be slowly changing with time, most likely as a result of molecular contamination build-up on the optical blocking filter. The BI CCDs response extends to lower energies than the FI CCDs and the energy resolution is mostly independent from position. The low-energy response of the BI CCDs is partially compromised by the contaminant build-up. The FI CCD response is more efficient at higher energies but the energy resolution varies with position due to radiation damage caused by protons reflecting through the telescope during radiation-zone passages in the early stage of the mission.

Figure 3.12 shows the layout of the CCD chips. The spacial resolution for on-axis imaging with ACIS is limited by the physical size of the CCD pixels (24 μm $\simeq 0''.492$) and not by the

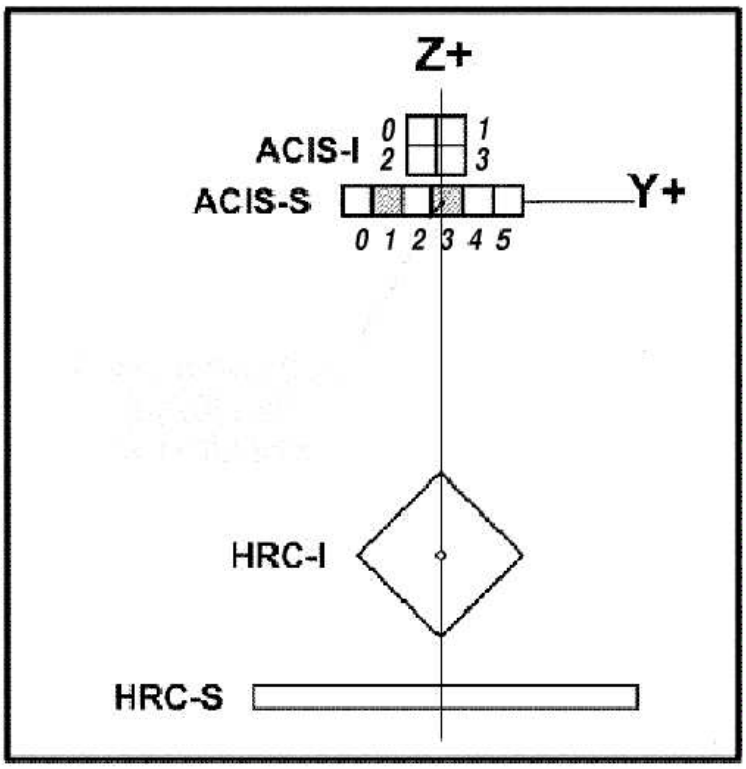

Figure 3.12: Arrangement of the ACIS and the HRC at the focal plane. The view is along the axis of the telescope from the direction of the mirrors. The shaded CCDs (S1 and S3) indicate BI CCD chips. The aim point can be placed at any point on the vertical solid line.

HRMA. This limitation applies regardless of whether the aim point is selected to be the nominal aim point on I3 or S3. Approximately 90 % of the encircled energy lands within 4 pixels ($\simeq 2''$) of the center pixel at 1.49 keV and within 5 pixels ($\simeq 2''.5$) at 6.4 keV. As the offset from the aim point becomes larger, the point spread function becomes larger.

The ACIS FI CCDs originally approached the theoretical limit of the energy resolution at almost all energies, while the BI CCDs exhibited a poor resolution.

3.3.3 HRC

HRC is also used at the focus of Chandra, where it detects X-rays reflected from an assembly of eight mirrors. The primary components of HRC are two Micro-Channel Plates (MCP). The unique capabilities of the HRC stem from the close match of its imaging capability to the focusing power of the mirrors. When used with the Chandra mirrors, HRC can make images that reveal detail as small as $0''.5$. The layout is shown in figure 3.12.

3.4 H.E.S.S.

H.E.S.S. is a system of four imaging atmospheric Cherenkov telescopes (IACTs), located in the Khomas Highlands of Namibia at a height of 1800 m above sea level. It covers an energy range from 100 GeV to several tens of TeV. It also has superior angular resolution of $\sim 0^{\circ}.1$, energy resolution about 16 % (Aharonian et al., 2006b), and total band sensitivity of a few times 10^{-13} erg s^{-1} cm^{-2}. H.E.S.S. is operated by the international collaboration of 32 scientific institutions over 12 different countries.

The 1st telescope of H.E.S.S. went into operation in 2002. All four are operational since 2003. Recently, a much larger 5th telescope, H.E.S.S. II, became operational since 2012, extending the energy coverage toward lower energies and further improving the sensitivity. The data I used for the thesis were all obtained with 4 telescope system of H.E.S.S. Thus, in what follows, I concentrate on H.E.S.S., and do not mention H.E.S.S. II.

Atmospheric Cherenkov technique exploits the cascade of secondary particles produced through interactions of primary gamma-rays with molecules in the Earth's upper atmosphere. These secondary particles emit Cherenkov light, and then they are observed by Cherenkov telescopes. The energy and direction of the primary gamma-rays can be reconstructed based on the intensity and shape of the detected Cherenkov light (e.g. Hillas 1996; Weekes 1996; Daum et al. 1997). The Cherenkov light is beamed toward the direction of the incident primary gamma-rays and illuminates the ground, an area of about 250 m in diameter, referred to as the Cherenkov light pool. They arrive within a very short time interval, a few nanoseconds. A telescope, located within the light pool, can detect the air shower. However, its mirror should be large enough to collect many photons (a primary photon of 1 TeV produces 100 photons/m^2 on the ground).

3.4.1 Telescope

H.E.S.S. uses four telescopes arranged in form of a square with 120 m side length, to provide multiple stereoscopic views of air showers. The diagonal of the square is oriented north-south. Figure 3.13 shows the H.E.S.S. array in Namibia. Also, figure 3.14 shows a schematic view of a telescope by Bernlöhr et al. (2003). Each telescope is segmented into 382 round mirror of 60 cm diameter, and then the total area of 12 m diameter. The mirror has a focal length of 15 m. Mirror reflectivity is above 80 %.

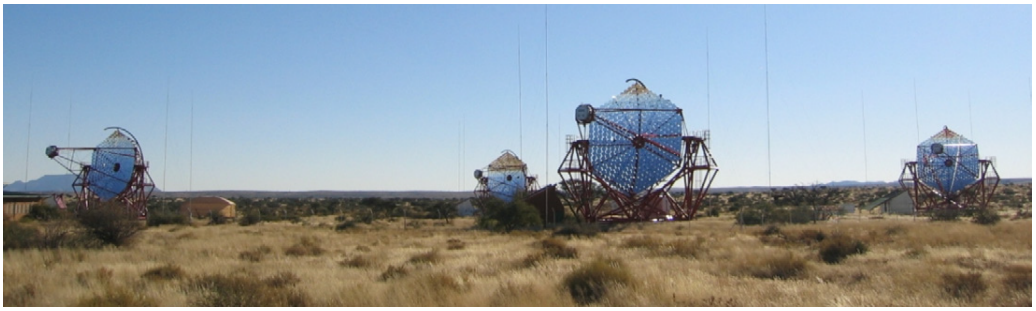

Figure 3.13: A picture of the H.E.S.S. array in Namibia (Aharonian et al., 2008c)

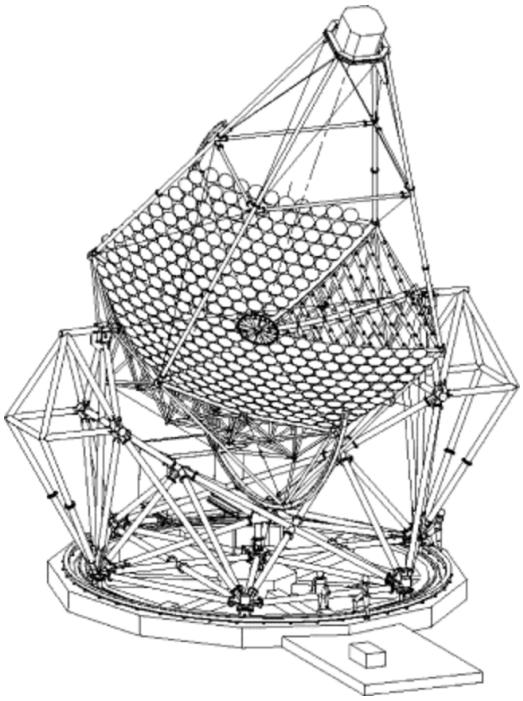

Figure 3.14: One of the four telescopes of H.E.S.S., showing the steel space frame of the dish and the telescope mount. Mirrors are removed in one section of the dish to show the support beams. This figure is adopted from Bernlöhr et al. (2003).

3.4.2 Camera

The focal plane detectors contain imaging cameras with 960 photo-multipliers (PMTs) of 0°.16 pixel size, for a 5° camera field of view (Punch, 2001). Figure 3.15 shows mechanics of the H.E.S.S. camera. The mechanics is designed for easy access to the electronics. The PMTs and their associated electronics are grouped into 60 Drawers which can be plugged-in interchangeably from the front of the camera after removal of the plate holding 960 Winston-cone light collectors. The position of this plate defines focal plane, and is accurate to 0.1 mm relative

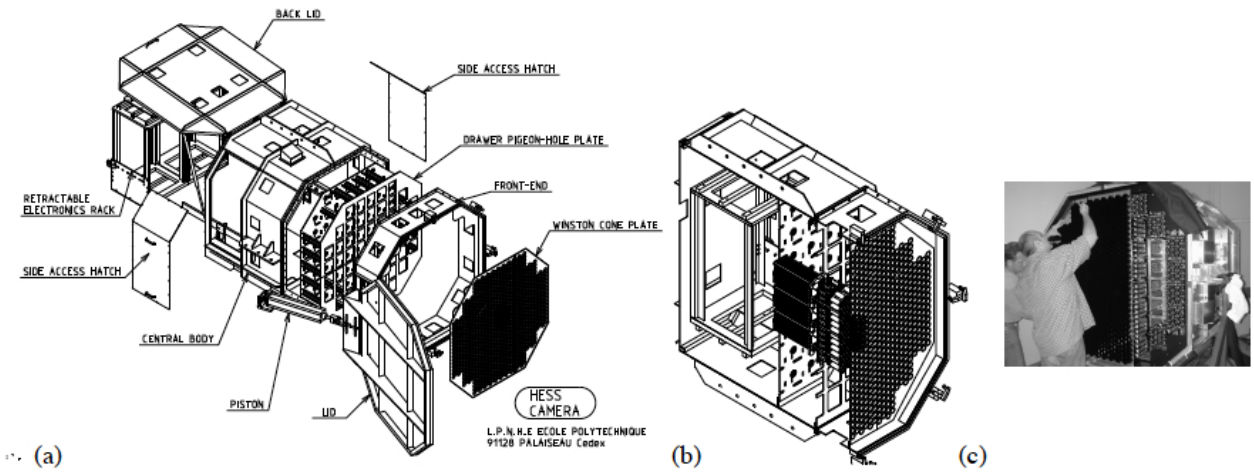

Figure 3.15: Mechanics of the H.E.S.S. camera (Punch, 2001): (a) exploded view, showing all elements, (b) cut-through view of closed camera with three drawers, (c) test mounting of drawers and cone plate.

Figure 3.16: The telescope array of VERITAS in Arizona, adopted from Holder et al. (2008).

to the PMT photo-cathodes. Each of the 60 Drawers contains 16 PMTs with their active bases. The size of the camera is about 1.5 m cube. The total weight of the camera, including mechanics, electronics, and low voltage supplies, is estimated to be 820 kg.

3.5 VERITAS

VERITAS is a ground-based IACTs operating at the Fred Lawrence Whipple Observatory (FLWO) in southern Arizona, USA (Holder et al., 2008). Figure 3.16 shows the VERITAS Array in Arizona. Construction of the array began with a prototype instrument in 2003; the first full telescope was commissioned in 2005, and the full array complemented in 2007.

VERITAS consists of four 12 m optical reflectors. Each telescope reflector consists of 350

individual mirrors, and is equipped with a 499-pixellated PMT camera, providing a $3^\circ.5$ field of view. Each PMT pixel in the telescope cameras is instrumented with a custom-built 500 Mega-samples per second Flash ADC. The energy coverage is from 100 GeV through 30 TeV. The angular resolution for a single event is $\simeq 0^\circ.1$ (68% containment radius). An unresolved source with a flux of 5% Crab source requires 2.5 hours. Spectral reconstruction is possible from a minimum energy of $\simeq$ 150 GeV and with an energy resolution of $\simeq$ 15% at high energies.

Chapter 4

X-ray Follow-up Observations of the unID VHE sources

As described in chapter 2, most of the VHE sources are identified as PWNe. However, a fifth of H.E.S.S. sources are unidentified and their nature is still unknown. To search for an X-ray counterpart and study their nature, deep observations of two unID sources, HESS J1702–420 and HESS J1427–608, were performed with Suzaku. In this chapter, the analysis results of these sources are explained. Description in this chapter for HESS J1702–420 is based on Fujinaga et al. (2011) and for HESS J1427–608 on Fujinaga et al. (2013).

4.1 HESS J1702–420

HESS J1702–420 is one of the brightest sources among the unID VHE gamma-ray sources (Aharonian et al., 2006a, 2008a). Its spatial extent is asymmetric ranging from 15′ through 30′. Its flux in the 1–10 TeV band is 3.1×10^{-11} erg s^{-1} cm^{-2} with a characteristic power-law spectrum with $\Gamma = 2.07 \pm 0.08$. Figure 4.1 shows the 843 MHz radio image of the HESS J1702–420 field, with the H.E.S.S. image and nearby sources. An SNR G344.7–0.1 and a pulsar PSR J1702–4128 are located in the outskirts of this source. Aharonian et al. (2008a) concluded that G344.7–0.1 is not associated to HESS J1702–420 because the angular size of the SNR is too small and the estimated distance of SNR (14 kpc, Dubner et al. 1993) is very large. On the other hand, PSR J1702–4128 may be related to HESS J1702–420 (Gallant, 2007). Also, a hint of extended X-ray emission characteristic of PWNe was obtained by Chandra (Chang et al., 2008). However, given the large angular offset of 35′ between the pulsar and the peak of the VHE gamma-ray source, which corresponds to $\simeq$ 50 pc for the distance of 5.1 kpc to the pulsar (Guseinov et al., 2004) , and the 3 orders of magnitude difference between the X-ray PWN energy flux (2×10^{-14} erg s^{-1} cm^{-2} in the 0.3–10 keV band) and the VHE gamma-ray

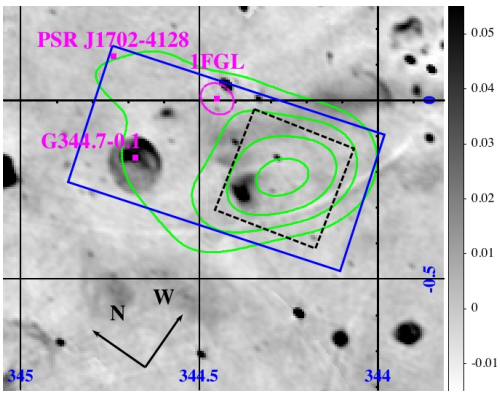

Figure 4.1: The 843 MHz Molongo radio image of the HESS J1702–420 field (Green et al., 1999) is shown in gray scale in units of Jy beam^{-1}, in Galactic coordinates. The green contours show the H.E.S.S. intensity map (Aharonian et al., 2006a) in linear scale. The 1σ error region of the Fermi source, 1FGL J1702.4–4147c, is indicated by a magenta circle with the label "1FGL" (Abdo et al., 2010). The black dashed box represents the FOV of Suzaku XIS. The emission region of VHE gamma-rays is approximated by the blue solid rectangle of $0^\circ.8 \times 0^\circ.4$, when we constrain the total X-ray emission from the source. This figure is presented by Fujinaga et al. (2011).

flux, we consider the association of this source rather weak.

A deep observation of the sky field including HESS J1702–420 has not been carried out so far, and only survey results are available. No plausible counterpart is found in the Galactic SNR catalog (Green, 2009). 1FGL J1702.4–4147c, located 14 arcmin away from HESS J1702–420, is listed on the Fermi first source catalog (Abdo et al., 2010). They reported that the diffuse background model needs to be improved on the Galactic plane and the position of the GeV source depends on this model. Thus, it is unclear that 1FGL J1702.4–4147c is a counterpart of HESS J1702–420. In order to search for an X-ray counterpart, a deep X-ray observation of HESS J1702–420 with Suzaku was performed.

4.1.1 Analysis

It was clear from the quick-look analysis of XIS that no bright source was present in the FOV. Therefore, accurate background subtraction is crucial to identify a possible counterpart. For this purpose, two sets of archive data were selected, which are useful to estimate the background of this observation. Considering the postion dependence of the Galactic ridge X-ray emission (GRXE: cf., Koyama et al. 1989; Yuasa et al. 2008; Yamauchi et al. 2009), the data were selected to satisfy the following criteria: (1) $300^\circ \leq l \leq 350^\circ$, $-0^\circ.25 \leq b \leq -0^\circ.15$, (2) free from bright sources, and (3) observed with normal clocking mode. Hereafter, we refer to these two sets of

Table 4.1: Journal of the source and background observations

	Obs ID	Observation date	Aim point[1] (l, b)	Exposure (ks)	SCI
HESS J1702–420	502049010	2008/03/25–2008/03/30	$(344°.26, -0°.220)$	216	On
Background 1	100028010	2005/09/19–2005/09/20	$(332°.40, -0°.150)$	45	Off
Background 2	100028020	2005/09/18–2005/09/19	$(332°.00, -0°.150)$	21	Off

[1] In Galactic coordinates.

data as background 1 and background 2, respectively. For this analysis, version 2.2.7.18 of the processed data for HESS J1702–420 and version 2.0.6.13 for the background data, provided by Suzaku team, were used. The differences between these versions on XIS are the calibration data for SCI and that for burst options, which are negligible for the analyses in this paper. The data were analyzed with the HEADAS software version 6.7 and XSPEC version 12.5.1. The journal of the observations are listed in table 4.1.

Images

A vignetting corrected image of XIS was calculated. For this purpose, images of the non X-ray background (NXB) were generated using the FTOOL `xisnxbgen` (Tawa et al., 2008). After subtracting the NXB image, vignetting was corrected using the vignetting map created by the FTOOL `xissim` (Ishisaki et al., 2007). Finally, all the images of XIS0, XIS1 and XIS3 were summed up. Figure 4.2 shows the resulting image of both the soft and hard energy bands.

No clear point source is seen in the soft energy band, whereas two significant sources are found in the hard energy band. Hereafter, the two sources are referred to as src A and src B. They are consistent with point sources if we consider the fluctuation of the pointing direction of Suzaku, which is at most $\simeq 1'$ (Serlemitsos et al., 2007; Uchiyama et al., 2008), and a typical half power diameter of the point spread function ($\simeq 2'$, Serlemitsos et al. 2007).

Energy Spectra of Point Sources

The fluxes of the faint point-like sources were calculated. Since the poor statistics prevented us from detailed spectral analysis of the two point sources, the count rates of each sources were converted into the X-ray fluxes using `WebPIMMS`[1]. The count rate of the background was calculated using the area shown in figure 4.2. Because the mirror vignetting (0.8 for src A and

[1] http://heasarc.gsfc.nasa.gov/Tools/w3pimms.html

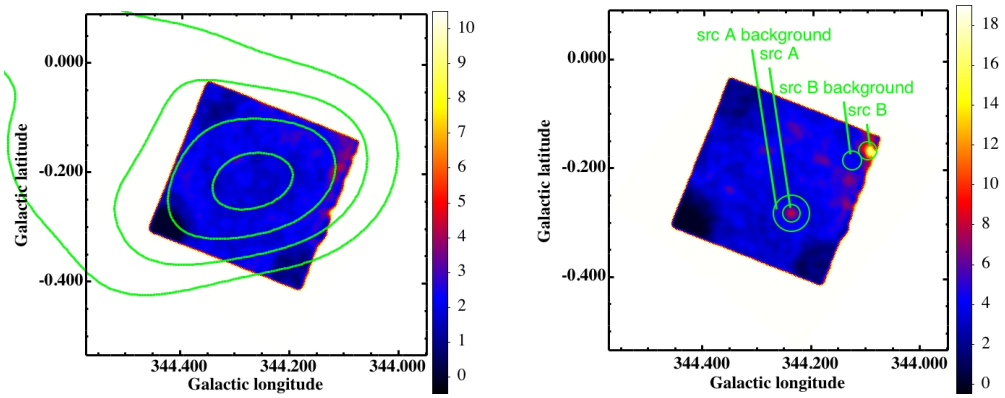

Figure 4.2: Suzaku XIS images of HESS J1702–420 field in the 0.5–2 keV band (left) and the 2–8 keV band (right). Definition of the color scale is indicated in the right-hand-side of each panel in unit of counts/pixel. These images were binned to a pixel size of 8″, and were smoothed with a Gaussian of $\sigma = 1'.0$. The vignetting is corrected after the NXB subtraction. In the left image, the VHE gamma-ray intensity map is overlaid in the green contour (the same as figure 4.1). The regions described in the hard band image are used for the spectral analysis of point sources. Adopted from Fujinaga et al. (2011).

0.7 for src B) is not considered in `WebPIMMS`, it was corrected separately. The spectral shape was assumed that these sources have the same intrinsic spectrum of a power-law with a photon index of 2.1 (same as HESS J1702–420) modified by the interstellar or circumstellar absorption of $N_{\rm H} = 1.5 \times 10^{22}$ cm^{-2} (Kalberla et al., 2005). The X-ray fluxes in the 2–10 keV band were $(3.0 \pm 0.6) \times 10^{-14}$ erg s^{-1} cm^{-2} (src A) and $(1.9 \pm 0.7) \times 10^{-14}$ erg s^{-1} cm^{-2} (src B), where the errors are in 90% confidence limit.

Diffuse Emission

An excess diffuse emission, which may be associated to HESS J1702–420, is looked for. The diffuse emission is simply assumed to be distributed uniformly in the XIS FOV. For this purpose, the energy spectrum (including background) of the entire XIS FOV was calculated, and is compared with that of the background observations. Below 4 keV, background 1 was contaminated by an SNR, RCW 103. Thus the spectra were used only in the 4–8 keV band. It is noteworthy that the observation of HESS J1702–420 was carried out with SCI-on, whereas the background observations with SCI-off. Because dead areas are introduced in the XIS image with SCI-on, they need to be incorporated in the analysis using appropriate response files. Two kinds of response files, i.e. redistribution matrix files (RMFs) and ancillary response files (ARFs), were made for each spectrum using the FTOOL `xisrmfgen` and `xissimarfgen` (Ishisaki et al., 2007), respectively. The dead area is included in the ARFs.

The background data of XIS consist of 3 components, i.e. NXB, cosmic X-ray background (CXB), and GRXE. NXBs were generated using `xisnxbgen` as explained above. Based on Tawa et al. (2008), we estimate the systematic error of NXB is 5.9 % in 4–8 keV (at 90 % confidence limit). The NXB subtracted energy spectra for background 1 and 2 were summed up (background 1+2) to use the later analysis. The GRXE is constant in time, but depends on the Galactic coordinate, mostly on latitude. HESS J1702–420 is separated from background 1+2 by 12 degree along to the Galactic longitude, while their Galactic latitudes are almost same (see table 4.1). According to Revnivtsev et al. (2006), angular separation of 12 deg along the Galactic longitude in the vicinity of HESS J1702–420 may cause systematic change of GRXE by $\simeq$ 20 %. In addition to this, GRXE has small scale fluctuation. Thus, a careful analysis may be needed. In what follows, we compare the GRXE between HESS J1702–420 and background 1+2. Then, we proceed to the search for the excess emission from HESS J1702–420.

At first, the NXB subtracted spectra of HESS J1702–420 with those of background 1+2 were compared. Here, a simple model spectrum is adopted, which consist of a power-law with three gaussians. The model is appropriate to represent a sum of the CXB and GRXE. The spectra of HESS J1702–420 and background were fitted separately. Figure 4.3 shows the results and the best-fit parameters are summarized in table 4.2. The flux of the power-law is not consistent with each other, which may be due to the systematics of the background subtraction and/or the presence of excess emission. The three gaussians are considered to be associated to the GRXE and their fluxes are a good measure of the GRXE flux (Yamauchi et al., 2009). As explained in the previous paragraph, the GRXE flux around HESS J1702–420 may be larger than that around background 1+2 by 20 % due to its global variation. However, the gaussian fluxes do not follow this trend. In fact, they are consistent with each other within the statistical errors. This is due to the small scale fluctuation of the GRXE and the intrinsic difference of the GRXE fluxes may be smaller than 20 %. In the present analysis, the systematic error of GRXE is assumed to be at most 20 %.

Next, the excess emission is derived from the simultaneous fitting of HESS J1702–420 and background 1+2 spectra. The model parameters of the background spectra were linked between the HESS J1702–420 and the background 1+2 data. Furthermore, a possible emission from HESS J1702–420 is modeled as a power-law with $\Gamma = 2.1$, same as that obtained by Aharonian et al. (2008a), and included it in the model function for the HESS J1702–420 data. The fit was reasonably good with χ^2/d.o.f. = 465.6/359. However, it becomes insignificant if we consider the systematic error of the NXB and GRXE (5.9 % and 20 %, respectively, and $\simeq$7.1 % in total at 90 % confidence range). The intrinsic X-ray flux in the 2–10 keV band is 3.4 $^{+2.9}_{-2.7}$(statistical) $^{+2.0}_{-2.1}$(systematic) (10^{-13} erg s^{-1} cm^{-2}) with the 90 % confidence range. Taking account both the statistical and systematic errors, there is no significant excess emission

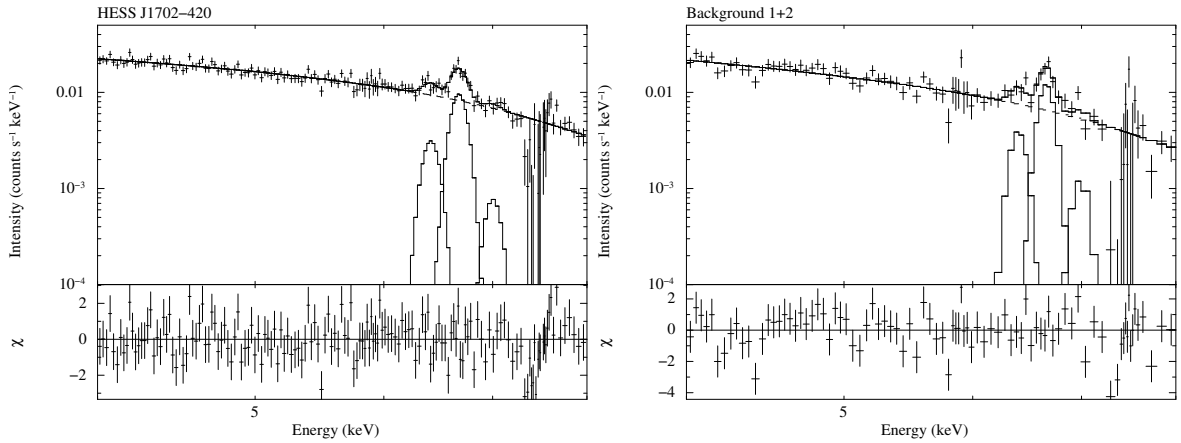

Figure 4.3: XIS FI spectra of HESS J1702–420 (left) and background 1+2 (right) in the 4–8 keV band. The dashed line and solid lines show the power-law component and the iron line features. Adopted from Fujinaga et al. (2011).

Table 4.2: The best-fit parameters of the HESS J1702–420 and the background spectra

		HESS J1702–420	Background 1+2
Power-law	Γ	1.6 ± 0.1	2.1 ± 0.1
	Flux[1]	2.7 ± 0.1	2.3 ± 0.1
Neutral-Fe	Energy (keV)	6.40 ± 0.03	$6.46^{+0.03}_{-0.04}$
	Intensity[2]	3.9 ± 1.3	$6.1^{+1.6}_{-1.7}$
Fe_{XXV}	Energy (keV)	6.68 ± 0.01	6.68 ± 0.01
	Intensity[2]	12.7 ± 1.5	$13.5^{+1.9}_{-1.8}$
Fe_{XXVI}	Energy (keV)	6.97 (fixed)	6.97 (fixed)
	Intensity[2]	$1.0^{+2.0}_{-1.0}$	4.0 ± 1.6
χ^2/d.o.f.		193.37/163	185.15/124

Notes. Errors are in 90% confidence region.

[1] In units of 10^{-12} erg s^{-1} cm^{-2} for 4–8 keV.

[2] In units of 10^{-6} photons s^{-1} cm^{-2}.

in the entire XIS FOV (7.4×10^{-2} deg^2) and the upper limit is 6.9×10^{-13} erg s^{-1} cm^{-2} with 90 % confidence limit.

4.1.2 Discussion

Comparison of X-ray and VHE Gamma-ray Fluxes

To consider the nature of the sources and the meaning of the upper limit, a flux ratio ($F_{\rm TeV}/F_{\rm X}$) was evaluated, where $F_{\rm TeV}$ is the flux in the 1–10 TeV band and $F_{\rm X}$ in the 2–10 keV band, respectively. If we assume that the VHE gamma-rays are produced via inverse Compton scattering of the cosmic microwave background (CMB) by electrons, and X-rays via synchrotron emission, the flux ratio corresponds to the ratio of the energy densities of CMB and the magnetic field. If the VHE gamma-rays are mostly produced by electrons, the ratio becomes smaller than ~ 1. On the other hand, if electrons are not involved, the ratio becomes larger than ~ 1. Typically, VHE gamma-ray associated PWN and SNR typically have a flux ratio less than 10^1 ($F_{\rm TeV}/F_{\rm X} < 10$).

The two faint point sources detected in the XIS FOV are most likely not related to the VHE source. Their flux ratio, $F_{\rm TeV}/F_{\rm X} \sim 10^3$, is too large to consider either of them as a X-ray counterpart of HESS J1702–420. Furthermore, their X-ray fluxes are less than the upper limit of the diffuse X-ray flux. The diffuse emission fainter than the upper limit would be more plausible as the X-ray counterpart than two faint sources. As shown in figure 4.1, the VHE gamma-ray source is more extended than the XIS FOV. A possible X-ray counterpart may also be more extended than the XIS FOV. Thus we need to consider the source extension (outside the XIS FOV) to obtain the correct upper limit of the X-ray flux. The rough size of the HESS source is approximated to be a $0^\circ.8 \times 0^\circ.4$ rectangular (the blue box in figure 4.1) and the X-ray surface brightness is constant over the entire rectangular region. Then, the upper limit for this source is estimated to be 2.7×10^{-12} erg s^{-1} cm^{-2} in the 2–10 keV band.

If we use this upper limit, the flux ratio of this source becomes large ($F_{\rm TeV}/F_{\rm X} > 12$). The (lower limit of the) ratio is comparable to those known as dark particle accelerators (e.g., HESS J1616–508 with $F_{\rm TeV}/F_{\rm X} > 55$ (Matsumoto et al., 2007); HESS J1804–216 with $F_{\rm TeV}/F_{\rm X} > 13$ (Bamba et al., 2007)). Thus, HESS J1702–420 is found to be a dark particle accelerator.

Wide-band Spectrum

Figure 4.4 shows the wide-band spectral energy distribution of HESS J1702–420. The X-ray spectrum can be estimated from the VHE gamma-ray spectrum assuming a simple one-zone model and electron origin. In the most simple approach, the seed photon field is assumed to be only CMB, the Thomson cross section is taken for Compton scattering, and no cut-off in the electron spectrum is assumed (see Balbo et al. (2010) for details of the model). The flux ratio corresponds to the ratio of the energy density of the seed photon and the local magnetic field.

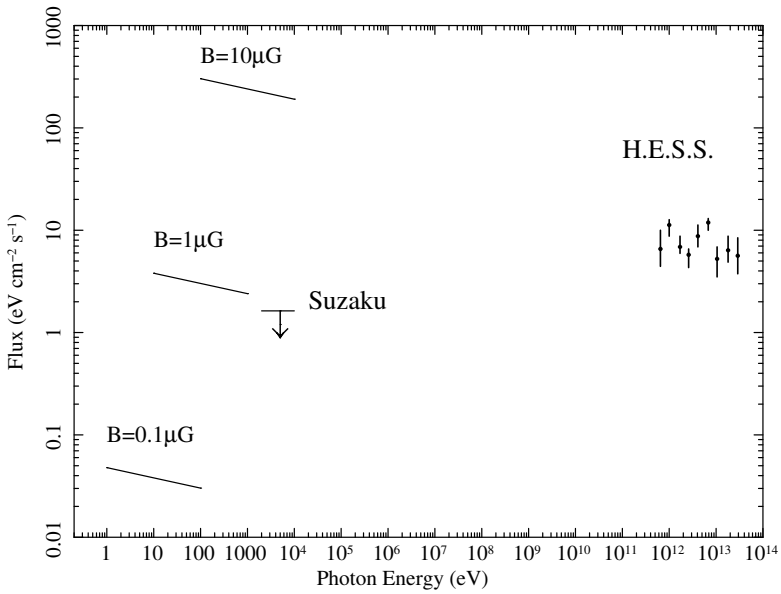

Figure 4.4: Spectral energy distribution of HESS J1702–420 from the X-ray to VHE gamma-ray bands. The synchrotron X-ray emission expected for the simple one-zone model (using only CMB as target photon field for inverse Compton scattering) is indicated as a function of the magnetic field. Adopted from Fujinaga et al. (2011).

If we assume the photon index of the X-ray spectrum is same as that of the VHE gamma-ray spectrum ($\Gamma = 2.1$), the X-ray flux is represented by a function of the local magnetic field. The estimated spectra for $B = 0.1\ \mu\mathrm{G}, 1\ \mu\mathrm{G}, 10\ \mu\mathrm{G}$ are overlaid on Figure 4.4. According to the derived flux ratio, the local magnetic field would be $B < 0.9\ \mu\mathrm{G}$, which is smaller than the typical value of $B \simeq 3 - 10\ \mu\mathrm{G}$ on the Galactic plane. To resolve this discrepancy, several possibilities are conceivable: (1) a simple one-zone model does not hold for HESS J1702–420, (2) the electron spectrum has a cut-off, and (3) the VHE emission is originated not from electrons but from protons.

Because we could not find an X-ray counterpart of HESS J1702–420, the nature of this source remains unknown. However, the number of similar sources (i.e. dark particle accelerator) is increasing. Thus, it might be a rather common source type in our Galaxy. Yamazaki et al. (2006) suggest that an old SNR ($t \simeq 3 \times 10^5$ yr) tends to have high flux ratio sometimes reaching $F_{\mathrm{TeV}}/F_{\mathrm{X}} \sim 10^2$. Such an old SNR may be consistent with our results, because it preferentially emit soft X-rays which are easily absorbed by the interstellar matter on the Galactic plane. In this case, no significant X-ray emission may be observed. Thus an old SNR scenario may be one of the plausible possibilities consistent with the current X-ray and gamma-ray observations. A similar possibility is reported for HESS J1745–303 by Bamba et al. (2009).

4.2 HESS J1427–608

HESS J1427–608 is one of the unID VHE gamma-ray sources located at $l = 314°.409, b = -0°.145$ (Aharonian et al., 2008a), and is extended with $\sigma = 0°.06$ [2]. The flux is $F_{\rm TeV} = 4.0 \times 10^{-12}$ erg s^{-1} cm^{-2} in the 1–10 TeV band with a photon index of $\Gamma = 2.16$ (Aharonian et al., 2008a). No plausible counterpart is listed in the Galactic supernova remnant (SNR) catalog (Green, 2009) or in the SIMBAD data base[3] in the vicinity of HESS J1427–608. In addision, no energetic pulsar was found within $100'$ from HESS J1427–608. To search for an X-ray counterpart, the observation of HESS J1427–608 was held with Suzaku. Also the XMM-Newton archive data of HESS J1427–608 was analyzed.

4.2.1 Analysis of Suzaku

The sky region including HESS J1427–608 was observed with Suzaku (Mitsuda et al., 2007) from 2010 January 13 through 16. Among the four XIS sensors, XIS2 is not operational[4] and a part of XIS0 (corresponding to the off-source region in the latter analysis) is not usable due to its anomaly[5]. Hereafter, unless otherwise mentioned, we used only XIS1 and XIS3 data for the current analysis. XIS was operated in normal clocking mode without any window options. Spaced-row charge injection (Prigozhin et al., 2008; Uchiyama et al., 2009a) was used to reduce the effects of radiation damage.

For the analyses, the version 2.4.12.27 of the processed data for HESS J1427–608 was used. The data were analyzed with the HEADAS software version 6.10 and XSPEC version 12.6.0. We used the cleaned event file created by the Suzaku team. The journal of the observation is listed in table 4.3.

Images

Figure 4.5 shows XIS images in the soft (0.5–2 keV) and the hard (2–8 keV) bands. The images were corrected for exposure using an exposure map generated by the FTOOL `xisexpmapgen` after subtracting non X-ray background (NXB) images generated by the FTOOL `xisnxbgen` (Tawa et al., 2008). Finally, the XIS1 and XIS3 images were added, and the resulting image was binned to a pixel size of 8" and smoothed with a Gaussian of $\sigma = 1'.0$. The position

[2] Poster presentation by Komin, N., et al. in "The X-ray Universe 2011" held in June 27–30, 2011, at Berlin, Germany, http://xmm.esac.esa.int/external/xmm_science/workshops/2011symposium/posters/Komin_TopicE.pdf

[3] http://simbad.u-strasbg.fr/simbad/

[4] JX-ISAS-SUZAKU-MEMO-2007-08; http://www.astro.isas.jaxa.jp/suzaku/doc/suzakumemo/suzakumemo-2007-08.pdf

[5] JX-ISAS-SUZAKU-MEMO-2010-01; http://www.astro.isas.jaxa.jp/suzaku/doc/suzakumemo/suzakumemo-2010-01.pdf

Table 4.3: Journal of the X-ray observations pointing at HESS J1427–608

	Obs ID	Observation date	Effective Exposure (ks)
Suzaku	504034010	2010/01/13–2010/01/16	104
XMM-Newton	0504990101	2007/08/09	21/22/15†

† The effective exposures for MOS1/MOS2/pn.

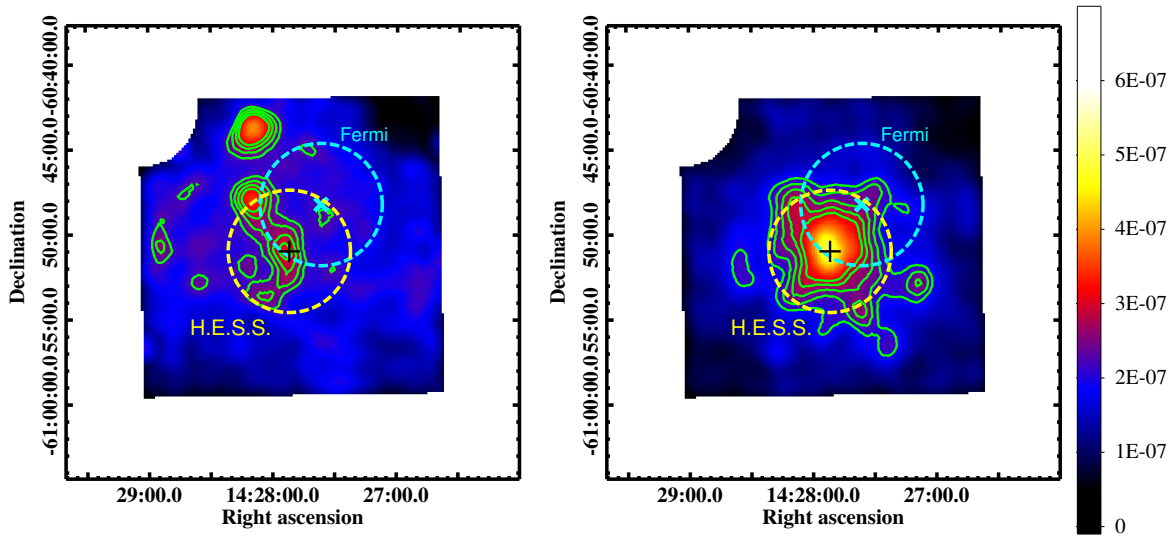

Figure 4.5: XIS images of the HESS J1427–608 field in the 0.5–2 keV (left) and the 2–8 keV (right) bands, respectively. The color bar indicates the surface brightness in units of count s^{-1} $pixel^{-1}$. The black cross and the dashed yellow circle indicate the position and the extent of the VHE source ($3'.6$ in radius), respectively. The cyan cross and the dashed cyan circle indicate the position and the error circle of 2FGL J1427.6–6048c ($3'.6$ in radius), respectively (Nolan et al., 2012). The green contours indicate the intensity of XIS image in linear scale. Adopted from Fujinaga et al. (2013).

center and the extent of HESS J1427–608 are shown as a black cross and a yellow dashed circle, respectively. A few faint, point-like sources are seen in the soft band, while an apparently extended source is detected in the hard band. The position and apparent extension of the hard source match those of HESS J1427–608. As will be shown in a later section, all the Suzaku soft-band sources may be explained by the point-like sources in the XMM-Newton archive data while the Suzaku hard-band source seems to be a truly new source. Thus, the central hard-band source was designated as Suzaku J1427–6051, and mainly focus on this source in the following analysis.

Because HESS J1427–608 and Suzaku J1427–6051 are both extended, we evaluate the X-ray

size of the source. For this purpose, careful estimation of the X-ray background is necessary since Suzaku J1427–6051 is relatively faint. In particular, this region contains significant contribution from the Galactic ridge X-ray emission (GRXE) as well as the cosmic X-ray background (CXB), both of which are subject to mirror vignetting effect resulting in a centrally-peaked spatial distribution. Therefore, it is not appropriate to assume a flat background image defined at an off-source region within the field of view (FOV). Instead, the GRXE+CXB image was estimated in the source region through Monte-Carlo simulation. Details of the X-ray background estimation are described below.

First, we estimated the surface brightness of the GRXE and CXB assuming their uniform distribution in the sky. For this purpose, we analyzed the X-ray spectrum in the off-source annulus region shown in figure 4.6. The region (between $6'.5$ and $7'.5$ from the center of Suzaku J1427–6051) was selected to minimize contamination from Suzaku J1427–6051. In other words, the off-source region contains only the GRXE and the CXB after the subtraction of NXB. Figure 4.7 shows the spectra extracted from the off-source region. The spectra were modeled by optically thin thermal three temperature plasma with neutral iron emission line plus the CXB following Uchiyama et al. (2009b). In the course of model fitting, the hydrogen column density was fixed to 1.54×10^{22} cm^{-2} determined by HI observations (Kalberla et al., 2005), the photon index of the CXB to 1.4, and the surface brightness of the CXB to 5.4×10^{-15} erg s^{-1} cm^{-2} arcmin^{-2} in the 2–10 keV band (Kushino et al., 2002). We made the ancillary response file using the FTOOL `xissimarfgen` assuming a uniform emission in the sky. The model could reproduce the observed spectrum well. The best-fit parameters are listed in table 4.4.

Next, we simulated the GRXE+CXB event data assuming uniform emission with the best-fit spectrum model determined above using the FTOOL `xissim` (Ishisaki et al., 2007). In order to avoid an extra ambiguity due to poor statistics, the exposure time for the simulation was set to 500 ks. Then we extracted the GRXE+CXB spectrum in the source region and added it to the NXB in the source region to obtain the total background spectrum, following the instruction in section 5.5.2 of the Suzaku technical description[6]. Figure 4.8 shows the simulated background spectra of the XIS1 and XIS3 respectively as well as the source and off-source spectra. As can be seen from the spectra, the source region contains significant emission above the GRXE+CXB level.

Figure 4.9 shows the radial profiles of the NXB-subtracted image and the simulated GRXE+CXB image in the 2–8 keV band. The difference is attributed to Suzaku J1427–6051. Even if we consider the relatively broad half-power radius ($1'.0$; Serlemitsos et al. 2007) of the point spread function of Suzaku mirror, Suzaku J1427–6051 is clearly extended. In order to estimate the

[6]http://heasarc.gsfc.nasa.gov/docs/suzaku/prop_tools/suzaku_td/node8.html#SECTION0085200000000000

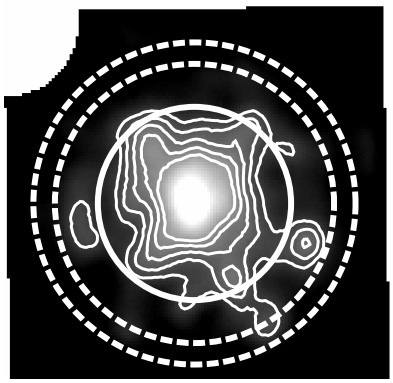

Figure 4.6: The source and the off-source regions are indicated in the XIS hard band image. The contours shown in figure 4.5 are also overlaid. The source region is defined within the circle of $r = 4'.5$ drawn by the solid line. The off-source region is defined as an annulus with an inner and an outer radius of $r = 6'.5$ and $r = 7'.5$ respectively, drawn by the dashed lines. Adopted from Fujinaga et al. (2013).

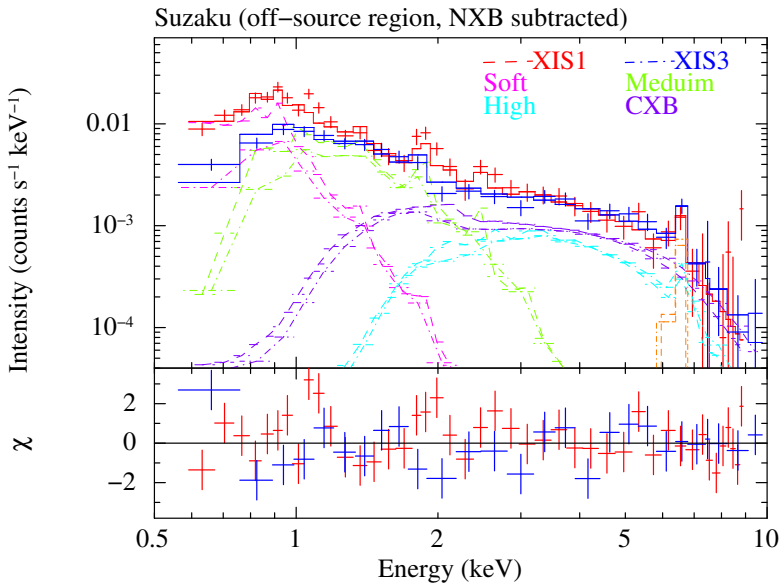

Figure 4.7: XIS spectra of the off-source region after NXB subtraction. Red and blue data represent XIS1 and XIS3 spectra, respectively. The best-fit model of thin thermal three temperature plasma with an iron emission line plus the CXB is also shown. Adopted from Fujinaga et al. (2013).

source extent, we compared the observed radial profile with that of a model calculation for an extended source having a 2D-gaussian distribution. Instead of performing the χ^2 fitting, we calculated χ^2 for a set of σ, i.e. $0'.5, 0'.7, 0'.8, 0'.9$, and $1'.1$. The simulated profiles were generated with `xissim`. It turned out that none of them gave an acceptable fit; the radial profile of

Table 4.4: The best-fit parameters of the observed XIS spectrum in the off-source region

	Soft	Medium	High
$N_{\rm H}$ (10^{22} cm^{-2})	$0.21^{+0.17}_{-0.16}$	$1.04^{+0.25}_{-0.19}$	$4.95^{+10.86}_{-1.49}$
kT (keV)	0.26 ± 0.06	$0.55^{+0.11}_{-0.08}$	$3.71^{+11.45}_{-1.53}$
Absorbed flux*	$0.86^{+1.58}_{-0.66}$	3.30 ± 1.06	$3.80^{+4.94}_{-1.90}$
		Abundance ($z_\odot$)	
Ne		0.57 (fixed)	
S		1.27 (fixed)	
Ar		2.10 (fixed)	
others		0.33 (fixed)	
Line E (keV)		$6.47^{+0.22}_{-0.07}$	
Line flux†		$7.0^{+3.9}_{-3.5}$	
χ^2/d.o.f		84.68 / 60	

* In units of 10^{-12} erg s^{-1} cm^{-2} in the 0.8–10 keV band.

† In units of 10^{-5} photons s^{-1} cm^{-2}.

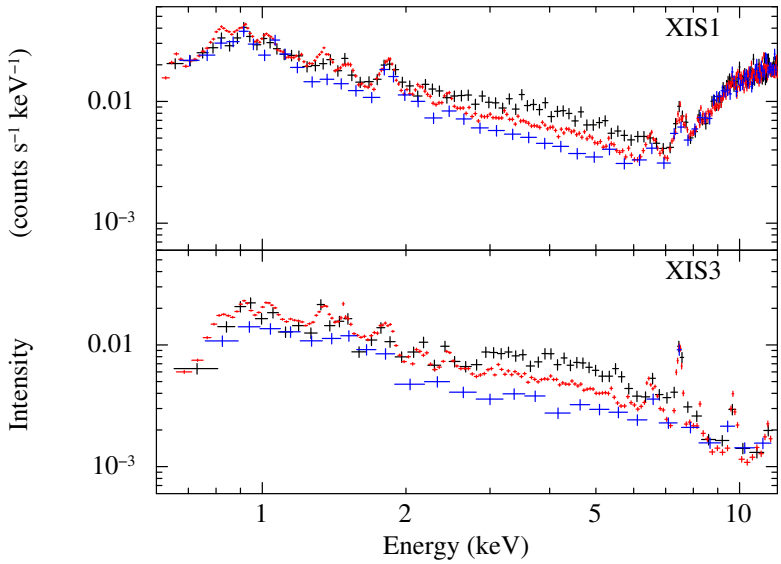

Figure 4.8: Comparison of the source spectrum (black) including the background, the background spectrum estimated for the source region (red), and the off-source spectrum (blue). The off-source spectrum is normalized considering the area difference of source and off-source regions. The upper and lower panels show spectra of XIS1 and XIS3, respectively. Adopted from Fujinaga et al. (2013).

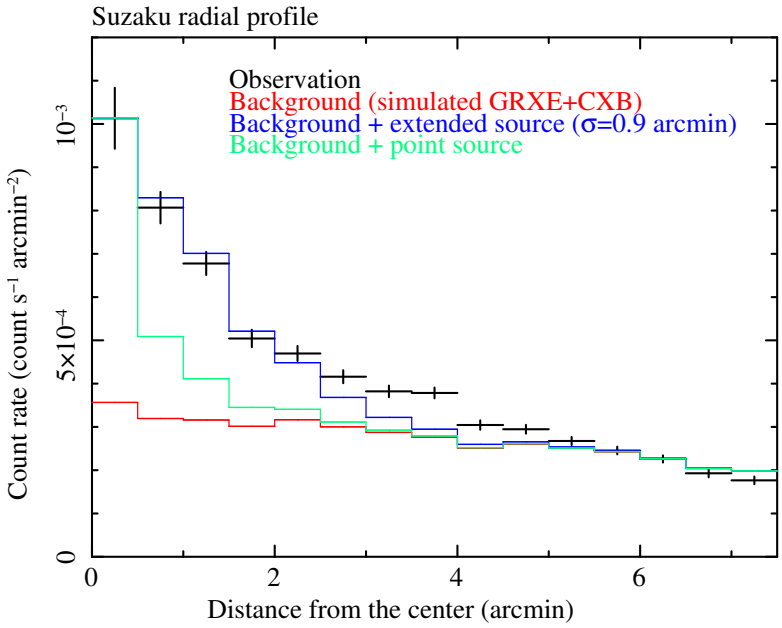

Figure 4.9: The NXB subtracted, GRXE and CXB included radial profiles of XIS in the 2–8 keV band. Black, red, blue and green lines represent the observed radial profile, the simulated radial profile of GRXE+CXB, that of an extended source with $\sigma = 0'.9$ and GRXE+CXB, and that of a point source and GRXE+CXB, respectively. Adopted from Fujinaga et al. (2013).

Suzaku J1427–6051 has a core and a tail in comparison with the best-fit simulation data. Thus the χ^2 test was performed using only the core region ($r < 2'.0$), and an acceptable fit ($\chi^2 = 0.6$ for 3 degrees of freedom) was obtained. The best-fit value obtained was $\sigma = 0'.9 \pm 0'.1$ with 90% confidence level.

Energy Spectra

Figure 4.10 shows the background-subtracted energy spectra of Suzaku J1427–6051. Here, the background spectrum (sum of GRXE, CXB, and NXB) was calculated with the method detailed above. It is found that the spectrum of Suzaku J1427–6051 is featureless and heavily absorbed. Although a hint of feature is seen in the 6–7 keV band, which may be due to the spacial variation of the iron emission line in GRXE, it is not statistically significant. The ancillary response file was calculated using the FTOOL `xissimarfgen` for an extended source of a Gaussian profile with $\sigma = 0'.9$. The spectrum was well modeled by either an absorbed power-law or a thermal model, whose best-fit parameters are listed in table 4.5. However, a thermal origin is unlikely because the abundance is unreasonably small, and the X-rays are thus considered to be produced by non-thermal processes. The absorbed X-ray flux of the source is 3.1×10^{-13} erg s^{-1} cm^{-2} in the 2–10 keV band.

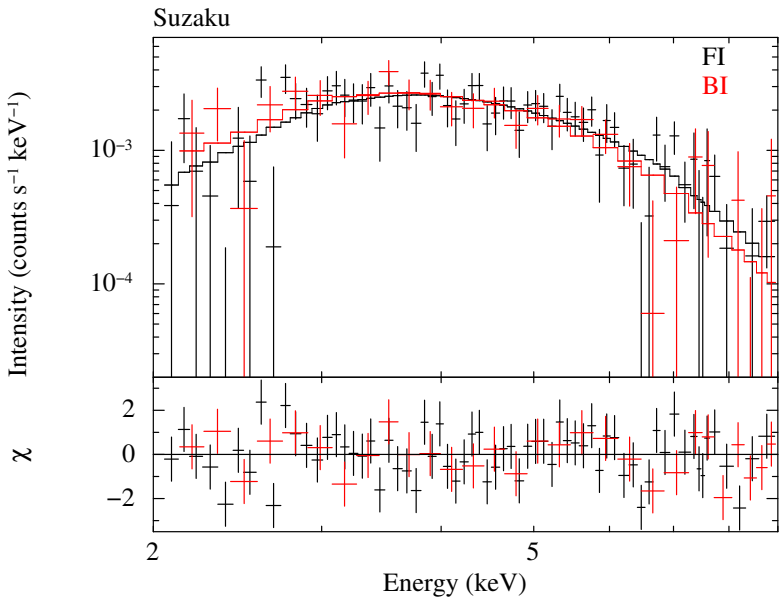

Figure 4.10: The background-subtracted energy spectra of Suzaku J1427–6051. Black and red crosses indicate data of FI CCDs (sum of XIS0 and XIS3) and BI CCD (XIS1), respectively. The solid lines show the best-fit absorbed power-law model. Adopted from Fujinaga et al. (2013).

The spectrum of the HXD was also analyzed to search for emission of Suzaku J1427–6051 above 10 keV. The background spectrum was used which is called "bgd_d" provided by the Suzaku team (Fukazawa et al., 2009). The CXB spectrum was added to it using the FTOOL `hxdpinnxbpi`. The XIS nominal-position response file categorized to epoch 6 was used, which is released as a CALDB. The background-subtracted spectrum was made and was fitted with a power-law, whose photon index was fixed to $\Gamma = 3.1$, as derived from the XIS analysis. The flux in the 15–40 keV band is $(1.6 \pm 1.1) \times 10^{-12}$ erg s^{-1} cm^{-2} (χ^2/d.o.f. = 35.21/27) if no systematic error is taken into account. Based on Fukazawa et al. (2009), who showed the reproducibility of NXB in the 15–40 keV band is about 3% in the 90% confidence range, we constructed the NXB spectra with 3% higher count rates to include the systematic error of the NXB reproduction. Then, a significant signal is no longer detected. We thus obtained the 90% upper limit of 5.3×10^{-12} erg s^{-1} cm^{-2} in the 15–40 keV band.

4.2.2 Analysis of XMM-Newton Archive Data

In order to estimate the contribution of point sources, we analyzed the archival data of XMM-Newton including the HESS J1427–608 field. The observation was carried out on 2007 August 9 for 24 ks. During the observation, EPIC was operated in full-frame mode with medium filter.

Table 4.5: The best-fit parameters of the background-subtracted XIS spectrum

	Power-law	APEC
$N_{\rm H}$ (10^{22} cm^{-2})	$11.1^{+2.9}_{-2.5}$	$9.0^{+2.2}_{-1.9}$
Γ	$3.1^{+0.6}_{-0.5}$	—
kT (keV)	—	$3.2^{+1.5}_{-0.8}$
Abundance ($z_\odot$)	—	< 0.09
Unabsorbed flux*	$8.9^{+3.6}_{-2.0}$	$6.6^{+4.7}_{-2.5}$
Absorbed flux*	3.1	3.0
χ^2/d.o.f.	64.02/71	62.89/70

Note: The errors are in the 90 % confidence range.

* In the 2.0–10.0 keV band in units of 10^{-13} erg s^{-1} cm^{-2}.

The data were analyzed with the Science Analysis Software (SAS) version 10.0.0, HEADAS version 6.10 and XSPEC version 12.6.0. Time intervals of enhanced background, which are caused by soft proton flares, were removed with thresholds of 0.20 count s^{-1} for MOS1, 0.24 count s^{-1} for MOS2, and 0.6 count s^{-1} for pn, respectively, calculated for PATTERN=0 events above 10 keV. We used X-ray events of PATTERN=0–12 (for MOS cameras) and PATTERN=0–4 (for pn camera) for the image and spectral analyses. The resultant effective exposures were 21 ks (MOS1), 22 ks (MOS2), and 15 ks (pn), respectively. The journal of the observation is listed in table 4.3.

Images

Figure 4.11 shows the summed images of MOS1 and MOS2 in the soft (0.3–2 keV) and the hard (2–12 keV) bands. The XIS images are also overlaid in green contours. Using the SAS tool `edetect_chain`, a total of 16 point sources were detected within 9′ from the center of Suzaku J1427–6051. Eleven and seven sources were found in the soft and the hard bands, respectively, and two sources were commonly detected in both bands. Summing up the count rates of the point sources located within the Suzaku source region (X1 through X7), we obtained $(3.4 \pm 0.4) \times 10^{-3}$ count s^{-1} in the 0.5–2 keV band. This may be converted to the XIS BI count rate of $(2.4 \pm 0.3) \times 10^{-3}$ count s^{-1} assuming the power-law spectrum in table 4.5. Because this is comparable to the rate actually observed with Suzaku ($(3.0 \pm 0.2) \times 10^{-3}$ count s^{-1}), the XIS data may be explained by the sum of the XMM-Newton point sources in the soft band. On the other hand, if we carry out a similar calculation for the hard band, the XMM-Newton point sources would produce 7×10^{-4} count s^{-1} in XIS. Because this corresponds to only $\simeq 8$ % of

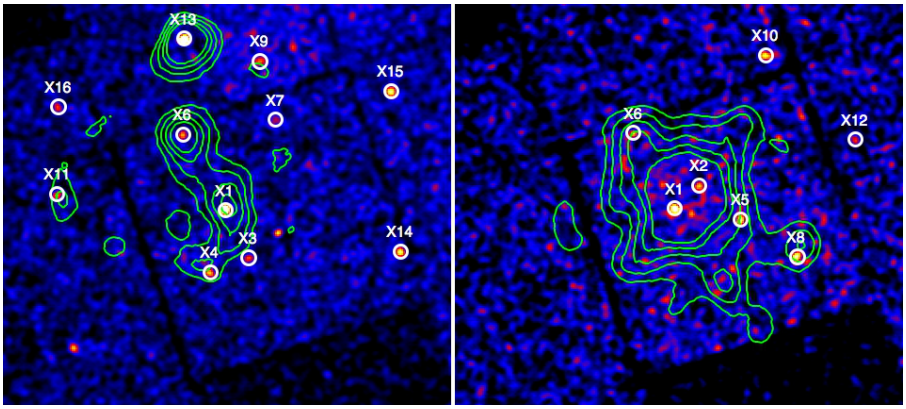

Figure 4.11: The summed MOS images of the HESS J1427–608 field in the 0.3–2 keV band (left) and in the 2–12 keV band (right), respectively. The green contours indicate the XIS images shown in figure 4.5. The white circles indicate the point sources detected by the SAS tool `edetect_chain`. Adopted from Fujinaga et al. (2013).

the actual XIS count rate, Suzaku J1427–6051 is difficult to be explained by the sum of the sources and may be a truly diffuse source.

Energy Spectra

The energy spectra of only X1 and of the summed spectra of the central seven point sources (X1 through X7) were calculated. The response file and the ancillary response file were generated using the SAS tool `rmfgen` and `arfgen`, respectively. These spectra were fitted with the model of an absorbed power-law. Because of the poor statistics, the photon index was fixed to 3.1, which was determined by the spectral analysis of Suzaku J1427–6051. The best-fit parameters are listed in table 4.6. The absorbed X-ray flux of the summed spectra was 1.7×10^{-14} erg s^{-1} cm^{-2} in the 2–10 keV band, which is about 5% of the flux derived with Suzaku for Suzaku J1427–6051. It is also found that the column density of the summed spectra is two orders of magnitude smaller than that derived for Suzaku J1427–6051. These results confirm that Suzaku J1427–6051 cannot be explained by the XMM-Newton point sources.

4.2.3 Discussion

Multi-Wavelength View of HESS J1427–608

An apparently-diffuse hard X-ray source, Suzaku J1427–6051 was discovered with Suzaku. In addition, several point sources were found with XMM-Newton in spatial coincidence with HESS J1427–608. Suzaku J1427–6051 could not be explained by the sum of the point sources

Table 4.6: The best-fit parameters of EPIC spectra

	X1	Sum of X1–X7
$N_{\rm H}$ (10^{22} cm^{-2})	< 0.3	0.3 ± 0.1
Γ	3.1 (fixed)	3.1 (fixed)
Unabsorbed flux*	$0.7^{+0.4}_{-0.2}$	$1.7^{+0.7}_{-0.6}$
Absorbed flux*	0.7	1.7
χ^2/d.o.f.	11.28 / 6	16.74 / 27

Note: The errors are in the 90 % confidence range.

* In the 2–10 keV band in units of 10^{-14} erg s^{-1} cm^{-2}.

detected with XMM-Newton, and concluded that it is a truly diffuse source. Even if time variability of the detected point-like sources is considered, it is unlikely that Suzaku J1427–6051 is explained by them because the hydrogen column densities are quite different. The XMM-Newton point sources are most likely foreground sources. To explain Suzaku J1427–6051 by the sum of several point sources would require that all those sources would be below detection threshold at the time of the XMM-Newton observation, which appears very unlikely. Thus, Suzaku J1427–6051 is an intrinsically diffuse source and the X-ray counterpart of HESS J1427–608.

Next, various catalogs and literature for the possible counterpart of HESS J1427–608 were searched in other wavebands. A GeV gamma-ray source, 2FGL J1427.6–6048c, is listed in the 2-year catalog of Fermi (Nolan et al., 2012). The GeV source is located at $l = 314^\circ.3953, b = -0^\circ.0909$, which is $3'.3$ away from the center of HESS J1427–608 (see figure 4.5). Since the error radius of the position is about $3'.6$, it may be associated with HESS J1427–608 (Nolan et al., 2012). However, this is a "c-designator-applied" Fermi source whose position, emission characteristics, or even existence may not be reliable due to a potential confusion with interstellar emission (Nolan et al., 2012). It may be premature to discuss a possible association of the GeV source to HESS J1427–608; future Fermi data and analysis is necessary.

Possible Nature of HESS J1427–608

Although HESS J1427–608 was thought to be one of the unID sources in the introduction, its center-filled morphology and featureless spectrum in the X-ray band suggest that the source could be a PWN. Thus, the source may be a PWN as a working hypothesis. Figure 4.12 shows the spectral energy distribution (SED) from X-rays to VHE gamma-rays. The estimated synchrotron spectra from the VHE gamma-ray spectrum (Aharonian et al., 2008a), assuming

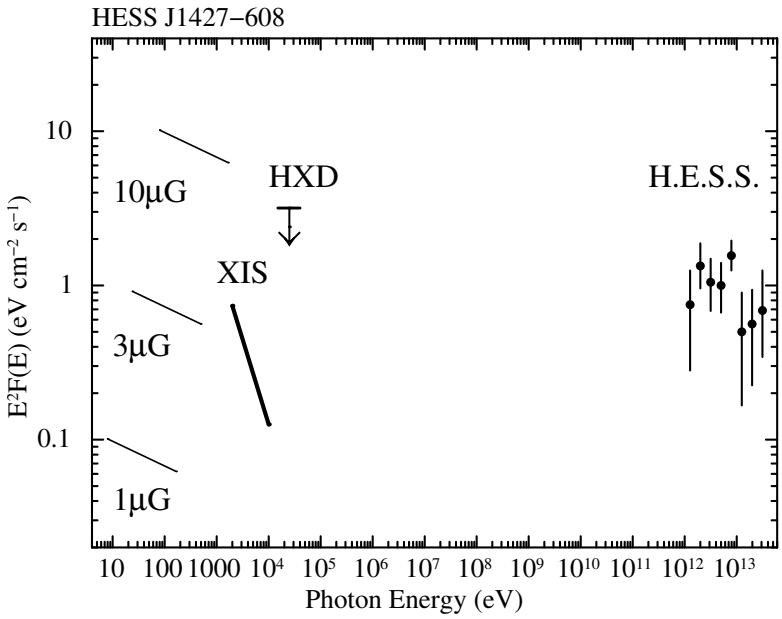

Figure 4.12: Spectral energy distribution of HESS J1427–608 from X-ray through VHE gamma-ray is shown (Fujinaga et al., 2013). The calculated spectra of the synchrotron emission are overlaid. The H.E.S.S. spectrum is taken from Aharonian et al. (2008a).

that the same electron population would inverse-Compton scatter CMB photons up to VHE gamma-rays and radiate synchrotron emission in X-rays, are also plotted with a local magnetic field B of 1, 3, and 10 μG. This SED plot indicates that the simple one-zone leptonic model with B of about 5 μG would roughly explain both the X-ray and VHE gamma-ray data. In this context, the steep Suzaku spectrum of $\Gamma \simeq 3.1$ could indicate that the Suzaku energy band is higher than the cut-off energy. The inferred magnetic field strength of $\simeq$5 μG is within the range of typical values on the Galactic plane. Thus the SED is consistent with a one-zone leptonic model expected for PWNe. The X-ray to VHE gamma-ray ratio is useful to probe the nature of unID sources (Yamazaki et al., 2006). In the case of HESS J1427–608, the unabsorbed X-ray flux $F_{\rm X}$ of 8.9×10^{-13} erg s^{-1} cm^{-2} (2–10 keV) and the VHE gamma-ray flux $F_{\rm TeV}$ of 4.0×10^{-12} erg s^{-1} cm^{-2} (1–10 TeV) result in a flux ratio of $F_{\rm TeV}/F_{\rm X} \simeq 4.5$. If we assume a distance to HESS J1427–608 of $d = 8$ kpc, the X-ray luminosity would be $L_{\rm X} = 7 \times 10^{33}$ erg s^{-1}. The estimated flux ratio and X-ray luminosity are within the values of known X-ray and VHE gamma-ray emitting PWNe, given that both values show a large scatter: $10^{-3} - 10^{2}$ in $F_{\rm TeV}/F_{\rm X}$ and $10^{32} - 10^{37}$ erg s^{-1} in $L_{\rm X}$ (Mattana et al., 2009). Thus the flux ratio and luminosity are also consistent with sources of PWN origin.

While there are observational evidences supporting the PWN origin as discussed above, others challenge such a view. With the assumption of $d = 8$ kpc, the core size and whole radial extent would be 2 pc and 12 pc, respectively. The core size of 2 pc is a little large, but not

exceptional among other PWN (Kargaltsev & Pavlov, 2008). The whole extent of 12 pc is not surprisingly large compared with the nebula of e.g., PSR J1826–1334 (Uchiyama et al., 2009b). The largest drawback of the PWN hypothesis is lacking the detection of both a pulsar and radio PWN associated. It is known that the pulsar luminosity and its nebula luminosity in the X-ray band are correlated over 7 orders of magnitude (Kargaltsev & Pavlov, 2008). According to the correlation, the not-yet-detected pulsar should be brighter than $\sim 10^{-13}$ erg s^{-1} cm^{-2} in X-rays, one-tenth of the PWN luminosity. Such a pulsar would have been easily detected with XMM-Newton. In addition, the X-ray photon index of the nebula ($\Gamma = 3.1$) is very steep among the known X-ray nebulae most of which have a Γ between 1.2–2.2 (Kargaltsev & Pavlov, 2008).

In terms of photon index comparison, non-thermal SNRs might present a more plausible scenario than PWNe. Most of non-thermal SNRs radiate synchrotron X-rays with a photon index of $\Gamma = 2.4 - 3.1$ (Nakamura et al., 2009). The X-ray luminosity and extent are also compatible to synchrotron SNRs (Nakamura et al., 2012). However, the facts that the source has a center-filled morphology in the X-ray band and no detection of the shell structure in the radio band hamper the interpretation as a non-thermal SNR.

4.3 Conclusion of These Two Follow-up Observations

In this chapter, analyses of the X-ray follow-up observations of two unID VHE gamma-ray sources were presented. In addition, their possible natures were discussed.

One of the brightest VHE gamma-ray sources, HESS J1702–420 was observed with Suzaku.

- Even though the deep exposure (216 ks), no plausible X-ray counterpart was found.
- Considering the systematic error of the background subtraction, no significant diffuse emission was detected with an upper limit of $F_{\rm X} < 2.7 \times 10^{-12}$ erg s^{-1} cm^{-2} in the 2–10 keV band for an assumed power-law of $\Gamma = 2.1$ and a source size same as that in the VHE gamma-ray band.
- The large flux ratio ($F_{\rm TeV}/F_{\rm X} > 12$) indicates that HESS J1702–420 is another example of a "dark" particle accelerator.
- Because the obtained magnetic field ($B < 1.7$ μG) is lower than the typical value in the Galactic plane (3–10 μG), the simple one-zone model may not work for HESS J1702–420 and a significant fraction of the VHE gamma-rays may originate from protons.

HESS J1427–608 was observed with Suzaku. Combining the Suzaku analysis with that of archive data of XMM-Newton, following results were obtained.

- We discovered an X-ray counterpart, Suzaku J1427–6051, of HESS J1427–608. It is intrinsically extended ($\sigma = 0'.9 \pm 0'.1$) and has an energy spectrum described as an absorbed power-law with a photon index of $\Gamma = 3.1^{+0.6}_{-0.5}$.

- Several faint point sources were found in the emission region of HESS J1427–608 using XMM-Newton archive data.

- Observational properties of Suzaku J1427–6051 and HESS J1427–608 are compared with those of known PWNe and non-thermal SNRs. Some properties favor the PWN and/or SNR origin, but the available data are insufficient to draw firm conclusions.

Chapter 5

X-ray and VHE Gamma-ray Spectral Analysis of PWNe

As reviewed in chapter 2, PWNe occupy the largest fraction of the VHE gamma-ray sources. Both VHE gamma-rays and X-rays are detected not only from young PWNe but also from old ones ($\tau_c \sim 100$ kyr). Assuming the leptonic process, we can estimate physical parameters of the PWNe, such as the magnetic field strength and the number density of electrons, with the X-ray and VHE gamma-ray data. In this chapter, X-ray and VHE gamma-ray emitting PWNe are selected and their magnetic and electron energy contents are estimated through the analysis of spectral energy distribution (SED).

5.1 Properties of the VHE Gamma-ray and X-ray emitting PWNe

Table 5.1 lists PWNe and candidates of PWN, from which both X-rays and VHE gamma-rays are detected. First, I selected PWNe listed in the online catalog for VHE gamma-ray astronomy, tevcat[1]. The catalog lists a type of the sources based on published journals. Among these VHE gamma-ray PWNe, I picked up the sources whose X-ray counterpart is present within three times the VHE gamma-ray extent. Here the source extent is defined by σ of the best-fit Gaussian profile. With these criteria, a total of 16 PWNe were selected. According to the ATNF pulsar catalog (Manchester et al., 2005), all these VHE gamma-ray sources have associated pulsars. Some of these sources may reside in a shell structure of the SNR. Because the shell of the SNR could be a gamma-ray of X-ray emitter, I consulted a Galactic SNR catalog by Green[2]. When an associated SNR is present, I compared the size of SNR in the catalog, which is measured

[1] http://tevcat.uchicago.edu/

[2] http://www.mrao.cam.ac.uk/surveys/snrs/index.html

in radio band, with that of the VHE gamma-rays. If the SNR size is smaller than the VHE gamma-ray size, I classified the source as "composite". Otherwise, the source is classified as "PWN". Contribution from the shell could be present in the composite sources. Such a possibility is discussed for individual sources in sections 5.3.12–5.3.16. In addition to the 16 sources, HESS J1427–608 and HESS J1702–420 are also included to compare their nature with that of PWNe.

Table 5.2 lists the parameters of the pulsars associated to the PWNe listed in table 5.1. Pulse periods P, pulse period derivatives $\dot{P}$ and distances d are adopted from the ATNF catalog, except for Fermi and X-ray pulsars. d of radio pulsars is derived from the dispersion measure. On the other hand, distances to Fermi and X-ray pulsars are inferred from various data described in the literature. Details are described in section 5.3. If a braking index n is not available from literature, I assume $n = 3$ as a dipole magnetic field radiation. Characteristic ages $\tau_{\rm c}$, spin down luminosities $\dot{E}$, and surface magnetic field $B_{\rm s}$ are calculated using P and $\dot{P}$ for the dipole configuration of the magnetic field. Distances from the Galactic center $D_{\rm G}$ is derived from coordinates of the pulsar and its distance d, assuming that the Galactic center is located at 8.5 kpc from the Sun. $D_{\rm G}$ is used for estimating the energy density of interstellar radiation field (ISRF), which is explained in section 5.2. The associated pulsar of HESS J1427–608 and HESS J1702–420 is not known yet. Thus I used distance in chapter 4 also in this section.

Table 5.3 lists the spectral and image properties of the selected sources in the VHE gamma-ray and the X-ray bands. In the VHE gamma-ray band, photon indices $\Gamma_{\rm TeV}$, fluxes in the 1–10 TeV band $F_{\rm TeV}$ and source extent $\sigma_{\rm TeV}$ are adopted from the literature. Because the VHE gamma-ray data were usually represented by a power-law in spectrum and a gaussian profile in an image, it was straightforward to obtain uniform description of the VHE gamma-ray spectra and images. In the X-ray band, photon indices $\Gamma_{\rm X}$, fluxes in the 2–10 keV band $F_{\rm X}$ were adopted from references. Most of these sources, the source extent was adopted from Anada (2009b) or Bamba et al. (2010), in which the best-fit Gaussian $\sigma_{\rm X}$ to the projected profile was listed. Crab and G0.9+0.1 are not extended in the VHE gamma-ray band. Thus, $\sigma_{\rm TeV}$ of them were left blank. In addition, the VHE gamma-ray size of Kes 75, and G21.5–0.9 were not available in the literature. Also, neither $\sigma_{\rm TeV}$ nor $\sigma_{\rm X}$ of HESS J1718–385, G0.9+0.1 and G54.1+0.3 were available. $R_{\rm TeV}$ and $R_{\rm X}$ are source radii in the VHE gamma-ray and the X-ray bands, respectively, in unit of pc. They are calculated as 3σ extent using the distance d to the pulsar.

Table 5.1: List of sources selected for the X-ray and VHE gamma-ray analysis

#	Source Name	Type	Associated Pulsar	References
1	Vela X	PWN	PSR J0835–4510	1 2 3 4 5
2	Crab Nebula	PWN	PSR J0534+2200	6 7 8 9
3	HESS J1356–645	PWN	PSR J1357–6429	10 11
4	HESS J1809–193	PWN	PSR J1809–1917	12 13 14 15
5	HESS J1825–137	PWN	PSR J1826–1334	14 15 16 17
6	HESS J1718–385	PWN	PSR J1718–3825	11 14 18
7	MSH 15–52	PWN	PSR J1513–5908	14 15 19 20 21
8	Kookaburra/Rabbit	PWN	PSR J1418–6058	4 22 23 24
9	Kookaburra/K3	PWN	PSR J1420–6048	14 15 22 23
10	G0.9+0.1	PWN	PSR J1747–2809	25 26 27
11	HESS J1837–069	PWN	AX J1838.0–0655	15 28 29 30
12	HESS J1708–443	Composite	PSR J1709–4429	31 32 33
13	G54.1+0.3	Composite	PSR J1930+1852	34 35 36
14	Kes 75	Composite	PSR J1846–0258	14 15 37 38 39
15	HESS J1813–178	Composite	PSR J1813–1749	28 40 41
16	G21.5–0.9	Composite	PSR J1833–1034	15 42 43 44 45
17	HESS J1427–608	PWN?	(none)	46 47
18	HESS J1702–420	Dark	(none)	46 48

References. [1] Aharonian et al. (2006c), [2] Dodson et al. (2003), [3] LaMassa et al. (2008), [4] Anada (2009b), [5] Lyne et al. (1996), [6] Aharonian et al. (2004b), [7] Kirsch et al. (2005), [8] Trimble (1973), [9] Lyne et al. (1993), [10] Abramowski et al. (2011b), [11] Camilo et al. (2004), [12] Aharonian et al. (2007), [13] Anada et al. (2010), [14] Manchester et al. (2005), [15] Bamba et al. (2010), [16] Aharonian et al. (2006d), [17] Uchiyama et al. (2009b), [18] Hinton et al. (2007b), [19] Aharonian et al. (2005b), [20] Gaensler et al. (2002), [21] Livingstone & Kaspi (2011), [22] Aharonian et al. (2006e), [23] Kishishita et al. (2012), [24] Ray et al. (2011), [25] Aharonian et al. (2005c), [26] Porquet et al. (2003), [27] Camilo et al. (2009), [28] Aharonian et al. (2006a), [29] Anada et al. (2009a), [30] Gotthelf and Halpern (2008), [31] Abramowski et al. (2011c), [32] Romani et al. (2005), [33] Johnston et al. (1992), [34] Acciari et al. (2010), [35] Bocchino et al. (2010), [36] Camilo et al. (2002), [37] Terrier et al. (2008), [38] Helfand et al. (2003), [39] Livingstone et al. (2007) [40] Gotthelf and Halpern (2009), [41] Funk et al. (2007), [42] Djannati-Atai et al. (2007), [43] Tsujimoto et al. (2011), [44] Camilo et al. (2006), [45] Roy et al. (2012), [46] Aharonian et al. (2008a) [47] Fujinaga et al. (2013), [48] Fujinaga et al. (2011)

Table 5.2: Properties of the pulsars associated to the selected sources

#	P	$\dot{P}$	n^*	$d^\dagger$	$\tau_c{}^\ddagger$	$\dot{E}$	$B_s{}^\S$	$D_G{}^\parallel$	Note
	ms	s s^{-1}		kpc	kyr	erg s^{-1}	10^{12} G	kpc	
1	89	1.3×10^{-13}	1.4	0.29	11	6.9×10^{36}	3.4	8.5	
2	33	4.2×10^{-13}	2.51	2.0	1.2	4.6×10^{38}	3.8	10.5	
3	166	3.6×10^{-13}	(3)	4.1	7.3	3.1×10^{36}	7.8	6.7	
4	83	2.6×10^{-14}	(3)	3.7	52	1.8×10^{36}	1.5	4.9	
5	102	7.5×10^{-14}	(3)	4.1	22	2.8×10^{36}	2.8	4.7	
6	75	1.3×10^{-14}	(3)	4.2	90	1.8×10^{36}	1.0	4.4	
7	151	1.5×10^{-12}	2.83	5.8	1.6	1.7×10^{37}	15	5.5	
8	111	1.7×10^{-13}	(3)	(5.0)	10	5.0×10^{36}	4.4	(6.3)	Fermi pulsar
9	68	8.3×10^{-14}	(3)	7.7	13	1.0×10^{37}	2.4	6.4	
10	52	1.5×10^{-13}	(3)	(10)	5.3	4.3×10^{37}	2.9	(1.5)	
11	70	4.9×10^{-14}	(3)	(6.6)	23	5.0×10^{36}	1.9	(3.8)	X-ray pulsar
12	102	9.3×10^{-14}	(3)	2.3	17	3.4×10^{36}	3.1	6.8	
13	136	7.5×10^{-13}	(3)	5.0	2.9	1.2×10^{37}	1.0	6.9	
14	326	7.1×10^{-12}	2.65	5.1	0.7	8.1×10^{36}	49	4.8	
15	44	1.5×10^{-13}	(3)	(4)	4.7	6.8×10^{37}	2.6	(4.1)	X-ray pulsar
16	61	2.0×10^{-13}	1.86	(4.8)	4.8	3.4×10^{37}	3.6	(4.8)	
17				(8)				(7.3)	No known pulsar
18				(1)				(7.5)	No known pulsar

* Braking index of the pulsar. When it is not available in the literature, a value in the parenthesis, which is expected for the dipole magnetic radiation, is assumed.

† In most cases, distance derived from the dispersion measure of the pulsar was adopted. Values in the parenthesis mean assumed distances (see details in section 5.2).

‡ Characteristic age derived with equation (2.40).

§ Magnetic field strength at the surface of pulsar derived with equation (2.42).

‖ Estimated distance from the Galactic center.

5.2 Method

I estimate number density of relativistic electrons, which are responsible for both X-ray and VHE gamma-ray emission, and the magnetic field strength from the data compiled in the previous section. For this purpose, I calculate a model spectrum to reproduce the wide-band spectrum. Many of the calculation of X-ray and VHE gamma-ray spectra published so far are carried out based on the "one-zone" model. This model assumes that (i) both VHE gamma-

Table 5.3: VHE gamma-ray and X-ray properties of the selected sources

#	$\Gamma_{\rm TeV}$	$F_{\rm TeV}$*	$\Gamma_{\rm X}$	$F_{\rm X}$†	$F_{\rm TeV}/F_{\rm X}$	$\sigma_{\rm TeV}$‡	$R_{\rm TeV}$§	$\sigma_{\rm X}$‖	$R_{\rm X}$**
1	1.4	55	2.2	20	2.8	26	6.5	24	6.0
2	2.4	76	2.1	19000	0.004	–	–	–	–
3	2.2	8	1.8	2.1	3.8	12	25	2.6	5.4
4	2.2	18	1.7	5.9	3.1	15	48	6.8	23
5	2.4	49	2.0	5	9.8	15	50	3.2	11
6	0.7	2.9	1.9	< 0.1	> 22	6.1	23	–	–
7	2.3	18	2.1	37	0.4	4.0	15	1.6	5.9
8	2.2	7.7	1.8	2.6	2.9	3.3	14	1.5	6.5
9	2.2	11	2.0	1.5	7.2	3.6	18	1.5	7.3
10	2.4	2.0	2.0	5.8	0.3	–	–	–	–
11	2.3	14	1.6	1.0	14	4.6	26	1.3	7.2
12	2.0	17	1.8	0.4	42	17	35	0.6	1.2
13	2.4	1.8	1.8	7.5	0.2	1.8	9.7	–	–
14	2.3	1.7	1.9	28	0.06	–	–	0.6	3.5
15	2.1	9.0	1.9	6.9	1.3	2.4	9.8	0.4	1.4
16	2.1	1.5	1.9	56	0.03	–	–	0.7	2.7
17	2.1	4.0	3.1	0.9	4.5	3.6	31	0.9	7.9
18	2.1	31	(2.1)	< 2.7	> 12	30	18	–	–

* Energy flux in the 1–10 TeV band in units of 10^{-12} erg s^{-1} cm^{-2}.

† Unabsorbed energy flux in the 2–10 keV band in units of 10^{-12} erg s^{-1} cm^{-2}.

‡ Angular size of the VHE gamma-ray emission region, approximated by a Gaussian in unit of arcminute.

§ Estimated 3σ radius of VHE gamma-ray emission region in unit of pc. Distance to VHE emission region is assumed to be same as that to the associated pulsar.

‖ Angular size of the X-ray emission region, approximated by a Gaussian in unit of arcminute.

** Estimated 3σ radius of X-ray emission region in unit of pc. Distance to X-ray emission region is assumed to be same as that to the associated pulsar.

rays and X-rays are emitted from the same population of electrons, meaning that the energy spectrum, number density, and spacial extent are common for VHE gamma-ray and X-ray emitting electrons, and (ii) magnetic field and electrons are uniformly distributed in the emission region. Furthermore, only the CMB is considered as the seed photons of the inverse Compton scattering in most cases. However, most of the observed spectra could not be reproduced by the one-zone model adequately, especially the maximum energy of electrons seem to be different

between the IC and the synchrotron spectra. Also, the size of the emission region is different between the X-ray and the VHE gamma-ray bands. These results imply that the populations of relativistic electrons contributing to the IC and the synchrotron emission are different.

Considering these situation, I assumed three types of model for the structure of the emission regions. Figure 5.1 shows the models. The type 1 is a simple one-zone model. Type 2 and type 3 are what is called two-zone models. In the two-zone models, the inner zone represents the X-ray (and the VHE gamma-ray) emission region and the outer zone represents the VHE gamma-ray emission region. In the type 2 model, only a single parameter is assumed to be different between the two zones. This leads to two possibilities. One is that the maximum energy (cut-off energy) of electrons is different. Between these possibilities, I consider the case that the cut-off energy is different, because the other case failed to reproduce the VHE gamma-ray and X-ray spectra simultaneously for most sources. Simple consideration can explain the reason. If we assume a power-law spectrum of electrons (index of p), both the inverse Compton scattering and synchrotron radiation produce emission with a power-law spectrum of an photon index of $(p-1)/2$, as explained in section 2.2.1. This means that the VHE gamma-ray and X-ray spectra should have the same slope. This does not hold in most of the sources. Thus I assume that the cut-off energy of electrons is different between the inner and outer zones in the type 2 model. As see later, this type 2 model can in fact reproduce the VHE gamma-ray and X-ray spectra simultaneously for most of the sources. The type 3 is assumed that the magnetic field strengths are also different between the inner and outer zones in addition to the electron cut-off energy. In all types of the models, I considered infrared emission of interstellar radiation field (ISRF) as the seed photons of IC scattering in addition to the CMB. If the size of the emission region is unknown, I carry out the calculation using the type 1 model. If the sizes of the emission regions in both the X-ray and the VHE gamma-ray bands are known, I start the analysis with the type 2 model. Then, if the model could not reproduce the observed spectra, I switch to type 3.

The calculation was based on the code developed by Kataoka (2000), but I modified the code to incorporate (i) the size difference between the VHE gamma-ray and X-ray emission regions, (ii) additional seed photons of ISRF for IC spectrum, and (iii) difference of cut-off energy in the electron spectrum between the VHE gamma-ray and X-ray emission regions. Assumptions of the model and the calculation procedure of a model spectrum are summarized below.

Assumptions of the Model

1. VHE gamma-rays and X-rays are produced by relativistic electrons through IC scattering of seed photons and synchrotron radiation, respectively.

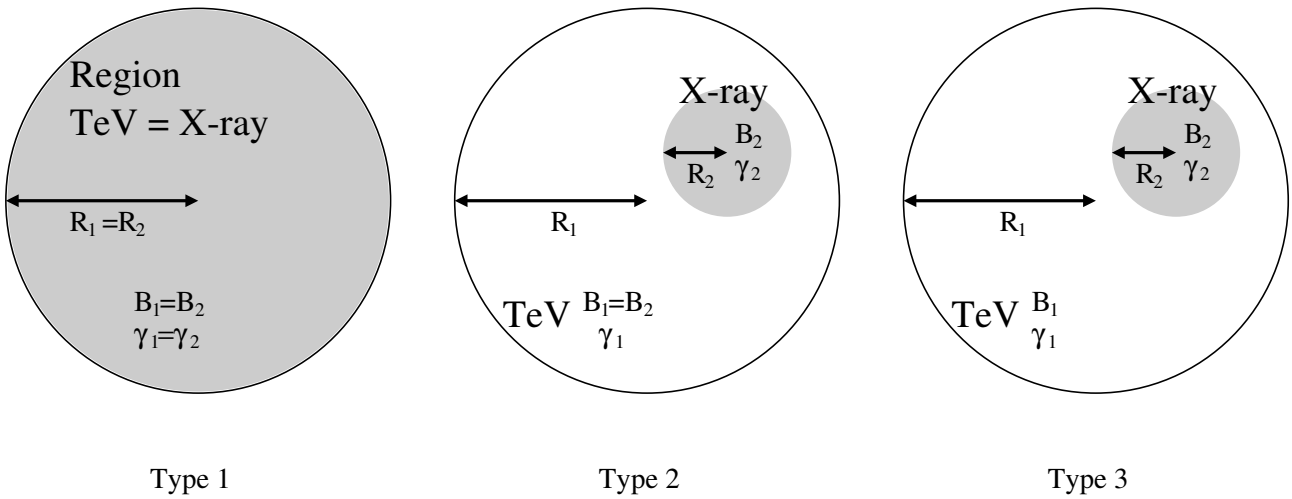

Figure 5.1: The assumed structures of PWNe for the spectrum calculation. The VHE gamma-ray emission region is a sphere with a radius of R_1. Within the VHE gamma-ray extent, the X-ray emission region exists in a sphere with a radius of R_2 (the gray circle). In the type 1, $R_1 = R_2$, $\gamma_1 = \gamma_2$ and $B_1 = B_2$ are assumed. In the type 2, $B_1 = B_2$ is assumed.

2. The emission regions are assumed to be a sphere with a radius of R_1 for VHE gamma-ray and R_2 for X-ray. Note that both X-ray and VHE gamma-ray are emitted from the sphere R_2. I used $R_{\rm TeV}$ and $R_{\rm X}$ for R_1 and R_2, respectively. If either $R_{\rm TeV}$ or $R_{\rm X}$ is not available in the literature, I assumed adequate values inferred from the available information. Note that R_1 is equal to or larger than R_2 according to the past observations. Furthermore, I assume that the sphere of R_2 (X-ray emission region) is included in the sphere of R_1 (VHE gamma-ray emission region) for simplicity.

3. Relativistic electrons has a power-law spectrum with an index of $p = 2.0$, which cuts off exponentially at higher energy. In the outer region (in which only VHE gamma-rays are emitted), the cut-off energy is defined as γ_1 (i.e., electrons having an exponential cut-off at γ_1 occupy the volume of $4\pi(R_1^3 - R_2^3)/3$). On the other hand, in the inner region (in which both X-rays and VHE gamma-rays are emitted), the cut-off energy is defined as γ_2. The cut-off energy γ_2 is equal to or larger than γ_1. The normalization of the electron spectrum $N_{\rm e}$, defined as by the number density per γ, is assumed to be same in the whole region. For the type 1, the cut-off energies are common, i.e. $\gamma_1 = \gamma_2$. In the type 2 and type 3 model, X-ray emission is produced only from the sphere R_2, not from the sphere R_1, because relativistic electrons energetic enough to produce X-rays through synchrotron emission are absent in the sphere R_2 due to relatively low cut-off energy. Figure 5.2 shows the electron spectrum of HESS J1837–069 as an example. In this case, the VHE gamma-ray emission is originated from the electrons with $\gamma \sim 10^7$, whereas the X-ray emission

from the electrons with $\gamma \sim 10^8$. The size difference of the emission region between the X-ray and VHE gamma-ray is explained by the difference of the cut-off energies.

4. Magnetic field is assumed to be uniformly distributed with strength of B_1 in the sphere R_1, except for inside the sphere R_2 (the inner region) which has uniform magnetic field of B_2. In the type 1 and type 2 models, the magnetic field is same for the whole nebula, i.e. $B_1 = B_2$. When the size difference of X-ray and VHE gamma-ray emission region is very large, synchrotron emission from the VHE gamma-ray region becomes non-negligible even for the difference of the cut-off energy. If it happens, $B_1 \neq B_2$ is assumed by adopting type 3 to reduce the contribution of synchrotron emission from the outer region.

5. Seed photons of IC is assumed to be CMB and ISRF. CMB is approximated by a black-body radiation of $T = 2.7$ K and the energy density of 0.5 eV cm^{-3}. ISRF consists of optical emission from stars and infrared emission from warm dust. The energy density of optical emission and that of infrared emission are almost same when the distance from the Galactic center $D_{\rm G}$ is smaller than 8 kpc, according to Porter et al. (2006). However, number density of optical photons should be about 100 times smaller than that of infrared photons, because of the difference of the temperature ($T_{\rm IR} \simeq 40$ K versus $T_{\rm optical} \simeq 1000$ K). Thus, the scattering probability of optical photons is much smaller than that of infrared photons, which enables us to ignore the contribution of optical photons. According to Porter et al. (2006), the energy density of the infrared emission depends on $D_{\rm G}$. I assume the energy density of $U_{\rm IR} = 2.0$ eV cm^{-3} for $D_{\rm G} < 5$ kpc, $U_{\rm IR} = 1.0$ eV cm^{-3} for $5 < D_{\rm G} < 7$ kpc, and $U_{\rm IR} = 0.5$ eV cm^{-3} for $D_{\rm G} > 7$ kpc, respectively.

Calculation Procedure

1. When the sizes of the emission regions are assumed to be same, i.e. $R_1 = R_2$, the type 1 model is adopted. On the other hand, if $R_1 \neq R_2$, I start with the type 2 model. In either case, calculation procedure is basically same.

2. Based on the assumptions of 1, 2, 3 and 5, I determine the normalization of the electron spectrum $N_{\rm e}$ to reproduce the observed VHE gamma-ray flux.

3. Simultaneously, I determine the cut-off energy γ_1 to reproduce the spectral shape in the VHE gamma-ray band.

4. Based on the assumptions of 1 through 4, I estimate the magnetic field strength $B_1 (= B_2)$ to reproduce the observed X-ray flux approximately. In the case of the type 1 model, go

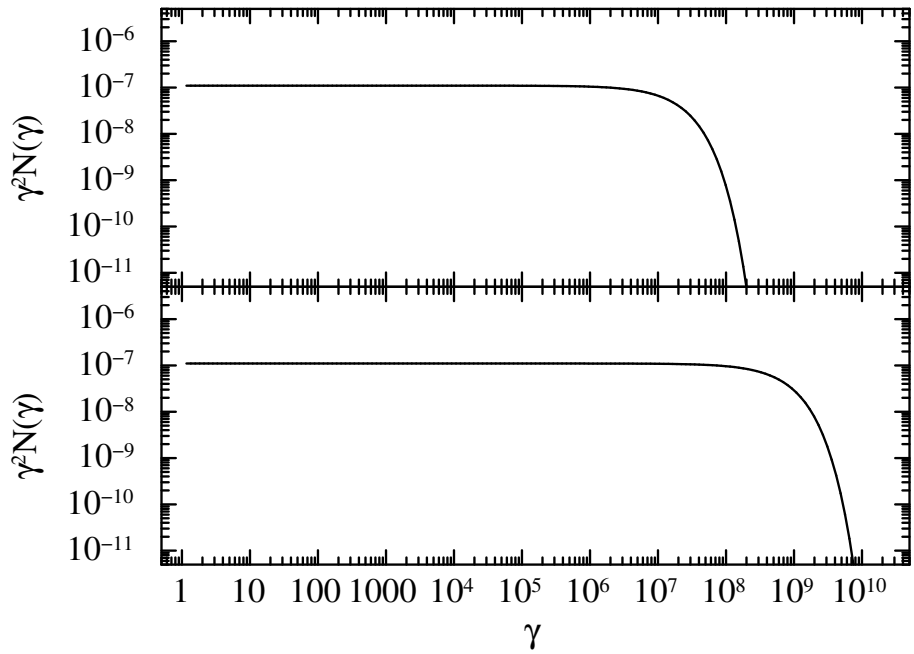

Figure 5.2: Electron spectra assumed for of HESS J1837–069. The ordinate of the plots is expressed by $\gamma^2 \times N(\gamma)$ as the power-law spectrum of $N(\gamma) \propto \gamma^{-2}$ becomes constant below the cut-off energy. The upper panel shows the spectrum with the cut-off at $\gamma_1 = 2.0 \times 10^7$ and the lower panel at $\gamma_2 = 7.5 \times 10^8$, respectively. The former represents the electron spectrum for the emission region of the VHE gamma-ray only, and the latter for the X-ray (and the VHE gamma-ray) emission region. The normalization is $N_{\rm e} = 1.1 \times 10^{-7}$ cm^{-3} γ^{-1} in both plots.

to procedure 9.

5. Simultaneously, I determine the cut-off energy γ_2 to reproduce the spectral shape in the X-ray band.

6. I repeat the procedures 2 through 5 until the model spectrum becomes consistent with the observed spectra. When the model spectrum shows a good agreement, skip to procedure 9.

7. If the model spectrum fails to reproduce the observed spectrum, I switch to type 3 model instead of type 2.

8. Go to the procedure 4 to determine (an upper limit of) B_2.

9. Finally, I estimate the total energy of electrons $E_{\rm e}$ and that of magnetic field $E_{\rm B}$ using the best-fit parameters.

The total energies are calculated as

$$E_{\rm e} = \frac{4}{3}\pi R_2^3 \times \int_1^{\gamma_2} N_{\rm e}\gamma^{-p}d\gamma + \frac{4}{3}\pi(R_1^3 - R_2^3) \times \int_1^{\gamma_1} N_{\rm e}\gamma^{-p}d\gamma, \tag{5.1}$$

$$E_{\rm B} = \frac{4}{3}\pi R_2^3 \times \frac{B_2^2}{8\pi} + \frac{4}{3}\pi(R_1^3 - R_2^3) \times \frac{B_1^2}{8\pi}. \tag{5.2}$$

5.3 Results

Table 5.4 lists the assumed and obtained values in the calculation. Table 5.5 lists the calculated total energies of electrons and magnetic field. Details of the assumption, used data, and the result for each source is described in the subsequent sections. As explained below, type 1 model could not reproduce the observed X-ray and VHE gamma-ray spectra well. This is because information on the VHE gamma-ray emission size is not available, and I could not use type 2 (or type 3) model. Thus, I did not try to improve the model for these sources, and excluded them from the discussion of the results.

5.3.1 Vela X

Vela SNR, at a distance of 0.29 kpc (Dodson et al., 2003), is composed of comlex regions containing a number of sources of non-thermal radio emission, including those designated by Rishbeth (1958) as Vela X, Vela Y, and Vela Z. PSR J0835–4510 is located in the Vela X region. The pulsar has a period of $P = 89$ ms and period derivative of $\dot{P} = 1.25 \times 10^{-13}$ s s^{-1}. The braking index is $n = 1.4$, measured by Lyne et al. (1996). The characteristic age is $\tau_{\rm c} = 11$ kyr. The VHE gamma-ray source is centered at RA=08h35m00s, Dec=–45d36m00s, and has an extension of $\sigma_{\rm TeV} = 26'$. The VHE gamma-ray spectrum is modeled by a power-law of $\Gamma_{\rm TeV} = 1.4$ and $F_{\rm TeV} = 5.5 \times 10^{-11}$ erg s^{-1} cm^{-2} (Aharonian et al., 2006c). The X-ray source has an extension of $\sigma_{\rm X} = 23'.5$ (Anada, 2009b). The X-ray spectrum is characterized by a power-law of $\Gamma_{\rm X} = 2.2$ and the unabsorbed flux 1.0×10^{-11} erg s^{-1} cm^{-2} in the 2–10 keV band (LaMassa et al., 2008). Assuming that the X-ray nebula is twice as large as the extracted region of the spectrum by LaMassa et al. (2008), the X-ray flux would be $F_{\rm X} = 2.0 \times 10^{-11}$ erg s^{-1} cm^{-2} in the whole X-ray nebula. Here, the X-ray flux is that for the power-law component, and the soft thermal emission is ignored. Using the distance $d = 0.29$ kpc, the radii of the VHE gamma-ray and the X-ray emission regions are $R_1 = 6.5$ pc and $R_2 = 6.0$ pc, respectively. The distance from the Galactic center is estimated to be $D_{\rm G} = 8.5$ kpc, thus the energy density of infrared ISRF is assumed to be $U_{\rm IR} = 0.5$ eV cm^{-3}.

Figure 5.3 shows the SED of Vela X assuming the type 2 model. Comparison with the model spectrum gives the exponential cut-off of $\gamma_1 = 1.2 \times 10^8$, $\gamma_2 = 2.5 \times 10^8$ and the normalization

Table 5.4: Summary of the assumed and obtained model parameters

#	Type*	$U_{\rm IR}$†	R_1‡	R_2§	$N_{\rm e}$‖	γ_1**	γ_2††	B_1‡‡	B_2§§
		eV cm^{-3}	pc	pc	cm^{-3}			μG	μG
1	2	0.5	6.5	6.0	2.4×10^{-6}	1.2×10^{8}	2.5×10^{9}	1.9	
2	1	0.5	0.76	0.76	6.0×10^{-3}	2.0×10^{7}		85	
3	2	1.0	25	5.4	2.2×10^{-8}	2.0×10^{7}	6.0×10^{8}	3.8	
4	2	2.0	48	23	3.8×10^{-9}	2.0×10^{7}	8.0×10^{8}	2.8	
5	2	2.0	50	11	2.8×10^{-8}	1.7×10^{7}	3.2×10^{8}	4.0	
6	1	2.0	23	23	6.0×10^{-9}	8.0×10^{7}		< 7.5	
7	2	2.0	15	5.9	1.8×10^{-6}	1.0×10^{7}	1.8×10^{8}	7.5	
8	2	1.0	14	6.5	5.0×10^{-7}	9.0×10^{6}	3.5×10^{8}	1.9	
9	2	1.0	18	7.3	2.3×10^{-7}	2.5×10^{7}	3.5×10^{8}	1.9	
10	1	2.0	4.5	4.5	6.0×10^{-6}	2.0×10^{7}		22	
11	2	2.0	26	7.2	1.1×10^{-7}	2.0×10^{7}	7.5×10^{8}	2.0	
12	3	1.0	35	1.2	4.3×10^{-9}	9.0×10^{7}	9.0×10^{7}	< 0.3	110
13	2	1.0	9.7	3.9	8.0×10^{-7}	8.0×10^{6}	6.0×10^{8}	5.7	
14	2	2.0	8.3	3.5	1.5×10^{-6}	8.0×10^{6}	2.0×10^{8}	16	
15	3	2.0	9.8	1.2	7.8×10^{-7}	2.0×10^{7}	1.2×10^{8}	< 3.0	42
16	2	2.0	7.5	2.7	6.5×10^{-7}	1.0×10^{7}	1.5×10^{8}	37	
17	2	0.5	31	7.9	5.5×10^{-7}	9.0×10^{6}	9.0×10^{7}	4.1	
18	1	0.5	18	18	1.5×10^{-8}	8.0×10^{7}		< 1.5	

* Assumed model type shown in figure 5.1.

† Assumed energy density of infra-red ISRF, which is one of the seed photons of the inverse Compton scattering.

‡ Radius of the VHE gamma-ray emission region.

§ Radius of the X-ray emission region.

‖ Number density of electrons at $\gamma = 1$.

** Cut-off energy of the electron spectrum outside of the X-ray emission region.

†† Cut-off energy of the electron spectrum in the X-ray emission region.

‡‡ Average strength of the magnetic field outside of the X-ray emission region.

§§ Average strength of the magnetic field in the X-ray emission region.

of $N_{\rm e} = 2.4 \times 10^{-6}$ cm^{-3}. Observed X-ray spectrum corresponds to $B_1 = B_2 = 1.9$ μG. The resulting total energies are $E_{\rm e} = 1.2 \times 10^{48}$ erg and $E_{\rm B} = 4.5 \times 10^{45}$ erg, respectively.

Table 5.5: Total energies of the electrons and magnetic field

#	Name	Type*	E_e† 10^{47} erg	E_B‡ 10^{47} erg	E_B/E_e	$E_B + E_e$ 10^{47} erg
1	Vela X	2	12	0.045	0.0037	12
2	Crab Nebula	1	43	0.14	0.0033	43
3	HESS J1356–645	2	5.7	10	1.8	16
4	HESS J1809–193	2	7.2	40	5.6	47
5	HESS J1825–137	2	57	90	1.6	147
6	HESS J1718–385	1	1.3	< 31	< 24	< 32
7	MSH 15–52	2	89	7.9	0.089	97
8	Kookaburra/Rabbit	2	22	0.45	0.020	22
9	Kookaburra/K3	2	21	0.89	0.042	22
10	G0.9+0.1	1	9.0	2.0	0.22	11
11	HESS J1837–069	2	33	3.3	0.099	37
12	HESS J1708–443	3	3.3	< 1.1	< 0.35	< 4.4
13	G54.1+0.3	2	12	1.4	0.12	13
14	Kes 75	2	13	6.5	0.49	20
15	HESS J1813–178	3	7.7	< 0.38	< 0.050	< 8.1
16	G21.5–0.9	2	4.4	26	6.0	30
17	HESS J1427–608	2	268	24	0.088	291
18	HESS J1702–420	1	1.6	< 0.62	< 0.38	< 2.3

* Assumed model type shown in figure 5.1.

† Total energy of electrons estimated by equation (5.1).

‡ Total energy of the magnetic field estimated by equation (5.2).

5.3.2 The Crab Nebula

The Crab nebula is one of the best-known and best-studied PWNe, and its supernova explosion was recorded in 1054. The Crab pulsar (PSR J0534+2200) is located at the center of the Crab nebula. The pulsar has a period of $P = 33$ ms and period derivative of $\dot{P} = 4.2 \times 10^{-13}$ s s^{-1}. The braking index is $n = 2.51$, measured by Lyne et al. (1993). The characteristic age is $\tau_c = 1.2$ kyr, which is almost same as the real age ($\tau \simeq 960$ yr). The VHE gamma-ray source is centered at RA=05h34m31.1s, Dec=+22d00m52s, and is not extended within the instrumental resolution. The VHE gamma-ray spectrum is modeled by a power-law of $\Gamma_{\rm TeV} = 2.39$ and $F_{\rm TeV} = 7.6 \times 10^{-11}$ erg s^{-1} cm^{-2} (Aharonian et al., 2004b). The X-ray structure of Crab nebula is clearly resolved by Chandra (Weisskopf et al., 2000b). Weisskopf et al. (2000b) showed the

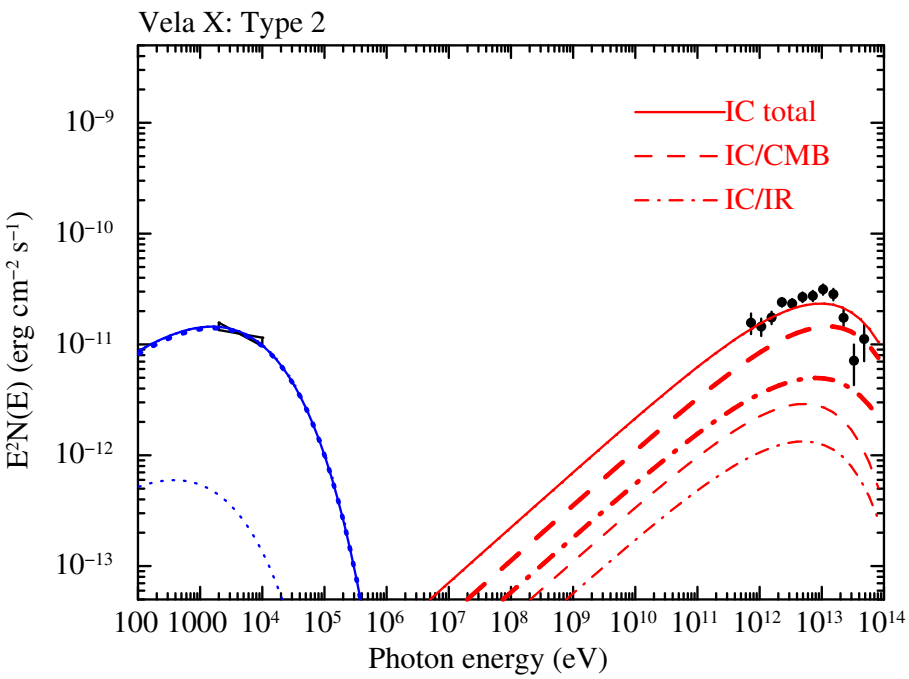

Figure 5.3: The type 2 model spectrum of Vela X overlaid on the observed spectra (Aharonian et al., 2006c; LaMassa et al., 2008). The red and blue solid lines indicate IC emission and synchrotron emission, respectively. The narrow and bold lines indicate the contribution from the electrons with the cut-off energy of γ_1 and γ_2, respectively. The dashed line and the dot-dashed line indicate the contribution from CMB and infrared ISRF, respectively. The dotted line indicates the contribution by the synchrotron radiation.

X-ray torus, jet, and the inner ring which might be the termination shock of pulsar wind. The radius of the X-ray torus is about $1'.3$ in semi-major axis, thus I assume the X-ray extent of the nebula is $3\sigma_{\rm X} = 1'.3$. The X-ray spectrum is characterized by a power-law of $\Gamma_{\rm X} = 2.1$ and the unabsorbed flux is $F_{\rm X} = 1.9 \times 10^{-8}$ erg s^{-1} cm^{-2} (Kirsch et al., 2005). Based on the distance $d = 2$ kpc, the radius of the synchrotron nebula is $R_1 = R_{\rm X} = 0.76$ pc. Because the VHE gamma-ray emission is not extended, I assume $R_1 = R_2$ and the type 1 model. The distance from the Galactic center is estimated to be $D_{\rm G} = 10.5$ kpc, thus the energy density of infrared ISRF is assumed to be $U_{\rm IR} = 0.5$ eV cm^{-3}. As reviewed in section 2.3.3, synchrotron emission also contributes as a seed photon of the inverse Compton scattering (Synchrotron Self Compton: SSC), which is quite different situation compared with other selected PWNe. However, I ignore the effect of SSC in order to analyze all the selected sources in a unified manner.

Figure 5.4 shows the SED of the Crab nebula assuming the type 1 model. Comparison with the model IC spectrum gives the exponential cut-off of $\gamma_1 = \gamma_2 = 2.0 \times 10^7$ and the normalization

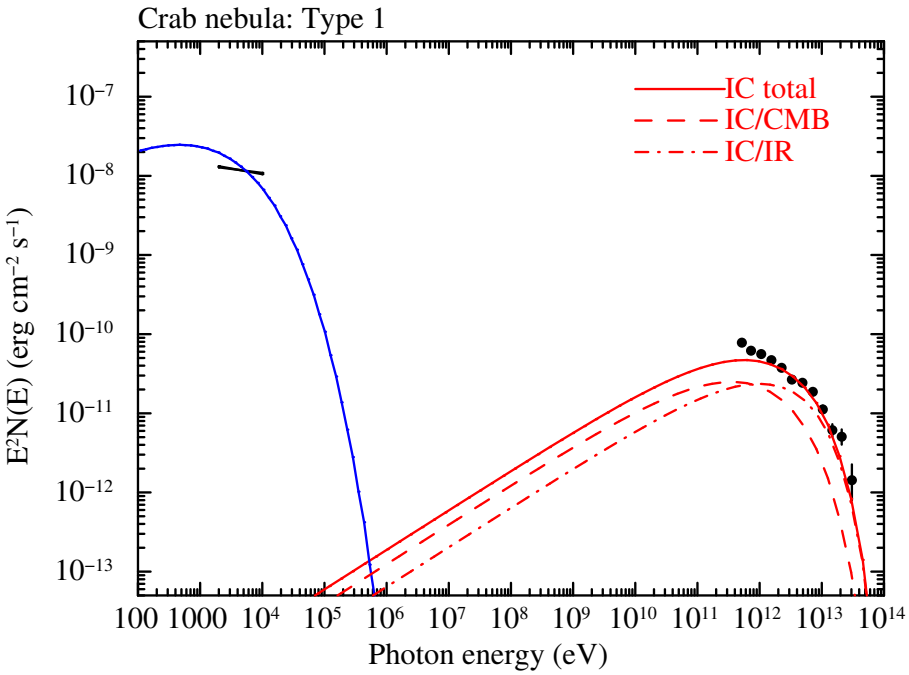

Figure 5.4: Model spectrum of the Crab nebula overlaid on the observed spectra (Aharonian et al., 2004b; Kirsch et al., 2005). The red and blue lines indicate IC emission and synchrotron emission, respectively. The dashed line and the dot-dashed line indicate the contribution from CMB and infrared ISRF, respectively.

of $N_{\rm e} = 6.0 \times 10^{-3}$ cm^{-3}. Observed X-ray spectrum corresponds to $B_1 = B_2 = 85$ μG. The resulting total energies are $E_{\rm e} = 4.3 \times 10^{48}$ erg and $E_{\rm B} = 1.4 \times 10^{46}$ erg, respectively.

5.3.3 HESS J1356–645

The VHE gamma-ray emission of HESS J1356–645 is centered at RA=13h56m00s, Dec=–64d30m00s, with an extent of $\sigma_{\rm TeV} = 12'$ (Abramowski et al., 2011b). The VHE gamma-ray spectrum is characterized by a power-law of $\Gamma_{\rm TeV} = 2.2$ and $F_{\rm TeV} = 8.0 \times 10^{-12}$ erg s^{-1} cm^{-2}. PSR J1357–6429 is located inside the VHE gamma-ray emission region. The pulse period and period derivative of the pulsar are $P = 166$ ms and $\dot{P} = 3.6 \times 10^{-13}$ s s^{-1}, respectively (Camilo et al., 2004). The distance to the pulsar is estimated to be $d = 4.1$ kpc using the dispersion measure. The diffuse X-ray emission was found by XMM-Newton. Its spectrum is characterized by a power-law of $\Gamma_{\rm X} = 1.8$ and the unabsorbed flux $F_{\rm X} = 2.1 \times 10^{-12}$ erg s^{-1} cm^{-2} (Abramowski et al., 2011b). I subtracted the filter wheel closed background from the observed raw image, and calculated a one-dimension profile. The profile was approximated by a Gaussian with $\sigma_{\rm X} = 2'.6$. Based on the distance $d = 4.1$ kpc, the radii of the VHE gamma-ray and X-ray emission regions are $R_{\rm TeV} = 25$ pc and $R_{\rm X} = 5.5$ pc, respectively. The distance from the

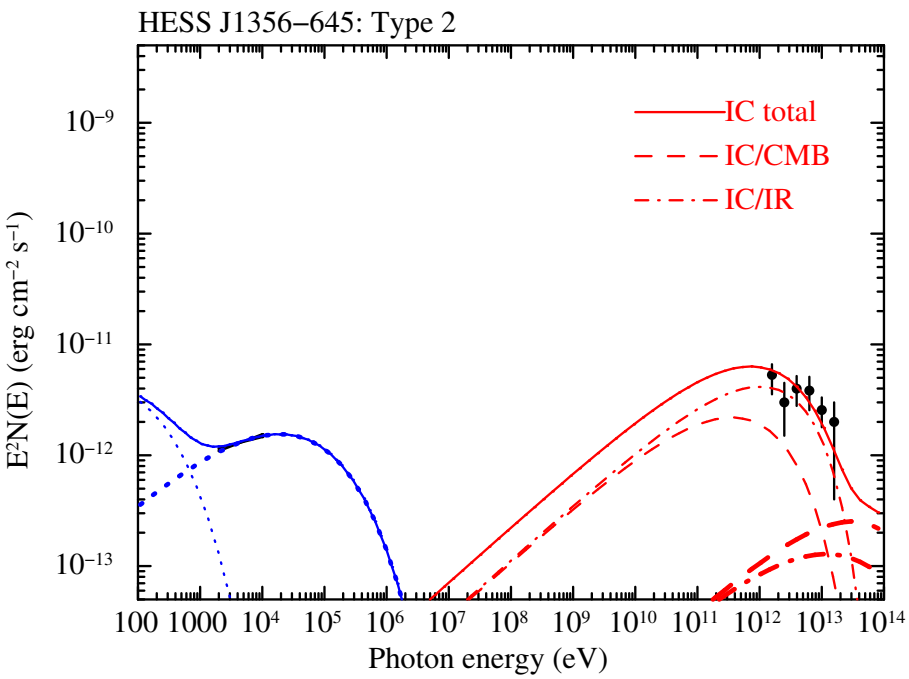

Figure 5.5: The type 2 model spectrum of HESS J1356–645 overlaid on the observed spectra (Abramowski et al., 2011b). The red and blue solid lines indicate IC emission and synchrotron emission, respectively. The narrow and bold lines indicate the contribution from the electrons with the cut-off energy of γ_1 and γ_2, respectively. The dashed line and the dot-dashed line indicate the contribution from CMB and infrared ISRF, respectively. The dotted line indicates the contribution by the synchrotron radiation.

Galactic center is estimated to be $D_{\rm G} = 6.7$ kpc, thus the energy density of infrared ISRF is assumed to be $U_{\rm IR} = 1.0$ eV cm^{-3}.

Figure 5.5 shows the SED of HESS J1356–645 assuming the type 2 model. Comparison with the model IC spectrum gives the exponential cut-off of $\gamma_1 = 2.0 \times 10^7$, $\gamma_2 = 6.0 \times 10^8$ and the normalization of $N_{\rm e} = 2.2 \times 10^{-8}$ cm^{-3}. Observed X-ray spectrum corresponds to $B_1 = B_2 = 3.8$ μG. The resulting total energies are $E_{\rm e} = 5.7 \times 10^{47}$ erg and $E_{\rm B} = 1.0 \times 10^{48}$ erg, respectively.

5.3.4 HESS J1809–193

The VHE gamma-ray emission of HESS J1809–193 is centered at RA=18h09m52s, Dec=–19d23m42s, with an extent of $\sigma_{\rm TeV} = 15'$ (Aharonian et al., 2007). The VHE gamma-ray spectrum is characterized by a power-law of $\Gamma_{\rm TeV} = 2.2$ and $F_{\rm TeV} = 1.8 \times 10^{-11}$ erg s^{-1} cm^{-2}. PSR J1809–1917 is located within the extent of the VHE gamma-ray emission. The pulse period and period derivative of the pulsar are $P = 83$ ms and $\dot{P} = 2.6 \times 10^{-14}$ s s^{-1}, respectively

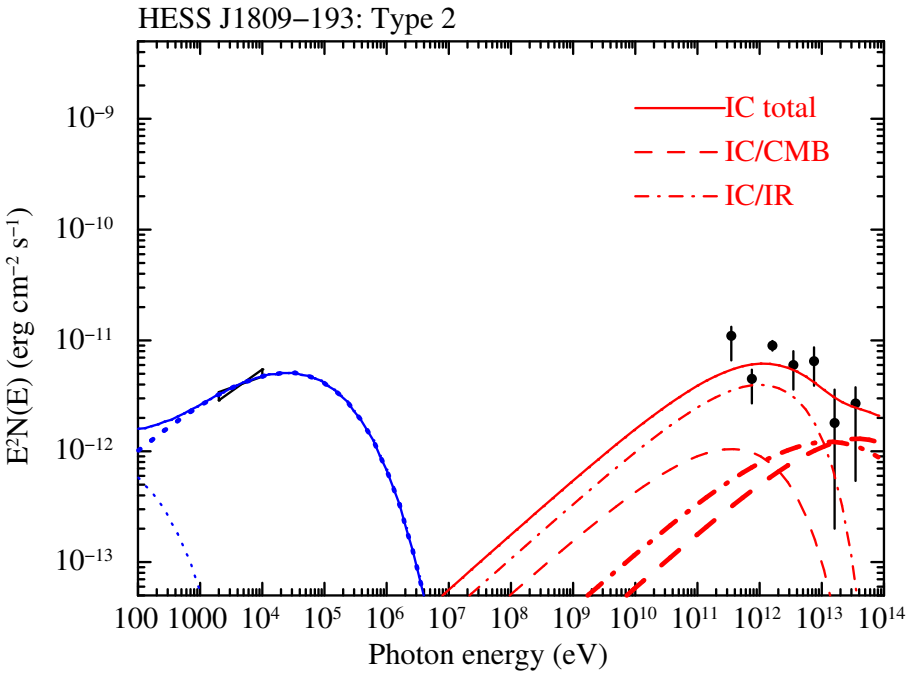

Figure 5.6: The type 2 model spectrum of HESS J1809–193 overlaid on the VHE gamma-ray spectrum (Aharonian et al., 2007) and the X-ray spectrum (Anada, 2009b). The red and blue solid lines indicate IC emission and synchrotron emission, respectively. The narrow and bold lines indicate the contribution from the electrons with the cut-off energy of γ_1 and γ_2, respectively. The dashed line and the dot-dashed line indicate the contribution from CMB and infrared ISRF, respectively. The dotted line indicates the contribution by the synchrotron radiation.

(Manchester et al., 2005). The distance to the pulsar is estimated to be $d = 3.7$ kpc using the dispersion measure. The diffuse X-ray emission was observed by Suzaku. Its spectrum is characterized by a power-law of $\Gamma_{\rm X} = 1.7$ and the unabsorbed flux $F_{\rm X} = 5.9\times10^{-12}$ erg s^{-1} cm^{-2} (Anada, 2009b). The profile was approximated by a Gaussian with $\sigma_{\rm X} = 6'.8$ (Bamba et al., 2010). Based on the distance $d = 3.7$ kpc, the radii of the VHE gamma-ray and X-ray emission regions are $R_{\rm TeV} = 48$ pc and $R_{\rm X} = 23$ pc, respectively. The distance from the Galactic center is estimated to be $D_{\rm G} = 4.9$ kpc, thus the energy density of infrared ISRF is assumed to be $U_{\rm IR} = 1.0$ eV cm^{-3}.

Figure 5.6 shows the SED of HESS J1809–193 assuming the type 2 model. Comparison with the model IC spectrum gives the exponential cut-off of $\gamma_1 = 2.0 \times 10^7$, $\gamma_2 = 8.0 \times 10^8$ and the normalization of $N_{\rm e} = 3.8 \times 10^{-9}$ cm^{-3}. Observed X-ray spectrum corresponds to $B_1 = B_2 = 2.8$ μG. The resulting total energies are $E_{\rm e} = 7.2\times10^{47}$ erg and $E_{\rm B} = 4.0\times10^{48}$ erg, respectively.

5.3.5 HESS J1825–137

The VHE gamma-ray emission of HESS J1825–137 is centered at RA=18h25m41s, Dec=–13d50m20s, and is extended ranging from 13′.8 to 15′.6 (Aharonian et al., 2006d). In the present analysis, the VHE gamma-ray emission region is assumed to be a sphere with a radius of $\sigma_{\rm TeV} = 14'.7$. The VHE gamma-ray spectrum is characterized by a power-law of $\Gamma_{\rm TeV} = 2.4$ and $F_{\rm TeV} = 4.9 \times 10^{-11}$ erg s^{-1} cm^{-2}. PSR J1826–1334 is located within the VHE gamma-ray emission region. The pulse period and period derivative of the pulsar are $P = 102$ ms and $\dot{P} = 7.5 \times 10^{-14}$ s s^{-1}, respectively (Manchester et al., 2005). The distance to the pulsar is estimated to be $d = 4.1$ kpc using the dispersion measure. The spectrum of the diffuse X-ray emission was measured with Suzaku and is characterized by a power-law of $\Gamma_{\rm X} = 2.0$ and the unabsorbed flux $F_{\rm X} = 5.0 \times 10^{-12}$ erg s^{-1} cm^{-2} (Uchiyama et al., 2009b). The profile was approximated by a Gaussian with $\sigma_{\rm X} = 3'.2$ (Bamba et al., 2010). Based on the distance $d = 4.1$ kpc, the radii of the VHE gamma-ray and X-ray emission regions are $R_{\rm TeV} = 50$ pc and $R_{\rm X} = 11$ pc, respectively. The distance from the Galactic center is estimated to be $D_{\rm G} = 4.7$ kpc, thus the energy density of infrared ISRF is assumed to be $U_{\rm IR} = 2.0$ eV cm^{-3}.

Figure 5.7 shows the SED of HESS J1825–137 assuming the type 2 model. Comparison with the modelf IC spectrum gives the exponential cut-off of $\gamma_1 = 1.7 \times 10^7$, $\gamma_2 = 3.2 \times 10^8$ and the normalization of $N_{\rm e} = 2.8 \times 10^{-8}$ cm^{-3}. Observed X-ray spectrum corresponds to $B_1 = B_2 = 4.0$ μG. The resulting total energies are $E_{\rm e} = 5.7 \times 10^{48}$ erg and $E_{\rm B} = 9.0 \times 10^{48}$ erg, respectively.

5.3.6 HESS J1718–385

The VHE gamma-ray emission of HESS J1718–385 is centered at RA=17h18m07s, Dec=–38d33m00s, and is extended ranging from 4′.2 to 9′.0 (Aharonian et al., 2007). In the present analysis, the VHE gamma-ray emission region is assumed to be a sphere with a radius of $\sigma_{\rm TeV} = 6'.1$. The VHE gamma-ray spectrum is characterized by a power-law of $\Gamma_{\rm TeV} = 0.7$ and $F_{\rm TeV} = 2.9 \times 10^{-12}$ erg s^{-1} cm^{-2}. PSR J1718–3825 is located inside the VHE gamma-ray emission. The pulse period and period derivative of the pulsar are $P = 75$ ms and $\dot{P} = 1.3 \times 10^{-14}$ s s^{-1}, respectively (Manchester et al., 2005). The distance to the pulsar is estimated to be $d = 4.2$ kpc using the dispersion measure. Hinton et al. (2007b) derived an upper limit of diffuse X-ray flux, which is $F_{\rm X} < 1.0 \times 10^{-13}$ erg s^{-1} cm^{-2} for the assumed index of $\Gamma_{\rm X} = 1.9$. Based on the distance $d = 4.2$ kpc, the radius of the VHE gamma-ray emission is $R_{\rm TeV} = 23$ pc. Because the size of the X-ray emission region is unavailable in the literature, I assumed to be $R_2 = R_1 = R_{\rm TeV}$. The distance from the Galactic center is estimated to be $D_{\rm G} = 4.4$ kpc, thus the energy density of infrared ISRF is assumed to be $U_{\rm IR} = 2.0$ eV cm^{-3}.

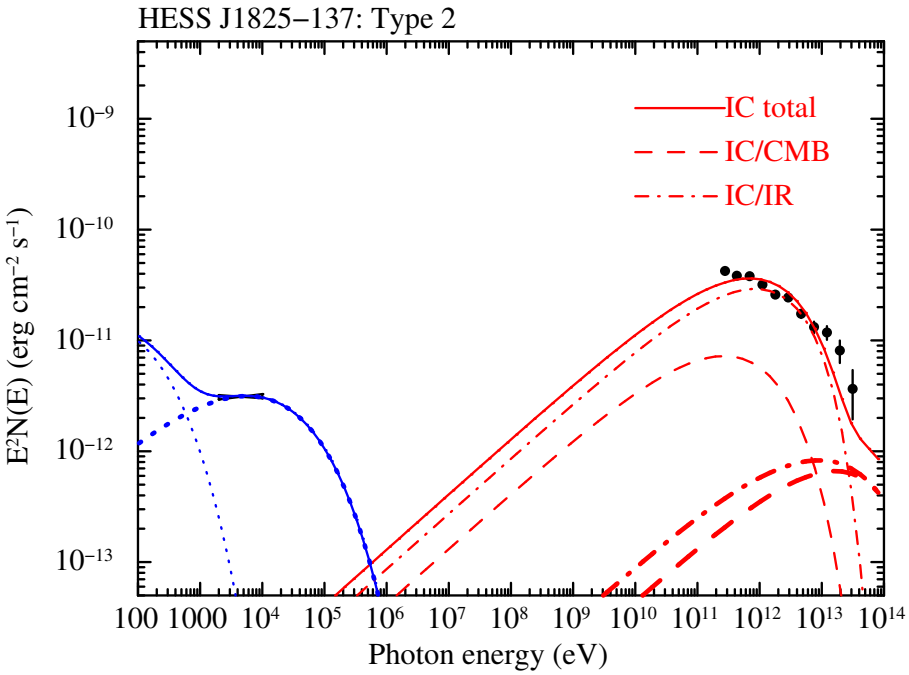

Figure 5.7: The type 2 model spectrum of HESS J1825–137 overlaid on the VHE gamma-ray spectrum (Aharonian et al., 2006d) and the X-ray spectrum (Uchiyama et al., 2009b). The red and blue solid lines indicate IC emission and synchrotron emission, respectively. The narrow and bold lines indicate the contribution from the electrons with the cut-off energy of γ_1 and γ_2, respectively. The dashed line and the dot-dashed line indicate the contribution from CMB and infrared ISRF, respectively. The dotted line indicates the contribution by the synchrotron radiation.

Figure 5.8 shows the SED of HESS J1718–385 assuming the type 1 model. Comparison with the model IC spectrum gives the exponential cut-off of $\gamma_1 = \gamma_2 = 8.0 \times 10^7$ and the normalization of $N_e = 6.0 \times 10^{-7}$ cm^{-3}. The upper limit of the observed X-ray flux corresponds to $B_2 (= B_1) < 7.5$ μG. The resulting total energies are $E_e = 1.3 \times 10^{47}$ erg and $E_B < 3.1 \times 10^{48}$ erg, respectively.

5.3.7 MSH 15–52

The VHE gamma-ray emission of MSH 15–52 is centered at RA=15h14m07s, Dec=–59d09m27s, and is extended ranging from 2′.4 to 6′.6 (Aharonian et al., 2005b). In the present analysis, the VHE gamma-ray emission region is assumed to be a sphere with a radius of $\sigma_{\rm TeV} = 4'.0$. The VHE gamma-ray spectrum is characterized by a power-law of $\Gamma_{\rm TeV} = 2.3$ and $F_{\rm TeV} = 1.8 \times 10^{-11}$ erg s^{-1} cm^{-2}. PSR J1513–5908 is located inside the VHE gamma-ray emission. The pulse period and period derivative of the pulsar are $P = 151$ ms and $\dot{P} = 1.5 \times 10^{-12}$ s s^{-1},

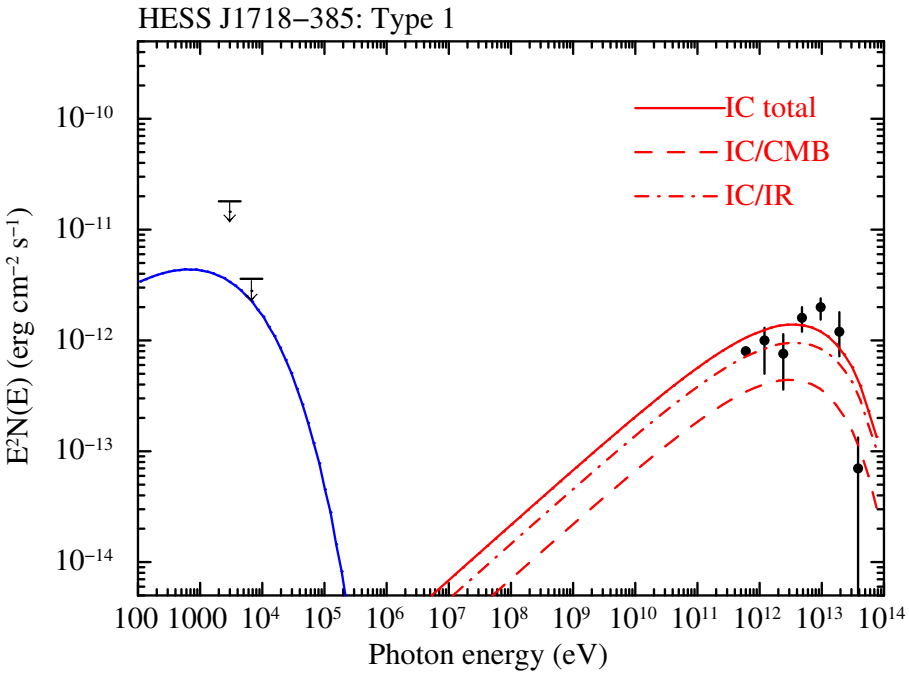

Figure 5.8: The type 1 model spectrum of HESS J1718–385 overlaid on the VHE gamma-ray spectrum (Aharonian et al., 2007) and the X-ray spectrum (Hinton et al., 2007b). The red and blue lines indicate IC emission and synchrotron emission, respectively. The dashed line and the dot-dashed line indicate the contribution from CMB and infrared ISRF, respectively.

respectively (Manchester et al., 2005). The distance to the pulsar is estimated to be $d = 5.8$ kpc using the dispersion measure. The spectrum of diffuse X-ray emission is characterized by a power-law of $\Gamma_{\rm X} = 2.1$ and the unabsorbed flux $F_{\rm X} = 3.7 \times 10^{-11}$ erg s^{-1} cm^{-2} (Gaensler et al., 2002). The profile was approximated by a Gaussian with $\sigma_{\rm X} = 1'.6$ (Bamba et al., 2010). Based on the distance $d = 5.8$ kpc, the radii of the VHE gamma-ray emission and the X-ray emission are $R_{\rm TeV} = 15$ pc and $R_{\rm X} = 5.9$ pc, respectively. The distance from the Galactic center is estimated to be $D_{\rm G} = 5.5$ kpc, thus the energy density of infrared ISRF is assumed to be $U_{\rm IR} = 1.0$ eV cm^{-3}.

Figure 5.9 shows the SED of MSH 15–52 assuming the type 2 model. Comparison with the model IC spectrum gives the exponential cut-off of $\gamma_1 = 1.0 \times 10^7$, $\gamma_2 = 1.8 \times 10^8$ and the normalization of $N_{\rm e} = 1.8 \times 10^{-6}$ cm^{-3}. Observed X-ray spectrum corresponds to $B_1 = B_2 = 7.5$ μG. The resulting total energies are $E_{\rm e} = 8.9 \times 10^{48}$ erg and $E_{\rm B} = 7.9 \times 10^{47}$ erg, respectively.

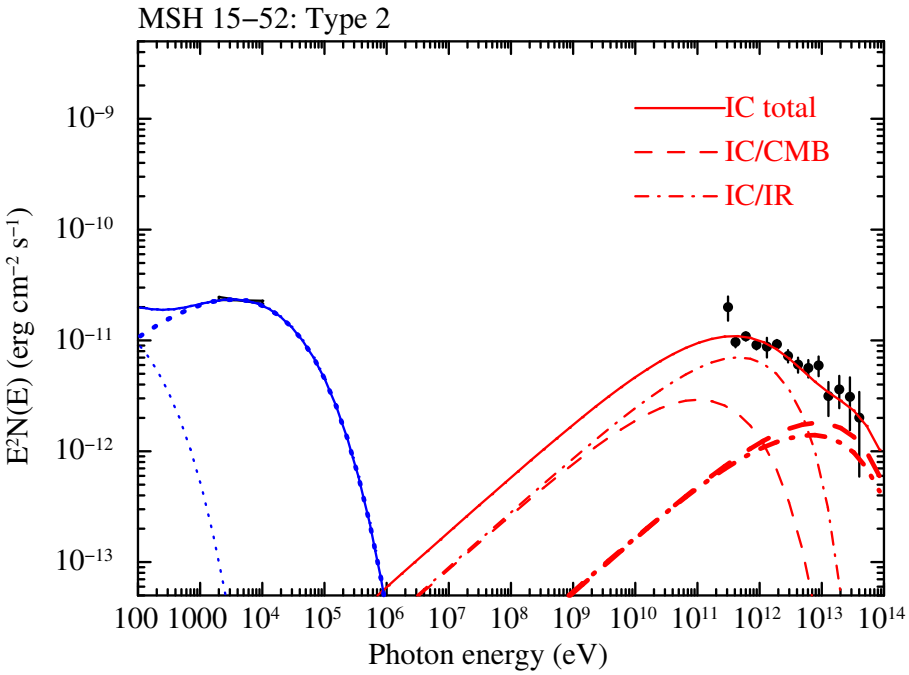

Figure 5.9: The type 2 model spectrum of MSH 15–52 overlaid on the VHE gamma-ray spectrum (Aharonian et al., 2005b) and the X-ray spectrum (Gaensler et al., 2002). The red and blue solid lines indicate IC emission and synchrotron emission, respectively. The narrow and bold lines indicate the contribution from the electrons with the cut-off energy of γ_1 and γ_2, respectively. The dashed line and the dot-dashed line indicate the contribution from CMB and infrared ISRF, respectively. The dotted line indicates the contribution by the synchrotron radiation.

5.3.8 Kookaburra/Rabbit

The VHE gamma-ray emission of Rabbit (HESS J1418–609) is centered at RA=14h18m07s, Dec=–60d58m31s, and is extended ranging from $3'.0$ to $3'.6$ (Aharonian et al., 2006e). In the present analysis, the VHE gamma-ray emission region is assumed to be a sphere with a radius of $\sigma_{\rm TeV} = 3'.3$. The VHE gamma-ray spectrum is characterized by a power-law of $\Gamma_{\rm TeV} = 2.2$ and $F_{\rm TeV} = 7.7 \times 10^{-12}$ erg s^{-1} cm^{-2}. PSR J1418–6058 is found by Fermi Ray et al. (2011). The pulse period and period derivative of the pulsar are $P = 111$ ms and $\dot{P} = 1.7 \times 10^{-13}$ s s^{-1}, respectively. The distance to the pulsar is assumed to be $d = 5.0$ kpc. The spectrum of diffuse X-ray emission is characterized by a power-law of $\Gamma_{\rm X} = 1.8$ and the unabsorbed flux $F_{\rm X} = 2.6 \times 10^{-12}$ erg s^{-1} cm^{-2} (Kishishita et al., 2012). The profile was approximated by a Gaussian with $\sigma_{\rm X} = 1'.5$ (Anada et al., 2009a). Based on the assumed distance $d = 5.0$ kpc, the radii of the VHE gamma-ray and the X-ray emission regions are $R_{\rm TeV} = 14$ pc and $R_{\rm X} = 6.5$ pc, respectively. The distance from the Galactic center is estimated to $D_{\rm G} = 6.3$ kpc, thus the

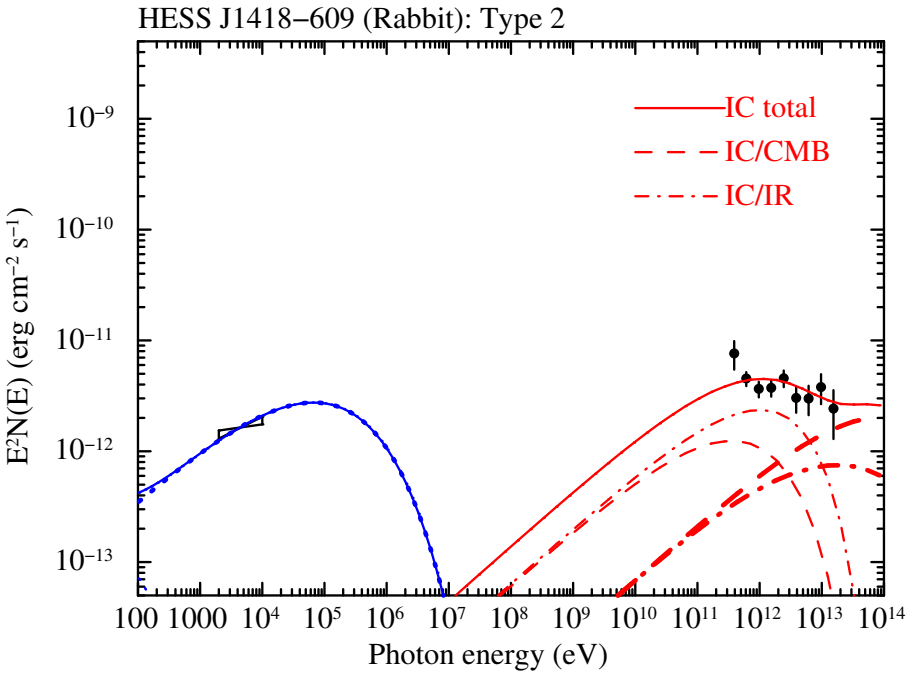

Figure 5.10: The type 2 model spectrum of Rabbit overlaid on the VHE gamma-ray spectrum (Aharonian et al., 2006e) and the X-ray spectrum (Kishishita et al., 2012). The red and blue solid lines indicate IC emission and synchrotron emission, respectively. The narrow and bold lines indicate the contribution from the electrons with the cut-off energy of γ_1 and γ_2, respectively. The dashed line and the dot-dashed line indicate the contribution from CMB and infrared ISRF, respectively. The dotted line indicates the contribution by the synchrotron radiation.

energy density of infrared ISRF is assumed to be $U_{\rm IR} = 1.0$ eV cm^{-3}.

Figure 5.10 shows the SED of Rabbit assuming the type 2 model. Comparison with the model IC spectrum gives the exponential cut-off of $\gamma_1 = 9.0 \times 10^6$, $\gamma_2 = 3.5 \times 10^8$ and the normalization of $N_{\rm e} = 5.0 \times 10^{-7}$ cm^{-3}. Observed X-ray spectrum corresponds to $B_1 = B_2 = 1.9\ \mu$G. The resulting total energies are $E_{\rm e} = 2.2 \times 10^{48}$ erg and $E_{\rm B} = 4.5 \times 10^{46}$ erg, respectively. Kishishita et al. (2012) evaluated the X-ray and VHE gamma-ray spectra using a simple one-zone model. They obtained $B \simeq 2.5\ \mu$G and $\gamma_{\rm max} \simeq 2 \times 10^8$, which are almost same as my results.

5.3.9 Kookaburra/K3

The VHE gamma-ray emission of K3 (HESS J1420–607) is centered at RA=14h20m09s, Dec=–60d45m36s, with an extent of $\sigma_{\rm TeV} = 3'.6$ (Aharonian et al., 2006e). The VHE gamma-ray spectrum is characterized by a power-law of $\Gamma_{\rm TeV} = 2.2$ and $F_{\rm TeV} = 1.1 \times 10^{-11}$ erg s^{-1} cm^{-2}.

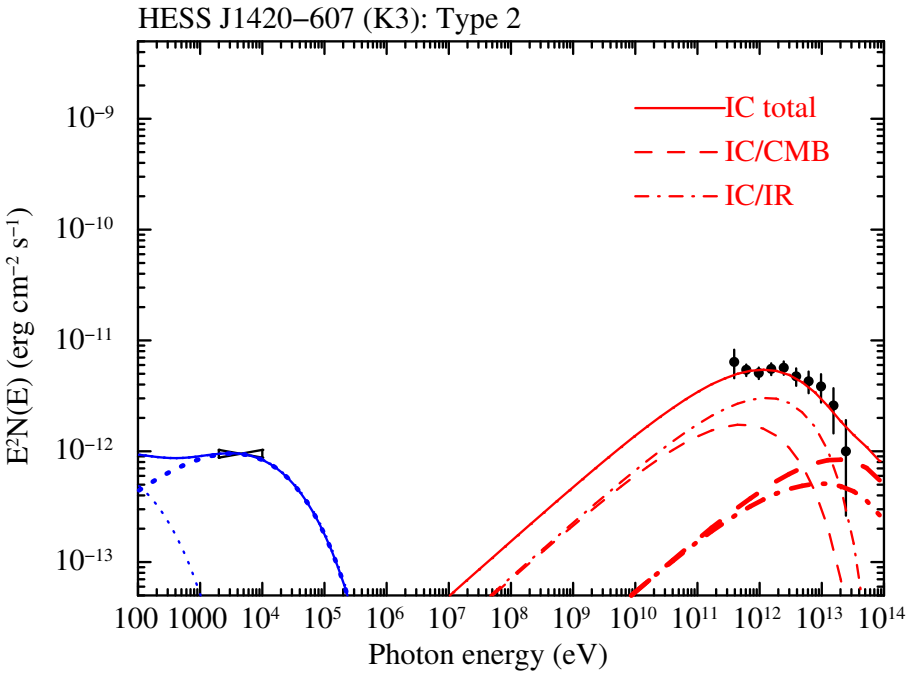

Figure 5.11: The type 2 model spectrum of Rabbit overlaid on the VHE gamma-ray spectrum (Aharonian et al., 2006e) and the X-ray spectrum (Kishishita et al., 2012). The red and blue solid lines indicate IC emission and synchrotron emission, respectively. The narrow and bold lines indicate the contribution from the electrons with the cut-off energy of γ_1 and γ_2, respectively. The dashed line and the dot-dashed line indicate the contribution from CMB and infrared ISRF, respectively. The dotted line indicates the contribution by the synchrotron radiation.

PSR J1420–6048 is located inside the VHE gamma-ray emission. The pulse period and period derivative of the pulsar are $P = 68$ ms and $\dot{P} = 8.3 \times 10^{-14}$ s s^{-1}, respectively (Manchester et al., 2005). The distance to the pulsar is estimated to be $d = 7.7$ kpc using the dispersion measure. The spectrum of diffuse X-ray emission is characterized by a power-law of $\Gamma_{\rm X} = 2.0$ and the unabsorbed flux $F_{\rm X} = 1.5 \times 10^{-12}$ erg s^{-1} cm^{-2} (Kishishita et al., 2012). The profile is approximated by a Gaussian with $\sigma_{\rm X} = 1'.5$ (Bamba et al., 2010). Based on the distance $d = 7.7$ kpc, the radii of the VHE gamma-ray and the X-ray emission regions are $R_{\rm TeV} = 18$ pc and $R_{\rm X} = 7.3$ pc, respectively. The distance from the Galactic center is estimated to be $D_{\rm G} = 6.4$ kpc, thus the energy density of infrared ISRF is assumed to be $U_{\rm IR} = 1.0$ eV cm^{-3}.

Figure 5.11 shows the SED of Kookaburra/K3 assuming the type 2 model. Comparison with the model IC spectrum gives the exponential cut-off of $\gamma_1 = 2.5 \times 10^7$, $\gamma_2 = 3.5 \times 10^8$ and the normalization of $N_{\rm e} = 2.3 \times 10^{-7}$ cm^{-3}. Observed X-ray spectrum corresponds to $B_1 = B_2 = 1.9$ μG. The resulting total energies are $E_{\rm e} = 2.1 \times 10^{48}$ erg and $E_{\rm B} = 8.9 \times 10^{46}$ erg, respectively. Kishishita et al. (2012) evaluated the X-ray and VHE gamma-ray spectra using

a simple one-zone model. They obtained $B \simeq 3$ μG and $\gamma_{\rm max} \simeq 8 \times 10^7$. Comparing with their results, the magnetic field strength is lower than their value because they adopted higher cut-off energy contributing VHE gamma-ray emission, and the X-ray spectrum is reproduced only by adjusting the magnetic field strength.

5.3.10 G0.9+0.1

The VHE gamma-ray emission of G0.9+0.1 is centered at RA=17h47m23.2s, Dec=–28d09m06s, and is not extended (Aharonian et al., 2005c). The VHE gamma-ray spectrum is characterized by a power-law of $\Gamma_{\rm TeV} = 2.4$ and $F_{\rm TeV} = 2.0 \times 10^{-12}$ erg s^{-1} cm^{-2}. PSR J1747–2809 is located inside the VHE gamma-ray emission. The pulse period and period derivative of the pulsar are $P = 52$ ms and $\dot{P} = 1.6 \times 10^{-13}$ s s^{-1}, respectively (Camilo et al., 2009). They suggest that the most probable distance is 10 kpc. G0.9+0.1 was observed with XMM-Newton. The spectrum of diffuse X-ray emission is characterized by a power-law of $\Gamma_{\rm X} = 2.0$ and the unabsorbed flux $F_{\rm X} = 5.8 \times 10^{-12}$ erg s^{-1} cm^{-2} (Porquet et al., 2003). They extracted the spectrum of PWN from an ellipsoidal region ($r \simeq 2'.0$), which covers all the diffuse X-ray emission around the pulsar. Thus, I assume the X-ray extent is $3\sigma_{\rm X} = 2'.0$. Based on the assumed distance $d = 10$ kpc, the radus of the X-ray emission is $R_{\rm X} = 4.5$ pc. Since the VHE gamma-ray emission is note extended, I assume $R_1 = R_2 = R_{\rm X}$. The distance from the Galactic center is estimated to be $D_{\rm G} = 1.5$ kpc, thus the energy density of infrared ISRF is assumed to be $U_{\rm IR} = 2.0$ eV cm^{-3}.

Figure 5.12 shows the SED of G0.9+0.1 assuming the type 1 model. The fit is admittedly poor due to the use of type 1 model. Comparison with the model spectrum gives the exponential cut-off of $\gamma_{\rm cut} = 2.0 \times 10^7$ and the normalization of $N_{\rm e} = 6.0 \times 10^{-6}$ cm^{-3}. Observed X-ray spectrum corresponds to $B_1 = B_2 = 22$ μG. The resulting total energies are $E_{\rm e} = 9.0 \times 10^{47}$ erg and $E_{\rm B} = 2.0 \times 10^{47}$ erg, respectively.

5.3.11 HESS J1837–069

The VHE gamma-ray emission of HESS J1837–069 is centered at RA=18h37m38.4s, Dec=–06d57m00s, and is extended ranging from $3'.0$ to $7'.0$ (Aharonian et al., 2006a). In this analysis, the VHE gamma-ray emission field is assumed to be a sphere with a radius of $\sigma_{\rm TeV} = 4'.6$. The VHE gamma-ray spectrum is characterized by a power-law of $\Gamma_{\rm TeV} = 2.3$ and $F_{\rm TeV} = 1.4 \times 10^{-11}$ erg s^{-1} cm^{-2}. A pulsation was detected from AX J1838.0–0655 in the vicinity of HESS J1837–069 (Anada et al., 2009a). The pulse period and period derivative of the pulsar are $P = 70$ ms and $\dot{P} = 4.9 \times 10^{-14}$ s s^{-1}, respectively. Anada et al. (2009a) assumed the distance $d = 6.6$ kpc using the radial velocity of the nearby cluster of red supergiants by

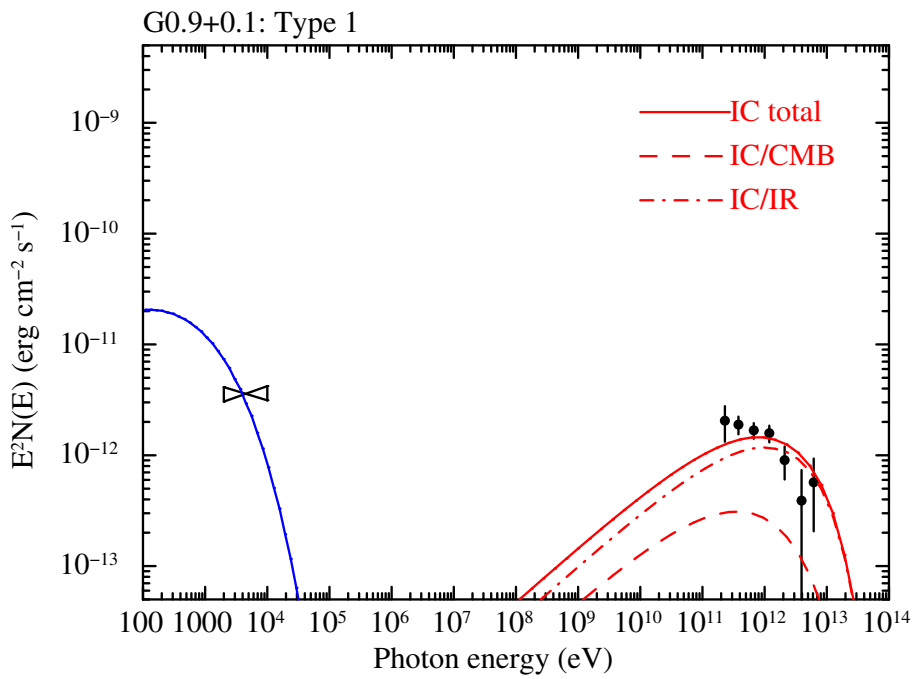

Figure 5.12: The type 1 model spectrum of G0.9+0.1 overlaid on the VHE gamma-ray spectrum (Aharonian et al., 2005c) and the X-ray spectrum (Porquet et al., 2003). The red and blue lines indicate IC emission and synchrotron emission, respectively. The dashed line and the dot-dashed line indicate the contribution from CMB and infrared ISRF, respectively.

Davies et al. (2008). The spectrum of diffuse X-ray emission is characterized by a power-law of $\Gamma_{\rm X} = 1.6$ and the unabsorbed flux $F_{\rm X} = 1.0 \times 10^{-12}$ erg s^{-1} cm^{-2} (Gotthelf and Halpern, 2008). The profile was approximated by a Gaussian with $\sigma_{\rm X} = 1'.3$ (Bamba et al., 2010). Based on the assumed distance $d = 6.6$ kpc, the radii of the VHE gamma-ray emission and the X-ray emission are $R_{\rm TeV} = 26$ pc and $R_{\rm X} = 7.2$ pc, respectively. The distance from the Galactic center is estimated to be $D_{\rm G} = 3.8$ kpc, thus the energy density of infrared ISRF is assumed to be $U_{\rm IR} = 2.0$ eV cm^{-3}.

Figure 5.13 shows the SED of HESS J1837–069 assuming the type 2 model. Comparison with the model IC spectrum gives the exponential cut-off of $\gamma_1 = 2.0 \times 10^7$, $\gamma_2 = 7.5 \times 10^8$ and the normalization of $N_{\rm e} = 1.1 \times 10^{-7}$ cm^{-3}. Observed X-ray spectrum corresponds to $B_1 = B_2 = 2.0$ μG. The resulting total energies are $E_{\rm e} = 3.3 \times 10^{48}$ erg and $E_{\rm B} = 3.3 \times 10^{47}$ erg, respectively.

5.3.12 HESS J1708–443

HESS J1708–443 is located in the SNR G343.1–2.3. The radio image of the SNR shows incomplete shell structure of a typical size of $30' - 60'$ (Dodson & Golap, 2002). The VHE gamma-

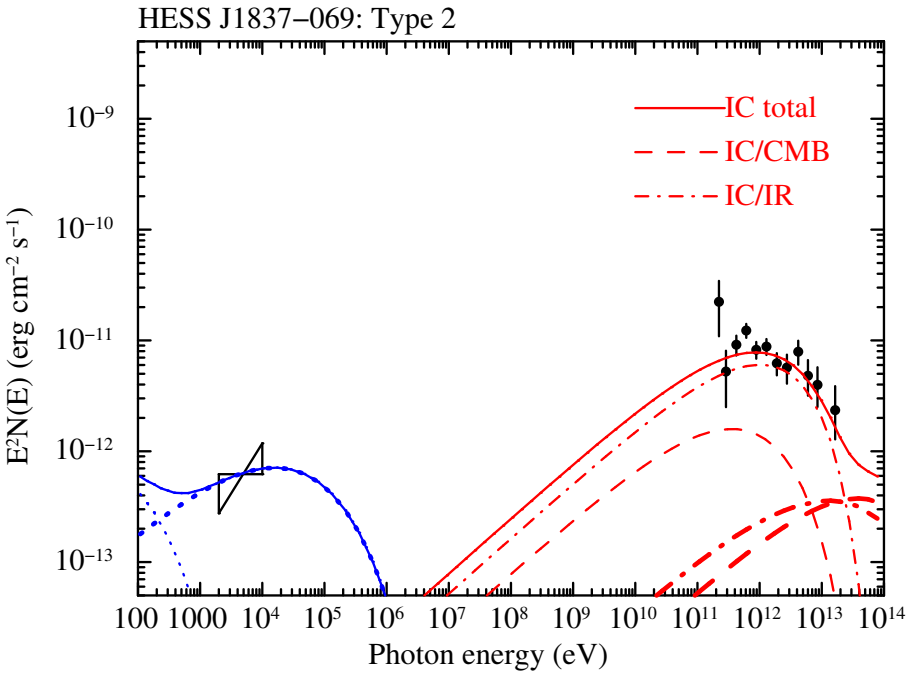

Figure 5.13: The type 2 model spectrum of HESS J1837–069 overlaid on the VHE gamma-ray spectrum (Aharonian et al., 2006a) and the X-ray spectrum (Gotthelf and Halpern, 2008). The red and blue solid lines indicate IC emission and synchrotron emission, respectively. The narrow and bold lines indicate the contribution from the electrons with the cut-off energy of γ_1 and γ_2, respectively. The dashed line and the dot-dashed line indicate the contribution from CMB and infrared ISRF, respectively. The dotted line indicates the contribution by the synchrotron radiation.

ray emission is centered at RA=17h08m11s, Dec=–44d20m00s, with an extent of $\sigma_{\rm TeV} = 17'.4$ (Abramowski et al., 2011c). Thus, the VHE gamma-ray emission region is partially overlapped with the incomplete shell detected in radio, and this source is classified as "composite" in table 5.1. When we compare the radio and VHE gamma-ray morphology, they are largely different. It is considered that the shell does not have major contribution to the VHE gamma-ray emission, but the possibility cannot be excluded. The spectrum of the VHE gamma-ray emission is characterized by a power-law of $\Gamma = 2.0$ and $F_{\rm TeV} = 1.7 \times 10^{-11}$ erg s^{-1} cm^{-2}. PSR J1709–4429 (or PSR B1706–44) is located at the edge of the VHE gamma-ray emission region. The pulse period and period derivative of the pulsar are $P = 102$ ms and $\dot{P} = 9.3 \times 10^{-14}$ s s^{-1}, respectively (Johnston et al., 1992). The distance to the pulsar is estimated to be $d = 2.3$ kpc using the dispersion measure. X-ray observation was performed with Chandra (Romani et al., 2005). The spectrum of diffuse X-ray emission is characterized by a power-law of $\Gamma_{\rm X} = 1.77$ and the unabsorbed flux $F_{\rm X} = 3.9 \times 10^{-13}$ erg s^{-1} cm^{-2}. The X-ray nebula is extended with a radius of $r = 110''$ (Romani et al., 2005). Thus, I assume $3\sigma_{\rm X} = 1'.8$. Based on the assumed

distance $d = 2.3$ kpc, the radii of the VHE gamma-ray emission and the X-ray emission are $R_{\rm TeV} = 35$ pc and $R_{\rm X} = 1.2$ pc, respectively. The distance from the Galactic center is estimated to $D_{\rm G} = 6.8$ kpc, thus the energy density of infrared ISRF is assumed to be $U_{\rm IR} = 1.0$ eV cm^{-3}.

Figure 5.14 shows the SED of HESS J1708–443 assuming the type 3 model (upper panel) and the type 2 model (lower model). If we assume the type 2 model, X-rays are emitted significantly from the outer zone. Thus, I use the type 3 model for this source. Comparison with the model spectrum gives the exponential cut-off of $\gamma_1 = \gamma_2 = 9.0 \times 10^7$ and the normalization of $N_{\rm e} = 4.3 \times 10^{-9}$ cm^{-3}. Observed X-ray spectrum corresponds to $B_2 = 110$ μG, which is almost same as the estimated value by Romani et al. (2005). The upper limit of the magnetic field strength outside the X-ray emission region is $B_1 < 0.3$ μG. Such a weak magnetic field suggests that a significant fraction of VHE gamma-ray emission includes the contribution of the protons accelerated at the SNR's shock. The resulting total energies are $E_{\rm e} = 3.3 \times 10^{47}$ erg and $E_{\rm B} < 1.1 \times 10^{47}$ erg, respectively.

5.3.13 G54.1+0.3

The VHE gamma-ray emission of a composite SNR G54.1+0.3 was found by VERITAS, which is centered at RA=19h30m32s, Dec=+18d52m17s, and is extended to $\sigma_{\rm TeV} = 1'.8$(Acciari et al., 2010). The SNR has a center-filled morphology in radio with a typical size of $1'.5$. Because this is comparable or smaller than VHE gamma-ray size, it is classified "composite" in table 5.1. (Velusamy & Becker, 1988) considered the SNR is a Crab-like, since It has a flat radio spectrum and strong polarization. Thus, major contribution to the VHE gamma-rays from the shell of SNR is unlikely. The spectrum of the VHE gamma-ray emission is characterized by a power-law of $\Gamma = 2.4$ and $F_{\rm TeV} = 1.8 \times 10^{-12}$ erg s^{-1} cm^{-2}. PSR J1930–1852 is located at the center of the VHE gamma-ray extent (Camilo et al., 2002). The pulse period and period derivative of the pulsar are $P = 136$ ms and $\dot{P} = 7.5 \times 10^{-13}$ s s^{-1}, respectively. The distance to the pulsar is estimated to be $d = 5.0$ kpc using the dispersion measure. The spectrum of diffuse X-ray emission is characterized by a power-law of $\Gamma_{\rm X} = 1.8$ and the unabsorbed flux $F_{\rm X} = 7.5 \times 10^{-12}$ erg s^{-1} cm^{-2} (Bocchino et al., 2010). They analyzed the PWN spectrum in the core region, which is within the radius of $r = 160''$. Thus, I assume $3\sigma_{\rm X} = 2'.7$. Based on the distance $d = 5.0$ kpc, the radii of the VHE gamma-ray emission and the X-ray emission are $R_{\rm TeV} = 9.7$ pc and $R_{\rm X} = 3.9$ pc, respectively. The distance from the Galactic center is estimated to be $D_{\rm G} = 6.9$ kpc, thus the energy density of infrared ISRF is assumed to be $U_{\rm IR} = 1.0$ eV cm^{-3}.

Figure 5.15 shows the SED of G54.1+0.3 assuming the type 2 model. Comparison with the model IC spectrum gives the exponential cut-off of $\gamma_1 = 8.0 \times 10^6$, $\gamma_2 = 6.0 \times 10^8$ and the normalization of $N_{\rm e} = 8.0 \times 10^{-7}$ cm^{-3}. Observed X-ray spectrum corresponds to $B_1 =$

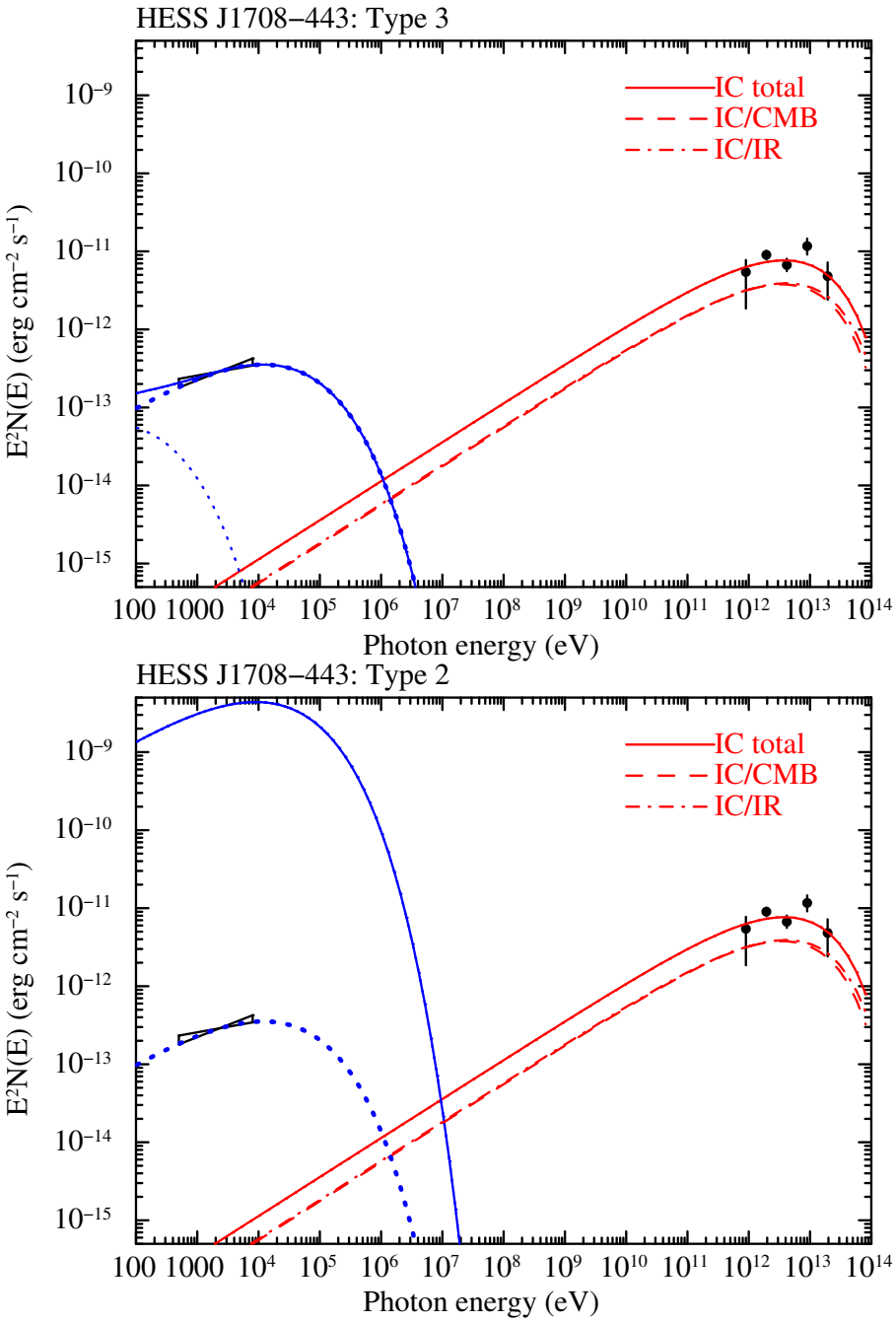

Figure 5.14: Model spectra of HESS J1708–443 overlaid on the observed spectra (Abramowski et al., 2011c; Romani et al., 2005). The red and blue lines indicate IC emission and synchrotron emission, respectively. The dashed line and the dot-dashed line indicate the contribution from CMB and infrared ISRF, respectively. Upper: the type 3 model spectrum is displayed, whose magnetic field strengths are $B_1 < 0.3$ μG and $B_2 = 110$ μG. Lower: the type 2 model spectrum, assuming $B_1 = B_2 = 110$ μG.

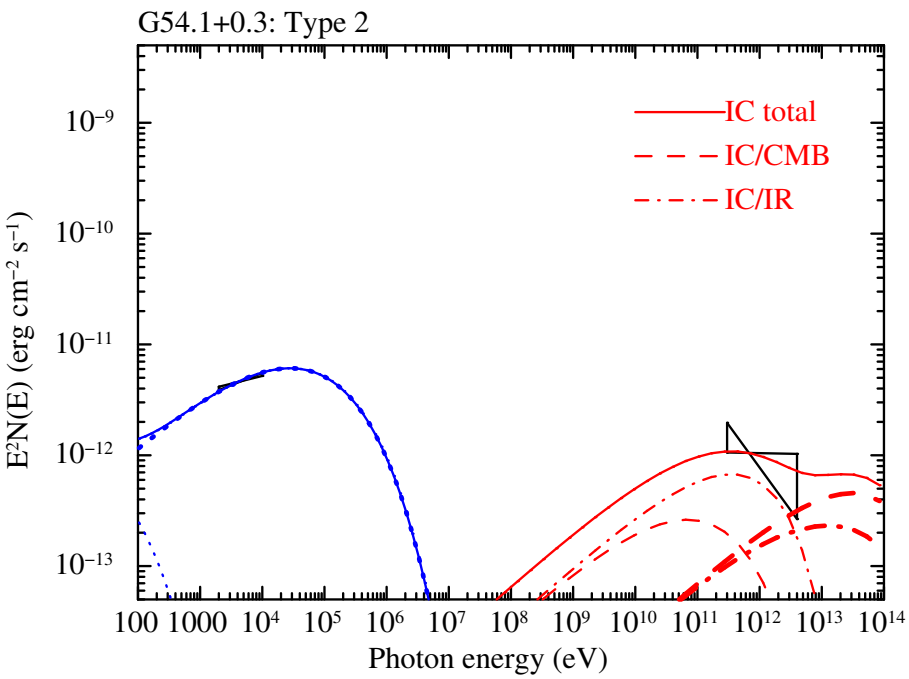

Figure 5.15: The type 2 model spectrum of G54.1+0.3 overlaid on the observed spectra (Acciari et al., 2010; Bocchino et al., 2010). The red and blue solid lines indicate IC emission and synchrotron emission, respectively. The narrow and bold lines indicate the contribution from the electrons with the cut-off energy of γ_1 and γ_2, respectively. The dashed line and the dot-dashed line indicate the contribution from CMB and infrared ISRF, respectively. The dotted line indicates the contribution by the synchrotron radiation.

$B_2 = 5.7\ \mu$G. The resulting total energies are $E_{\rm e} = 1.2 \times 10^{48}$ erg and $E_{\rm B} = 1.4 \times 10^{47}$ erg, respectively.

5.3.14 Kes 75

The VHE gamma-ray emission of Kes 75 (HESS J1846–029) is centered at RA=18h46m23.27s, Dec=–02d58m45s (Terrier et al., 2008). The spectrum of the VHE gamma-ray emission is characterized by a power-law of $\Gamma = 2.3$ and $F_{\rm TeV} = 1.7 \times 10^{-12}$ erg s^{-1} cm^{-2}. According to the VHE gamma-ray image by Terrier et al. (2008), the VHE gamma-ray extent is estimated to be $\sigma_{\rm TeV} = 1'.5$. A radio image of Kes 75 (G29.7–0.3) has a typical size of $3'$ and shows partial shells with flatter spectrum emission from the center (Morsi & Reich, 1987). They are considered thermal shells with a central PWN. The shell is also detected in X-rays with Chandra (Helfand et al., 2003). Because the position of the VHE gamma-ray emission coincides with the PWN, the emission is most likely originated from the PWN. However, because the VHE gamma-ray emission region overlaps with the shell, contribution from the shell cannot

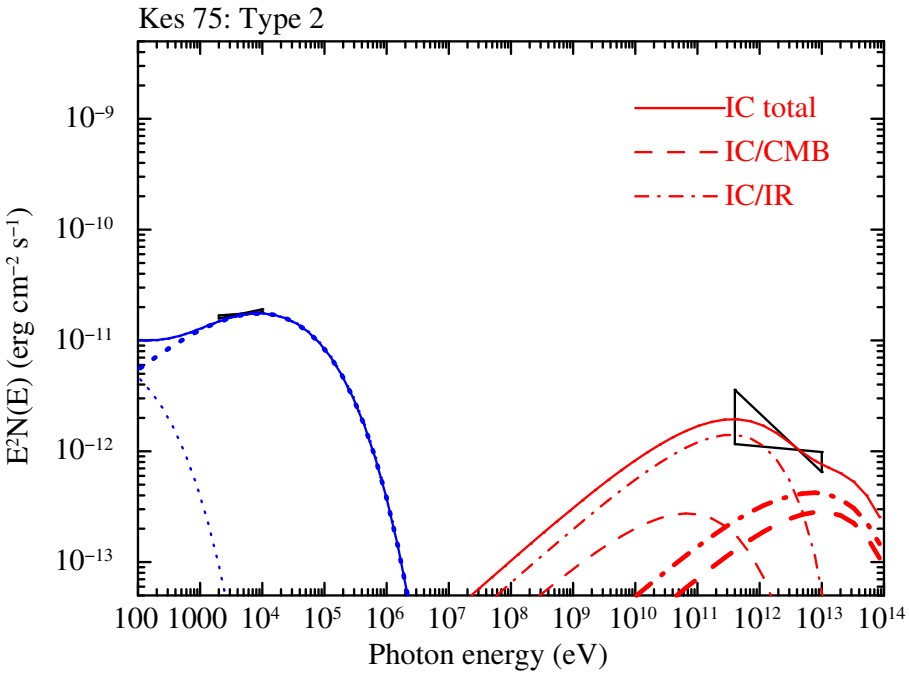

Figure 5.16: The type 2 model spectrum of Kes 75 overlaid on the observed spectra (Terrier et al., 2008; Helfand et al., 2003). The red and blue solid lines indicate IC emission and synchrotron emission, respectively. The narrow and bold lines indicate the contribution from the electrons with the cut-off energy of γ_1 and γ_2, respectively. The dashed line and the dot-dashed line indicate the contribution from CMB and infrared ISRF, respectively. The dotted line indicates the contribution by the synchrotron radiation.

be excluded. PSR J1846–0258 is located at the center of the VHE gamma-ray extent. The pulse period and period derivative of the pulsar are $P = 326$ ms and $\dot{P} = 7.1 \times 10^{-12}$ s s^{-1}, respectively. The distance to the pulsar is estimated to be $d = 5.1$ kpc using the dispersion measure. The spectrum of diffuse X-ray emission is characterized by a power-law of $\Gamma_{\rm X} = 1.92$ and the unabsorbed flux $F_{\rm X} = 2.8 \times 10^{-11}$ erg s^{-1} cm^{-2} (Helfand et al., 2003). The profile was approximated by a Gaussian with $\sigma_{\rm X} = 0'.63$ (Bamba et al., 2010). Based on the distance $d = 5.1$ kpc, the radii of the VHE gamma-ray emission and the X-ray emission are $R_{\rm TeV} = 8.3$ pc and $R_{\rm X} = 3.5$ pc, respectively. The distance from the Galactic center is estimated to be $D_{\rm G} = 4.8$ kpc, thus the energy density of infrared ISRF is assumed to be $U_{\rm IR} = 2.0$ eV cm^{-3}.

Figure 5.16 shows the SED of Kes 75 assuming the type 2 model. Comparison with the model IC spectrum gives the exponential cut-off of $\gamma_1 = 8.0 \times 10^6$, $\gamma_2 = 2.0 \times 10^8$ and the normalization of $N_{\rm e} = 1.5 \times 10^{-6}$ cm^{-3}. Observed X-ray spectrum corresponds to $B_1 = B_2 = 16$ μG. The resulting total energies are $E_{\rm e} = 1.3 \times 10^{48}$ erg and $E_{\rm B} = 6.5 \times 10^{47}$ erg, respectively.

5.3.15 HESS J1813–178

The VHE gamma-ray emission of HESS J1813–178 is centered at RA=18h13m36s, Dec=–17d50m24s, and is extended to $\sigma_{\rm TeV} = 2'.2$ (Funk et al., 2007). The spectrum of the VHE gamma-ray emission is characterized by a power-law of $\Gamma = 2.1$ and $F_{\rm TeV} = 9.0\times10^{-12}$ erg s^{-1} cm^{-2} (Aharonian et al., 2006a). PSR J1813–1749 was found by Gotthelf and Halpern (2009) at the center of the VHE gamma-ray extent. The pulse period and period derivative of the pulsar are $P = 44$ ms and $\dot{P} = 1.5 \times 10^{-13}$ s s^{-1}, respectively. Funk et al. (2007) assumed that the distance is $d = 4$ kpc, thus I also assume the same distance. The spectrum of diffuse X-ray emission is characterized by a power-law of $\Gamma_{\rm X} = 1.9$ and the unabsorbed flux $F_{\rm X} = 6.9 \times 10^{-12}$ erg s^{-1} cm^{-2}. The profile was approximated by a Gaussian with $\sigma_{\rm X} = 0'.35$ (Funk et al., 2007). Based on the assumed distance $d = 4$ kpc, the radii of the VHE gamma-ray emission and the X-ray emission are $R_{\rm TeV} = 8.4$ pc and $R_{\rm X} = 1.2$ pc, respectively. The distance from the Galactic center is estimated to be $D_{\rm G} = 4.7$ kpc, thus the energy density of infrared ISRF is assumed to be $U_{\rm IR} = 2.0$ eV cm^{-3}. Brogan et al. (2005) found a shell-like structure (G12.8–0.0) positionally coincident with HESS J1813–178 in the radio band. The SNR has a typical size of $3'$ and shows non-thermal radio emission. The X-ray image contains a compact core with an extended tail, which may be surrounded by the radio shell. Both X-ray and VHE gamma-ray emission may include the contribution from the SNR shell.

Figure 5.17 shows the SED of HESS J1813–178 assuming the type 3 model (upper panel) and the type 2 model (lower model). If we assume the type 2 model, X-rays are emitted significantly from the outer zone. Thus, I use the type 3 model for this source. Comparison with the model spectrum gives the exponential cut-off of $\gamma_1 = 2.0 \times 10^7$, $\gamma_2 = 1.2 \times 10^8$ and the normalization of $N_{\rm e} = 7.8 \times 10^{-7}$ cm^{-3}. Observed X-ray spectrum corresponds to $B_2 = 42$ μG. The upper limit of the magnetic field strength outside the X-ray emission region is $B_1 < 3.0$ μG. The resulting total energies are $E_{\rm e} = 7.7 \times 10^{47}$ erg and $E_{\rm B} < 3.8 \times 10^{46}$ erg, respectively.

5.3.16 G21.5–0.9

G21.5–0.9 is a composite SNR powered by the pulsar PSR J1833–1034 with a pulse period of $P = 62$ ms and a period derivative of $\dot{P} = 2.0 \times 10^{-13}$ s s^{-1} (Camilo et al., 2006). The distance is estimated to be $d = 4.8$ kpc (Tian & Leahy, 2008). The VHE gamma-ray emission (HESS J1833–105) of G21.5–0.9 is centered at RA=18h33m32.5s, Dec=–10d33m19s (Djannati-Atai et al., 2007). According to the image of Djannati-Atai et al. (2007), its diameter is as small as $0^\circ.2$. Thus, I assume $3\sigma_{\rm TeV} = 0^\circ.1$ in the present analysis. The spectrum of the VHE gamma-ray emission is characterized by a power-law of $\Gamma = 2.1$ and $F_{\rm TeV} = 1.5 \times 10^{-12}$ erg s^{-1} cm^{-2} (Djannati-Atai et al., 2007). The radio image of G21.5–0.9 shows a center-filled morphology

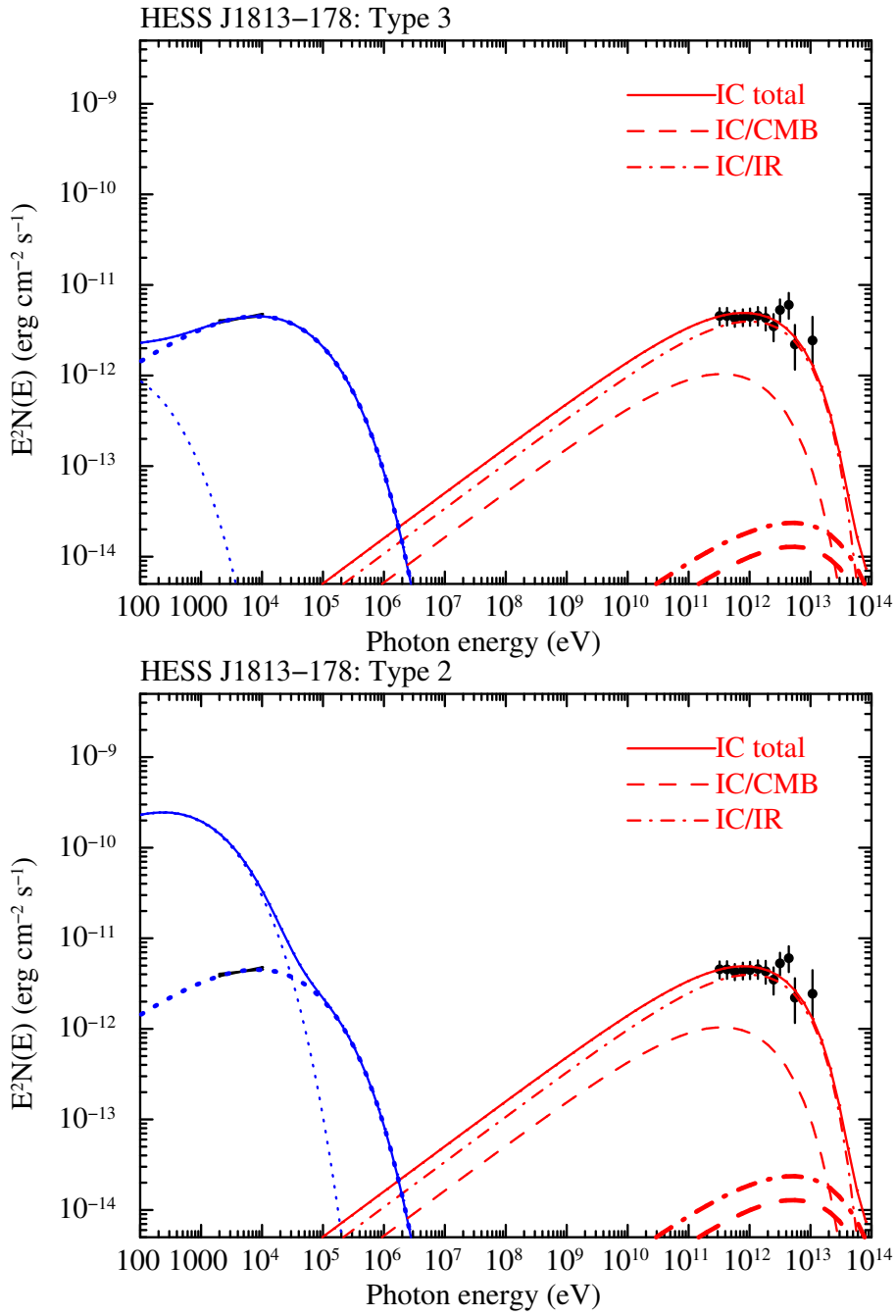

Figure 5.17: Model spectra of HESS J1813–178 overlaid on the observed spectra (Aharonian et al., 2006a; Funk et al., 2007). The red and blue lines indicate IC emission and synchrotron emission, respectively. The dashed line and the dot-dashed line indicate the contribution from CMB and infrared ISRF, respectively. Upper: the type 3 model spectrum is shown, whose magnetic field strengths are $B_1 < 3.0$ μG and $B_2 = 42$ μG. Lower: the type 2 model spectrum, assuming $B_1 = B_2 = 42$ μG.

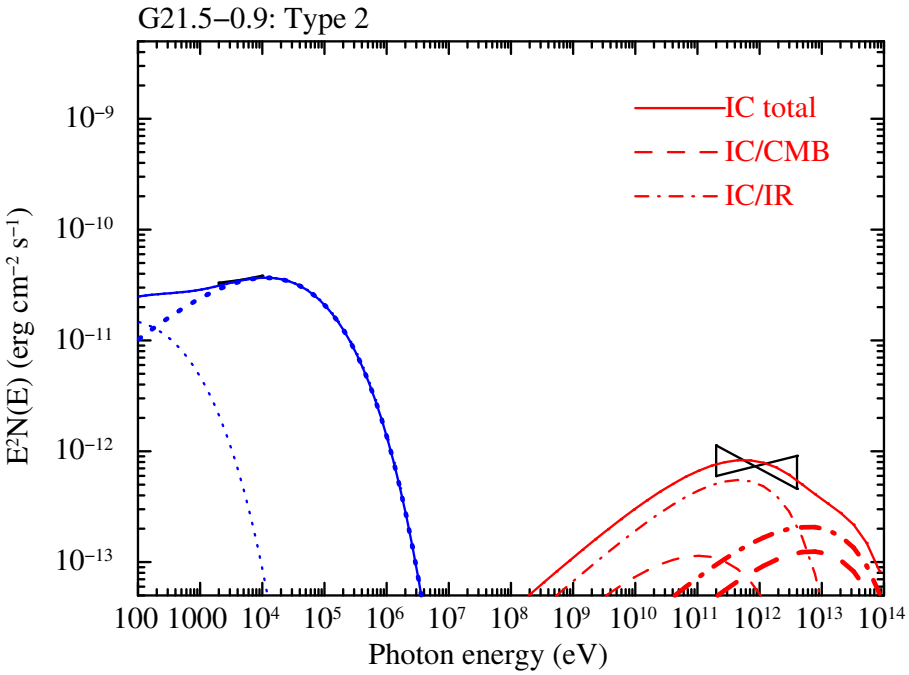

Figure 5.18: The type 2 model spectrum of G21.5–0.9 overlaid on the observed spectra (Djannati-Atai et al., 2007; Tsujimoto et al., 2011). The red and blue solid lines indicate IC emission and synchrotron emission, respectively. The narrow and bold lines indicate the contribution from the electrons with the cut-off energy of γ_1 and γ_2, respectively. The dashed line and the dot-dashed line indicate the contribution from CMB and infrared ISRF, respectively. The dotted line indicates the contribution by the synchrotron radiation.

with an extent of $4'$. The radio emission is dominated by the centrally peaked component, thus the source is classified as a plerion (Reich, 2002). Contribution from the shell to the VHE gamma-ray emission is considered to be small. The spectrum of diffuse X-ray emission is characterized by a power-law of $\Gamma_{\rm X} = 1.9$ and the unabsorbed flux $F_{\rm X} = 5.6\times10^{-11}$ erg s^{-1} cm^{-2} (Tsujimoto et al., 2011). The profile was approximated by a Gaussian with $\sigma_{\rm X} = 0'.72$ (Bamba et al., 2010). Based on the distance $d = 4.8$ kpc, the radii of the IC emission and the synchrotron emission are $R_{\rm TeV} = 7.5$ pc and $R_{\rm X} = 2.7$ pc, respectively. The distance from the Galactic center is estimated to be $D_{\rm G} = 4.8$ kpc, thus the energy density of infrared ISRF is assumed to be $U_{\rm IR} = 2.0$ eV cm^{-3}.

Figure 5.18 shows the SED of G21.5–0.9 assuming the type 2 model. Comparison with the model IC spectrum gives the exponential cut-off of $\gamma_1 = 1.0 \times 10^7$, $\gamma_2 = 1.5 \times 10^8$ and the normalization of $N_{\rm e} = 6.5 \times 10^{-7}$ cm^{-3}. Observed X-ray spectrum corresponds to $B_1 = B_2 = 37\ \mu$G. The resulting total energies are $E_{\rm e} = 4.4\times10^{47}$ erg and $E_{\rm B} = 2.6\times10^{48}$ erg, respectively.

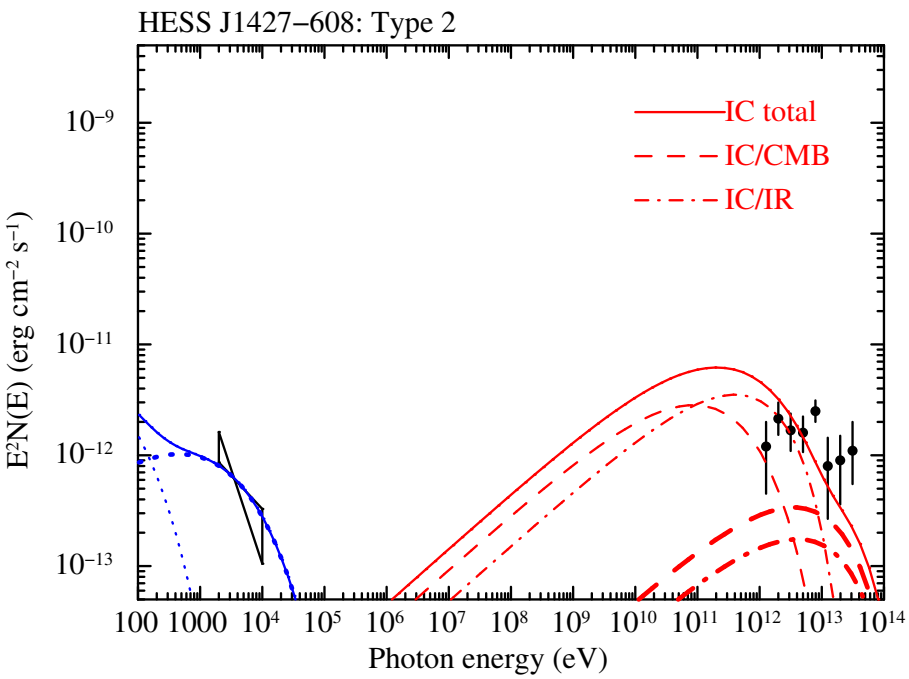

Figure 5.19: The type 2 model spectrum of HESS J1427–608 overlaid on the observed spectra (Aharonian et al., 2008a; Fujinaga et al., 2013). The red and blue solid lines indicate IC emission and synchrotron emission, respectively. The narrow and bold lines indicate the contribution from the electrons with the cut-off energy of γ_1 and γ_2, respectively. The dashed line and the dot-dashed line indicate the contribution from CMB and infrared ISRF, respectively. The dotted line indicates the contribution by the synchrotron radiation.

5.3.17 HESS J1427–608

HESS J1427–608 is a candidate of PWNe, whose energetic pulsar has not been found yet. Detail properties of HESS J1427–608 are described in section 4.2. Based on the assumed distance $d = 8$ kpc, the radii of the IC emission and the synchrotron emission are $R_1 = 31$ pc and $R_2 = 7.9$ pc, respectively. The distance from the Galactic center to HESS J1427–608 is estimated to be $D_{\rm G} = 7.3$ kpc, thus the energy density of infrared ISRF is assumed to be $U_{\rm IR} = 0.5$ eV cm^{-3}.

Figure 5.19 shows the SED of HESS J1427–608 assuming the type 2 model. Comparison with the model IC spectrum gives the exponential cut-off of $\gamma_1 = 9.0 \times 10^6$, $\gamma_2 = 9.0 \times 10^7$ and the normalization of $N_{\rm e} = 5.5 \times 10^{-7}$ cm^{-3}. Observed X-ray spectrum corresponds to $B_1 = B_2 = 4.1$ μG. The resulting total energies are $E_{\rm e} = 2.7 \times 10^{49}$ erg and $E_{\rm B} = 2.4 \times 10^{48}$ erg, respectively.

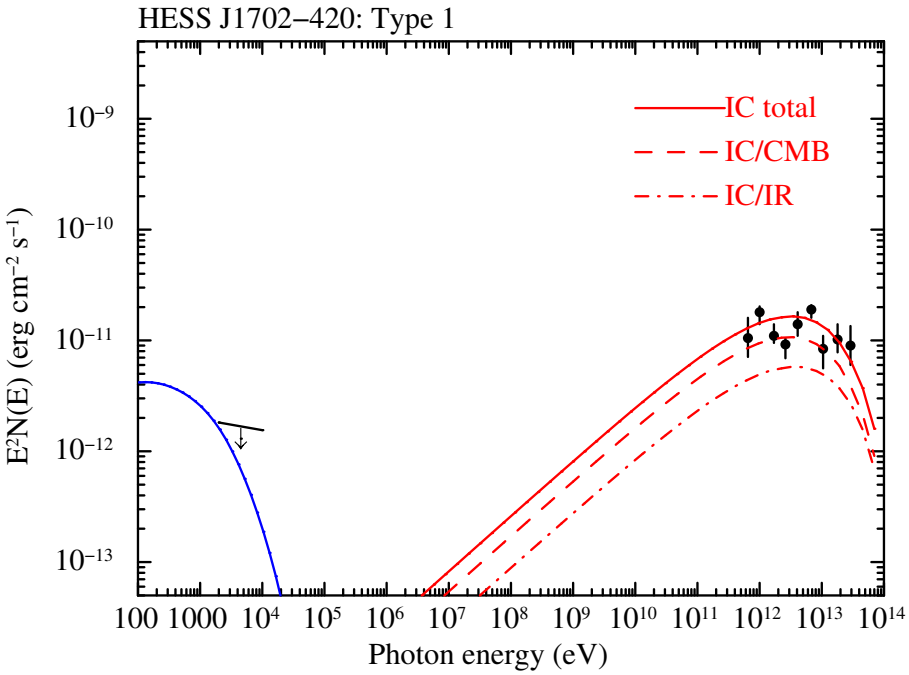

Figure 5.20: The type 1 model spectrum of HESS J1702–420 overlaid on the observed spectra (Aharonian et al., 2008a; Fujinaga et al., 2011). The red and blue lines indicate IC emission and synchrotron emission, respectively. The dashed line and the dot-dashed line indicate the contribution from CMB and infrared ISRF, respectively.

5.3.18 HESS J1702–420

HESS J1702–420 is one of the dark particle accelerators, whose detailed properties are described in section 4.1. I assume the distance is $d = 1$ kpc. The VHE gamma-ray extent is ranging from $15'$ to $30'$. I approximate the VHE gamma-ray size as a sphere with a radius of $r = 21'$. Based on the assumed distance, the radius of the IC emission is $R_{\rm TeV} = 18$ pc. Because the upper limit of the X-ray flux was obtained with the assumption of the same size as VHE gamma-ray, the radius of the synchrotron emission is assumed to $R_1 = R_2 = R_{\rm TeV}$. The distance from the Galactic center to HESS J1702–420 is estimated to $D_{\rm G} = 7.5$ kpc, thus the energy density of infrared ISRF is assumed to be $U_{\rm IR} = 0.5$ eV cm^{-3}.

Figure 5.20 shows the SED of HESS J1702–420 assuming the type 1 model. Comparison with the model spectrum gives the exponential cut-off of $\gamma_1 = \gamma_2 = 8.0 \times 10^7$ and the normalization of $N_{\rm e} = 1.5 \times 10^{-8}$ cm^{-3}. Observed X-ray spectrum corresponds to $B_2 (= B_1) < 1.5$ μG. The resulting total energies are $E_{\rm e} = 1.6 \times 10^{47}$ erg and $E_{\rm B} < 6.2 \times 10^{46}$ erg, respectively.

Chapter 6

Discussion

In chapter 5, I calculated X-ray and VHE gamma-ray spectra of selected sources, mostly PWNe. X-ray and VHE gamma-ray spectra could be reproduced simultaneously for most of the sources with the type 2 model, which considered differences of the size and cut-off energy of the two emission regions. Also, the total energies of electrons and magnetic field were estimated. In this chapter, I first discuss the meaning of the type 2 model. Then, I discuss time evolution of the estimated electron and magnetic field energies for PWNe. Assuming that both the electron and magnetic field energies are injected from the pulsar, I try to estimate the pulse period of the pulsar at birth. Finally, I compare these results of PWNe with those of two sources, HESS J1427–608 and HESS J1702–420, for which the details of analyses are given in chapter 4. whose nature are unclear.

6.1 Interpretation of the Type 2 and 3 Models

Among 16 selected sources, 11 sources could be successfully reproduced with the type 2 model, 2 sources required type 3 model, and I had to use the type 1 model for 3 sources. The reason I had to use type 1 is that the sources are not resolved in the VHE gamma-ray band. Furthermore, the fit was very poor for these three sources. Thus I do not pick up these three sources in the discussion, and I will discuss here the rest of 13 sources fitted with the type 2 and 3 models.

As reviewed in section 2.2, electron energies responsible for synchrotron X-ray emission and inverse Compton scattering to produce VHE gamma-ray emission are different. The former has typical energy of $E_{\rm e}^{\rm syn} \simeq 70$ TeV (equation 2.30) and the latter $E_{\rm e}^{\rm IC} \simeq 20$ TeV (equation 2.31). This leads to the different life times; the former $\tau \simeq 9$ kyr and the latter $\tau \simeq 30$ kyr (equation 2.32). Outside of the X-ray emission region, lower energy electrons (contributing VHE gamma-ray emission) continue to travel until they lose their energy, whereas higher energy electrons (contributing X-ray emission) no longer survive. Thus, the smaller size of the X-ray

emission region ($R_1 > R_2$) may be explained by higher electron energy, which is the same idea as "relic" PWNe (de Jager & Djannati-Ataï, 2009) or "cooled/uncooled electrons" (Mattana et al. (2009), also reviewed in section 2.4.2).

Assuming such a scenario, electrons escape from the termination shock with decreasing their energy. If this is true, the cut-off energy of the electron spectrum decreases with the distance from the pulsar. Position dependence of the cut-off energy may be traced by a spatial variation of photon index in the X-ray and/or VHE gamma-ray band. Taking advantage of high sensitivity of Suzaku X-ray CCD cameras, Kishishita et al. (2012) found a significant spatial variation of $\Gamma_{\rm X}$ in the X-ray nebula of Kookaburra/Rabbit and Kookaburra/K3. On the other hand, Anada et al. (2010) could not find any systematic spatial variation of the spectral slope from HESS J1809–193. Considering low surface brightness of the diffuse X-ray emission in PWNe, it seems not so easy to find a variation of $\Gamma_{\rm X}$. However, my analysis shows that the cut-off energy in the X-ray emission region is always larger than that outside the X-ray emission region, i.e. $\gamma_1 < \gamma_2$ for all the type 2 sources. Thus, the good agreement of the type 2 model spectra with the observed ones is an evidence that electrons travel gradually losing their energy in PWNe after the acceleration at the termination shock.

On the other hand, type 2 model requires no explicit constraint on the magnetic field strength in the VHE gamma-ray emission region (i.e. outer zone). Only the constraint is that no X-ray emission is produced in the outer zone, and same magnetic field as the inner zone satisfies this constraint. However, two cases required weaker magnetic field in the outer zone, thus they required type 3 model. These two sources has very large differences in the size of X-ray and VHE gamma-ray emission regions, a factors of 30 and 8. Furthermore, magnetic fields of the inner region are very large, 110 and 42 μG. These two properties seem to enable me to constrain the magnetic field of the outer zone. If this is a general trend of the PWNe, the magnetic field tends to become weaker as the wind diffuse out from the termination shock. One of the two sources requires weak magnetic field (< 0.3 μG) than the interstellar value. This may not be strange, because PWNe produces a kind of cavity as it diffuse out, in which the pulsar wind and associated magnetic field fills.

6.2 Evolution of Electron and Magnetic Field Energies

As reviewed in chapter 2, activity of the PWN is sustained by the pulsar who releases large amount of energy with the decrease of its spin frequency. The energy may be converted to either the electron energy or the magnetic field energy. I calculated the total electron energy $E_{\rm e}$ and magnetic field energy $E_{\rm B}$ from the model spectrum in the previous chapter. These energies, $E_{\rm e}$ and $E_{\rm B}$, reflect history of the pulsar spin-down. In other words, $E_{\rm e}$ and $E_{\rm B}$ reflect

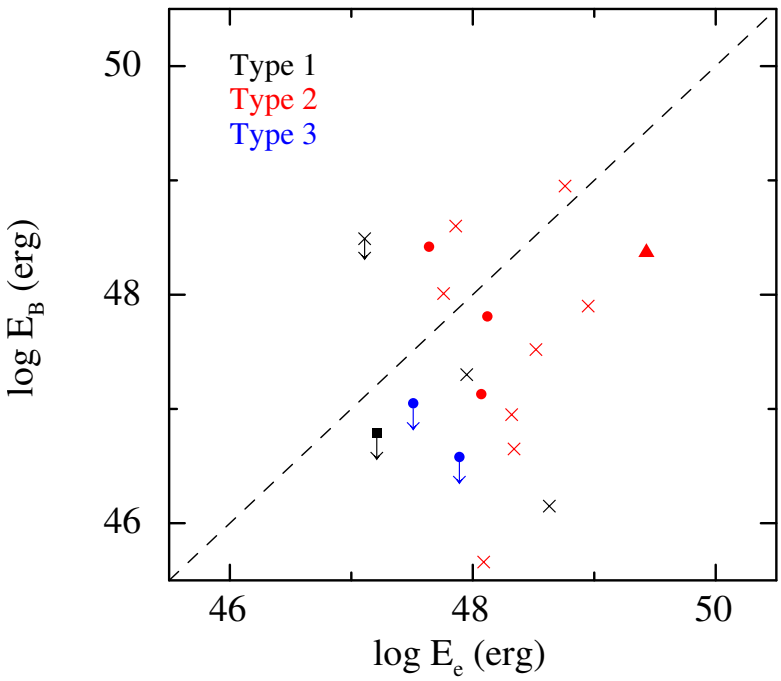

Figure 6.1: Total energies of electrons and magnetic fields are plotted. The crosses and the circles indicate 11 PWNe and 5 composite SNRs, respectively. In addition to these sources, HESS J1427–608 and HESS J1702–420 are also plotted by a triangle and a box, respectively. The dashed line indicates $E_{\rm B} = E_{\rm e}$. Black, red and blue indicate the model of type 1, 2 and 3, respectively.

integrated energy released by the pulsar since its birth.

For the later convenience, I define $E_{\rm e}^{\rm tot}$ and $E_{\rm B}^{\rm tot}$ as the total integrated energies of electrons and magnetic field, respectively, since the birth of the PWN. $E_{\rm B}^{\rm tot}$ and $E_{\rm e}^{\rm tot}$ are represented by $\dot{E}$ and the fraction parameter η $(0 < \eta < 1)$ as

$$E_{\rm B}^{\rm tot} = \eta \int_0^{\tau} \dot{E}(t)dt, \tag{6.1}$$

$$E_{\rm e}^{\rm tot} = (1-\eta) \int_0^{\tau} \dot{E}(t)dt, \tag{6.2}$$

where $t = 0$ corresponds to time when a PWN was born, τ is the age of the pulsar (and the PWN), and $t = \tau$ corresponds to the present time. Here, we assume that η is constant. $E_{\rm B}^{\rm tot}$ and $E_{\rm e}^{\rm tot}$ are in principle different from $E_{\rm B}$ and $E_{\rm e}$ because some of the electron energy is lost as the radiation. The magnetization parameter σ is defined by Kennel & Coroniti (1984) as the ratio of a Poynting flux and a particle energy flux,

$$\sigma = \frac{\dot{E_{\rm B}^{\rm tot}}}{\dot{E_{\rm e}^{\rm tot}}} = \frac{B_{\rm PWN}^2}{4\pi\gamma\rho c^2} = \frac{\eta}{1-\eta}, \tag{6.3}$$

where ρ is a mass density of electrons. The energy ratio is also represented by $E_{\rm B}^{\rm tot}/E_{\rm e}^{\rm tot} =$

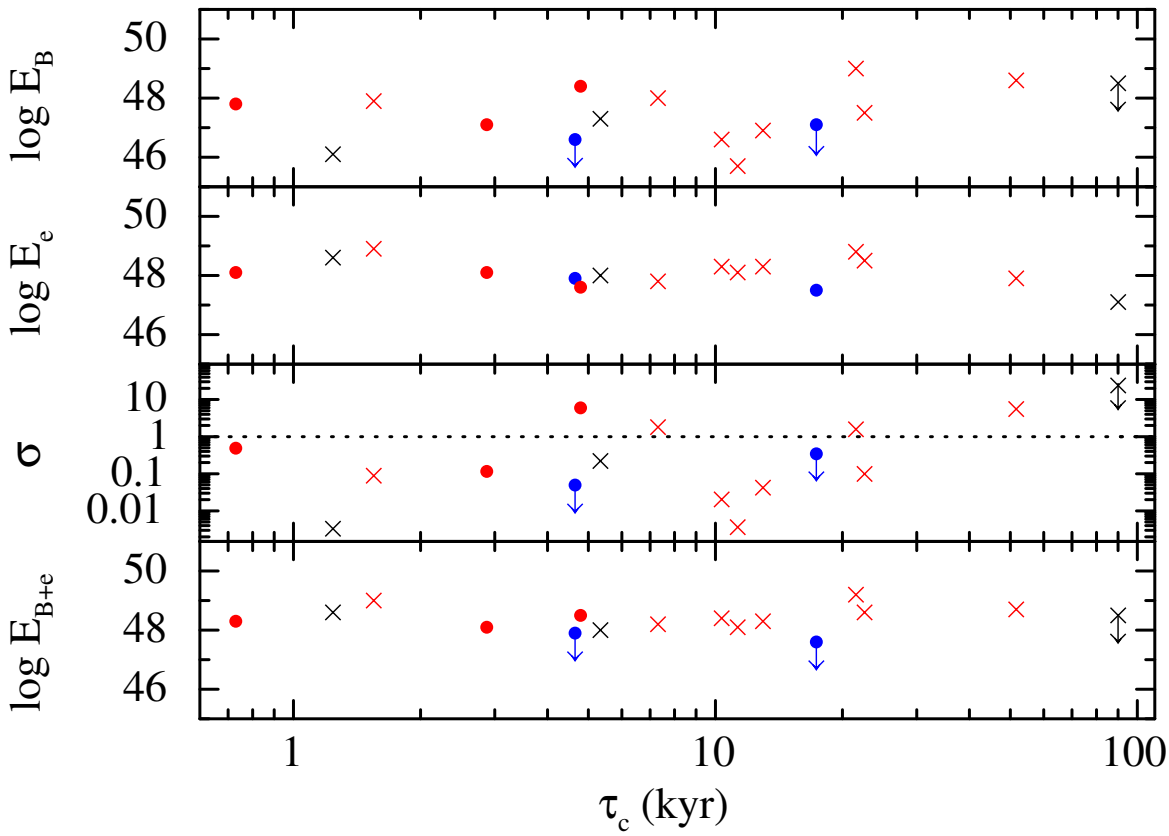

Figure 6.2: Evolution of $E_{\rm B}$ (the top), $E_{\rm e}$ (the second top), σ (the third top) and $E_{\rm B+e}$ (the lowest) are shown as a function of $\tau_{\rm c}$. Symbols are same as figure 6.1; the crosses and the circles indicate 11 PWNe and 5 composite SNRs, respectively. The dotted line in the third panel from the top indicates $\sigma = 1$. Colors are same as figure 6.1; black, red and blue indicate the model of type 1, 2 and 3, respectively.

$\eta/(1-\eta)$, thus

$$\sigma = \frac{E_{\rm B}^{\rm tot}}{E_{\rm e}^{\rm tot}} \simeq \frac{E_{\rm B}}{E_{\rm e}}. \tag{6.4}$$

As reviewed in section 2.3.2, the magnetization parameter is very large just after the launch of the pulsar wind at the pulsar's light cylinder ($\sigma > 10^4$), whereas it is very small just behind the termination shock ($\sigma \ll 1$). Using equation (6.4), the magnetization parameter in the whole nebula can be estimated.

Figure 6.1 shows the total energy distributions of the selected sources. Most of 11 PWNe satisfy $E_{\rm B} \lesssim E_{\rm e}$ except for HESS J1809–193 ($E_{\rm B}/E_{\rm e} = 5.6$). This trend is approximately satisfied even if 5 composite sources (except for G21.5–0.9, $E_{\rm B}/E_{\rm e} = 6.0$) and HESS J1427–608 are included. Thus, I conclude from the spectral calculation that the electron energy is dominated for most of the selected sources.

Figure 6.2 shows evolution of $E_{\rm B}$, $E_{\rm e}$, σ and $E_{\rm B+e} = E_{\rm B} + E_{\rm e}$ as a function of $\tau_{\rm c}$ for 11 PWNe

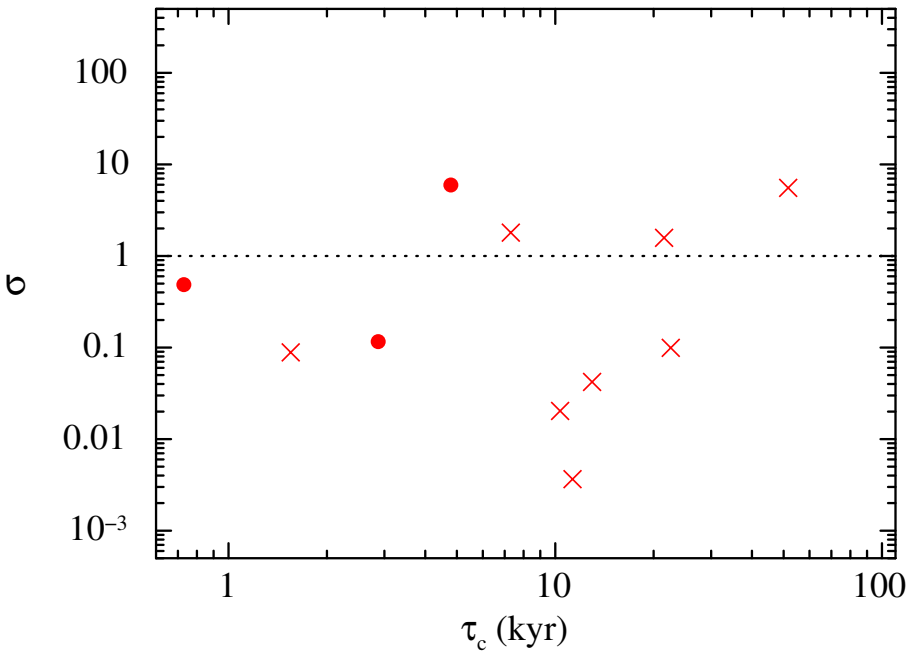

Figure 6.3: The magnetization parameter σ is plotted against the characteristic age of the pulsar, focusing only on the type 2 sources. Symbols are same as figure 6.1; the crosses and the circles indicate PWNe and composite SNRs, respectively.

and 5 composite SNRs. I tested significance of correlation by calculating correlation coefficient focusing only on the type 2 sources, because the spectral fits were very poor for the type 1 sources and the total energy of magnetic field cannot be determined for the type 3 sources. Figure 6.3 shows the σ versus τ_c plot of the type 2 sources. I use a non-parametric method to evaluate the correlation because we cannot assume a normal distribution for the variables and the number of data points are small. One of the non-parametric statistics appropriate to evaluate correlation is the Spearman's correlation coefficient (see appendix A). This is a kind of extension of conventional one (i.e. Pearson's correlation coefficient), and coincide to the Pearson's correlation coefficient when the variables obey the normal distribution. Table 6.1 lists the Spearman's rank correlation coefficient (ρ_s). To evaluate the significance of the Spearman's rank correlation, it is convenient to use the relation that z defined below approximately obey the normal distribution when the correlation of the parent distribution is zero ($\rho_s = 0$) and the number of sample is larger than 10:

$$z = \rho_s \sqrt{n-1}, \tag{6.5}$$

where n is the number of samples ($n = 11$ in the present case). As listed in table 6.1, all combinations show $|z| < z_{90}$, where $z_{90} = 1.64$ is the confidence range of 90% for a normal distribution. Thus, the estimation based on the Spearman's rank correlation coefficients shows

Table 6.1: Spearman's rank correlation coefficients between the energy parameters and τ_c or $\dot{E}$

	$\log \tau_c$		$\log \dot{E}$	
	ρ_s	z	ρ_s	z
$\log E_B$	0.05	0.14	–0.15	–0.49
$\log E_e$	0.13	0.40	–0.27	–0.86
$\log \sigma$	0.01	0.03	–0.15	–0.46
$\log E_{B+e}$	0.35	1.09	–0.21	–0.66

that there is no significant correlation between pulsar's ages and energy parameters. If a PWN gets older, σ is considered to approach $\simeq 1$ to reach equipartition of energy. However, Kes 75 has large value $\sigma \simeq 0.5$ even though it is very young ($\tau_c \simeq 700$ yr). On the other hand, some middle-aged PWNe ($\tau_c \simeq 10$ kyr, e.g., Kookaburra, Vela X) has small values ($\sigma \sim 0.01 - 0.1$). These large variations imply that the magnetization parameter is not simply determined by the characteristic age or spin-down luminosity. If we ignore the radiative loss, the electron and magnetic field energies, E_e and E_B respectively, are expected to increase with the age, as the energy input from the pulsar is accumulated to them. However, no such increasing trend was observed. Thus, it may be considered that the current energy injection from the pulsar is negligible and most of E_e and E_B may have been injected just after the birth of the pulsar. If we assume the magnetic dipole radiation, the energy injection rate depends on the 4th power of the spin frequency. Such a large dependence on the spin frequency may explain the apparent absence of correlation of E_e and E_B with the ages of pulsars.

The characteristic age of a pulsar τ_c does not necesarily reflect the true age of a PWN. Thus I also tested correlation using spin-down luminosity $\dot{E}$, instead of τ_c, as an indicator of the age of PWN. Figure 6.4 shows evolution of E_B, E_e, σ and E_{B+e} with $\dot{E}$. Correlation coefficients are also calculated as listed in table 6.1. Note that $\dot{E}$ tend to decrease in older PWNe (i.e., the larger $\dot{E}$ generally means younger PWNe). As shown in figure 6.4, the evolution is similar to those in the case of τ_c.

6.3 Evolution of Magnetic Field Strength

As discussed in the previous section, the magnetic field energy E_B is not correlated with the characteristic age or the spin-down luminosity. In this section, I focus on the magnetic field strength of type 2 sources. As reviewed in chapter 2, Tanaka & Takahara (2010, 2011) suggested that the increase of a flux ratio F_{TeV}/F_X is due to a decrease of magnetic field strength, not a

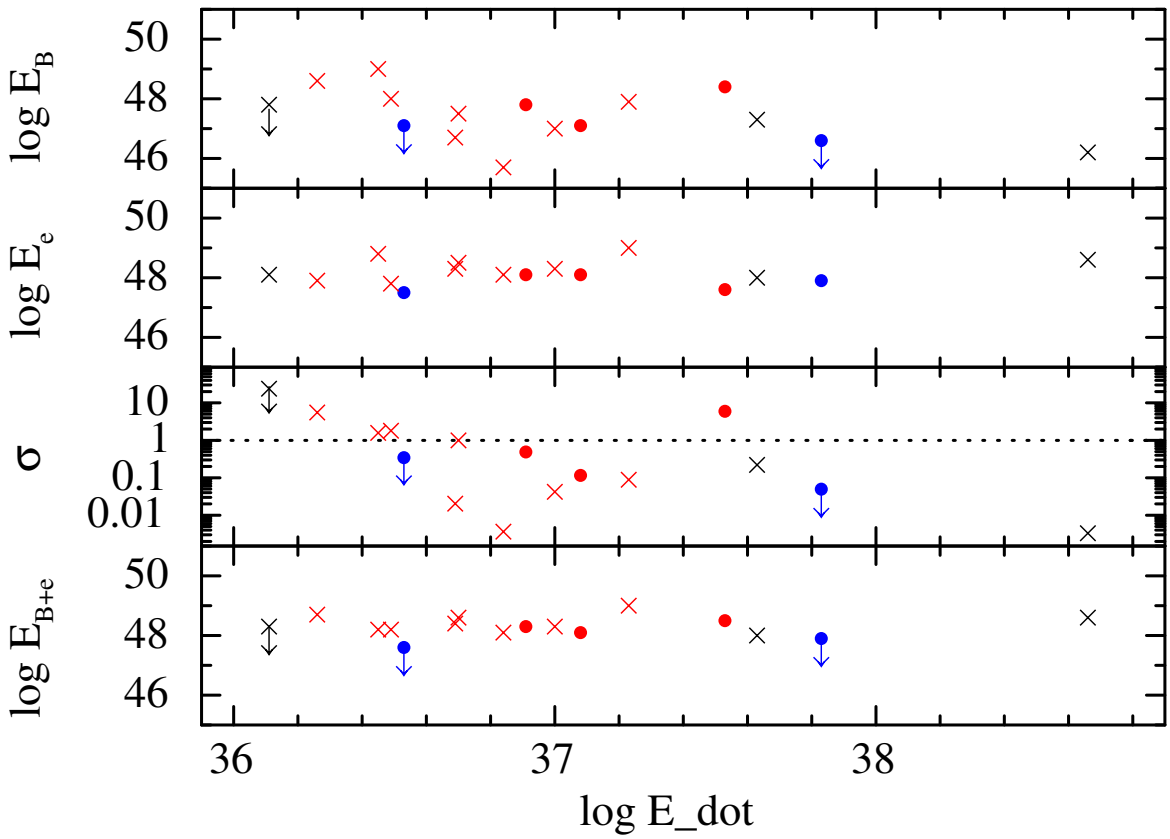

Figure 6.4: Evolution of $E_{\rm B}$ (the top), $E_{\rm e}$ (the second top), σ (the third top) and $E_{\rm B+e}$ (the lowest) as a function of the spin-down luminosity. Symbols are same as figure 6.1, the crosses and the circles indicate 11 PWNe and 5 composite SNRs, respectively. The dotted line in the third panel from the top indicates $\sigma = 1$. Colors are same as figure 6.1; black, red and blue indicate the model of type 1, 2 and 3, respectively.

rapid cooling of X-ray emitting electrons. Bamba et al. (2010) also pointed out that a largely expanded synchrotron X-ray nebula may be achieved with a decrease of magnetic field. If this is true, dark particle accelerators may be explained as an old PWN whose energy density of the magnetic field is much smaller than that of the seed photons scattered by electrons. Figure 6.5 shows evolution of the magnetic field strength $B_1 (= B_2)$. The magnetic field strength shows gradual decrease as PWNe get older. The Spearman's rank correlation coefficient shows significant correlation ($\rho_{\rm s} = -0.63$, $z = -1.98$) within the 95% confidence limit ($z_{95} = 1.96$). Thus, my results support the evolution suggested by Tanaka & Takahara (2010) and Bamba et al. (2010) until $\tau_{\rm c} \simeq 100$ kyr, and dark particle accelerators may be explained as not only old SNRs (Yamazaki et al., 2006) but also old PWNe.

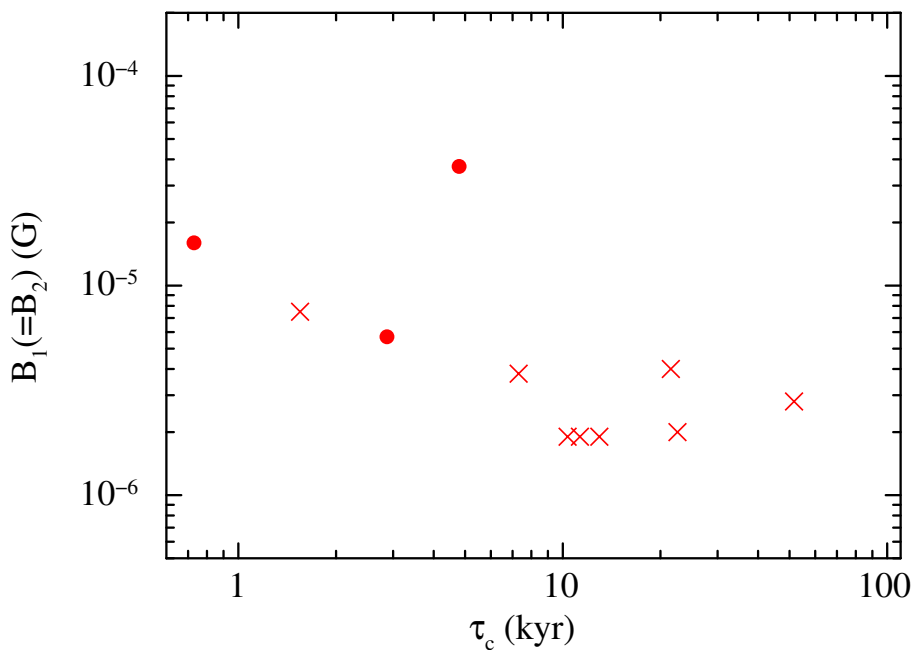

Figure 6.5: Magnetic field strengths $B_1(= B_2)$ of 11 PWNe are plotted against the characteristic age of the pulsar. Same as figure 6.1, the crosses and the circles indicate PWNe and composite SNRs, respectively.

6.4 Estimation of Initial Spin Periods

In the SED calculation, I assumed that the spin-down energy is divided into the magnetic field energy and the electron energy. The total energy $E_{\rm B}^{\rm tot} + E_{\rm e}^{\rm tot}$ may be regarded as the integrated energy so far injected from the pulsar since its birth. Precisely speaking, some fraction of the injected energy was lost as radiation from the PWN. The energy loss by electromagnetic radiation can be estimated using the difference of the cut-off energy between the inner and outer regions (γ_1 versus γ_2), as

$$E_{\rm loss} = \frac{4\pi}{3}(R_1^3 - R_2^3) \times \int_{\gamma_1}^{\gamma_2} N_{\rm e}\gamma^{-p} d\gamma. \tag{6.6}$$

In addition, some fraction of energy may be consumed by the nebula's expansion. If the interstellar space in which the PWN resides is filled by interstellar media with a pressure of $P_{\rm int}$, a PWN needs energy of

$$W = P_{\rm int} \times \frac{4\pi}{3} R_1^3, \tag{6.7}$$

to expand to the current size of the VHE gamma-ray emission region. Here I assume $P_{\rm int} = 1.6 \times 10^{-12}$ dyn cm^{-2}.

I summed up the current rotation energy, the calculated total energies, and the lost energies, as

$$E_0 = E_{\rm rot} + E_{\rm B} + E_{\rm e} + E_{\rm loss} + W, \tag{6.8}$$

Table 6.2: Estimation of the initial rotation energy of PWNe

#	Name	$E_{\rm rot}$	$E_{\rm e}$	$E_{\rm B}$	$E_{\rm loss}$	W	E_0
		10^{47} erg	10^{47} erg	10^{47} erg	10^{47} erg	10^{47} erg	10^{47} erg
1	Vela X	25	12	0.045	0.11	0.50	38
3	HESS J1356–645	7.2	5.7	10	1.1	29	53
4	HESS J1809–193	29	7.2	40	1.3	206	283
5	HESS J1825–137	19	57	90	9.4	226	402
7	MSH 15–52	8.7	89	7.9	14	5.7	125
8	Kookaburra/Rabbit	16	22	0.45	4.1	5.0	48
9	Kookaburra/K3	43	21	0.89	2.8	9.9	87
11	HESS J1837–069	40	33	3.1	6.6	33	117
13	G54.1+0.3	11	12	1.4	2.8	1.7	28
14	Kes 75	1.9	13	6.5	2.3	1.0	25
16	G21.5–0.9	53	4.4	26	0.66	0.77	85

where $E_{\rm rot}$ is the current rotation energy of the pulsar,

$$E_{\rm rot} = \frac{I}{2}\left(\frac{2\pi}{P}\right)^2, \tag{6.9}$$

E_0 is the initial rotational energy of the pulsar and P is the current pulse period. The moment of inertia is assumed to a typical value of $I = 10^{45}$ g cm^2. The initial spin period P_0 can be estimated as

$$P_0 = 2\pi\sqrt{\frac{I}{2E_0}}. \tag{6.10}$$

Using the period derivative $\dot{P}$, P and P_0, the age of the pulsar can be estimated using equation (2.39),

$$\tau = \frac{P}{(n-1)\dot{P}}\left[1 - \left(\frac{P_0}{P}\right)^{n-1}\right], \tag{6.11}$$

where n is the braking index of the pulsar, listed in table 5.2.

To consider the electron energy loss by radiation, I carried out the estimation using the type 2 sources. Table 6.2 lists the estimated energies. Table 6.3 lists the estimated initial spin period. The current pulse periods and the characteristic ages are also listed again. Interestingly, initial spin periods clusters around $\simeq 20 - 90$ ms for most of the sources. If this is true, there may be some mechanism to control the initial spin period during the supernova explosion.

Table 6.3: Estimation of initial spin periods

#	Name	P_0 (ms)	P (ms)	τ (kyr)	τ_c (kyr)
1	Vela X	72	89	4.6	11
3	HESS J1356–645	61	166	6.3	7.3
4	HESS J1809–193	26	83	46	51
5	HESS J1825–137	22	102	21	22
7	MSH 15–52	40	151	1.6	1.6
8	Kookaburra/Rabbit	64	111	6.9	10
9	Kookaburra/K3	51	68	5.8	13
11	HESS J1837–069	41	70	15	23
13	G54.1+0.3	84	136	1.8	2.9
14	Kes 75	89	326	0.78	0.73
16	G21.5–0.9	48	61	2.0	4.8

6.5 The Two unID Sources in the Context of PWNe

In this section, I will discuss nature of the two unID VHE gamma-ray sources in the context of the PWNe, whose X-ray follow-up observation are presented in chapter 4. To examine their nature, I use the characteristics of PWNe obtained so far.

6.5.1 HESS J1427–608

The most plausible nature of HESS J1427–608 is a PWN as discussed in section 4.2, although the associated pulsar has not been found yet. Here I compare the parameters of HESS J1427–608 with those of the PWNe studied so far, and examine the PWN scenario of HESS J1427–608. Its magnetization parameter is $\sigma = 0.088$. The magnetic field strength, $B_1 = B_2 = 4.1$ μG, is also consistent with the age of a few kyr or older. Both results are consistent with a middle aged pulsar. The size of the VHE gamma-ray emission region (31 pc) and that of X-rays (7.9 pc) are large among the samples. This also support the interpretation that the associated pulsar would be relatively old. Because no associated pulsar is found so far, there are two possibilities. One is that the pulsar's beams do not cross our line of sight, and the other is that pulsar has already spun down significantly and does not work as a pulsar any more. I consider the latter possibility rather low. Because the source is emitting X-rays, the pulsar should have been accelerating electrons until recently, at least a few kyrs ago. Otherwise, X-ray emitting electrons were already lost and the source would be dim in X-rays. A pulsar becomes inactive,

once it crosses the so-called the death line, which roughly corresponds to the spin period of $\simeq 4$ sec. However, a pulsar with a spin period of a few tenth seconds, longer end of the spin period distribution of the PWNe, cannot spin down to > 4 sec within a few kyrs if it posses a typical magnetic field for a pulsar. Thus, I consider this possibility rather unlikely. This leaves the other possibility that the pulsar associated to HESS J1427–608 has beams pointing outside our line of sight. If we ignore the current rotation energy of a pulsar, the initial rotation energy corresponds to the sum of $E_{\rm e} + E_{\rm B} + E_{\rm loss} + W \simeq 3.8 \times 10^{49}$ erg, and thus the initial spin period is required to be less than 23 ms.

6.5.2 HESS J1702–420

In the case of HESS J1702–420, available parameters are rather limited as no significant X-ray emission was detected. Thus all the magnetic field related parameters, its strength, total magnetic field energy, magnetization parameter are constrained only with upper limits. The magnetic field strength is smaller than the typical interstellar magnetic field on the Galactic plane ($B \simeq 3 - 10$ μG). The upper limit of the magnetization parameter is rather large and gives effectively no constraint. If we compare other parameters of HESS J1702–420 with those of PWNe, it is immediately realized that the angular size of the source is quite large, as large as $30'$. Together with its brightness in the VHE gamma-ray band, the source may be located close to us rather than being at the distance of 10 kpc. If we assume the source distance to be 1 kpc, rather arbitrarily, as a working hypothesis, the size of the emission region would become comparable to those of PWNe. Total electron energy would be $E_{\rm e} = 1.6 \times 10^{47}$ erg, rather small but compatible with the PWNe. If these parameters are adopted, the source may be similar to HESS J1718–385, for which the associated pulsar is known but only upper limit is obtained for diffuse X-ray emission. The associated pulsar to HESS J1718–385 is old ($\tau_{\rm c} \simeq 90$ kyr) and the spin-down luminosity is small, $\dot{E} = 1.8 \times 10^{36}$ erg s^{-1}. The termination shock of the pulsar wind may be weak and not be able to accelerate electrons high enough to emit X-rays. If this scenario is correct, HESS J1702–420 should be close to us, e.g. at a distance of 1 kpc. Future sensitive radio survey may be able to find the associated pulsar. The pulsar should be rather old and have a spin period around 0.1 sec.

Chapter 7

Conclusion

I studied the nature and evolution of PWNe detected in the VHE gamma-ray band. For this purpose, I examined the wide-band spectra of PWNe in the X-ray and the VHE gamma-ray bands. The analysis was supplemented by an X-ray study of two unID sources discovered in the VHE gamma-ray band.

For the analysis of the two unID sources, the Suzaku satellite was used. A deep observation of HESS J1702–420 was conducted with Suzaku for the first time. However, no X-ray counterpart was detected in the XIS FOV. Considering the systematic error of background subtraction, the upper limit of the X-ray flux was estimated to be $F_{\rm X} < 2.7 \times 10^{-12}$ erg s^{-1} cm^{-2} in the 2–10 keV band for an assumed power-law spectrum of $\Gamma = 2.1$. The large flux ratio $F_{\rm TeV}/F_{\rm X} > 12$ indicates that HESS J1702–420 is a new example of a dark particle accelerator. A significant fraction of VHE gamma-rays may originate from relativistic protons.

I observed the second unID source, HESS J1427–608 also with Suzaku. In the sky field coincident with HESS J1427–608, an extended source was found in the 2–8 keV band, and was designated as Suzaku J1427–6051. It is considered to be an X-ray counterpart of HESS J1427–608. Its radial profile has an extension of $\sigma = 0'.9$ if approximated by a Gaussian. The X-ray spectrum is featureless and heavily absorbed. Using the XMM-Newton archive data, I estimated the contribution from faint X-ray point sources. Seven point sources were found in the Suzaku source region, however, their total flux and absorbing column density are more than an order of magnitude lower than those of Suzaku J1427–6051. Thus, the point sources are not related to Suzaku J1427–6051. The center-filled morphology and featureless X-ray spectrum favor interpretation as a PWN. However, strong evidence supporting a PWN scenario is lacking, i.e. a central pulsar is not detected and the X-ray spectrum is too steep for a PWN.

Next, in order to estimate physical parameters of PWNe, I tried to reproduce the X-ray and the VHE gamma-ray spectra simultaneously for the 16 PWNe with a model as simple as possible. For this purpose, I assumed three types of models for the structure of the emission

regions. For most of the sources, the type 2 model spectrum showed good agreement with the observed spectrum. I obtained the cut-off energy, the normalization of the electron spectrum, and the magnetic field strength by adjusting the model parameters to reproduce the observed spectra. Then, total energies of electrons and the magnetic field were estimated. I found that they have no significant correlation with the ages of the pulsars. The magnetization parameter, defined as the ratio of the magnetic field energy to that of electrons, also has no significant correlation with the ages. On the other hand, I could obtain a marginal evidence to decrease the magnetic field strength with the ages of the PWNe. It is known that the X-ray luminosity of a PWN gradually decreases with the age of the pulsar. This may be explained by either the decrease of magnetic field strength or the rapid cooling of the electrons. The marginal evidence of the magnetic field decrease favors the former interpretation. Furthermore, a dark particle accelerator may be explained by an old PWN, whose magnetic field strength would be very weak and the pulsar would stop working as a pulsar.

Assuming that the rotation energy is divided into the electron and the magnetic field energies, a sum of them can be regarded as the energy that the central pulsar has lost since its birth. Thus, the initial spin period may be estimated by adding the lost energies to the current rotation energy. I summed up the lost energies of the 11 PWNe and found that the initial spin periods are clustered around $\sim 20 - 90$ ms.

Finally, I compared the observational properties of two unID sources with the evolutionary scenario of the PWNe obtained in the current studies. The properties of HESS J1427–608 fit relatively well in the scenario of the PWN evolution. The magnetic field strength is consistent with a PWN aged to a few or a few tens kyr. On the other hand, if HESS J1702–420 is a PWN, it is considered to be very old and to be located close to us. The dark particle accelerators like HESS J1702–420 may be explained by old PWNe.

Appendix A

Correlation Coefficient

A.1 Pearson's Correlation Coefficient

Pearson's correlation coefficient is the parametric statistics most often used to evaluate a linear correlation of data. If the data consist of N pairs of measurements (x_i, y_i), the coefficient r is calculated by

$$r = \frac{N\Sigma x_i y_i - \Sigma x_i \Sigma y_i}{[N\Sigma x_i^2 - (\Sigma x_i)^2]^{1/2}[N\Sigma y_i^2 - (\Sigma y_i)^2]^{1/2}}. \tag{A.1}$$

The value of r ranges from -1 to $+1$. If the data follow a straight line of the form $y = a + bx$, where a and b are constant coefficients, the correlation is said to be perfect, and r becomes ± 1. When there is no correlation, r becomes 0. We need to assume a normal distribution of the variables, when we evaluate the significance of correlation with the Pearson's correlation coefficient.

A.2 Spearman's Rank Correlation Coefficient

Spearman's rank correlation coefficient is the non-parametric method to evaluate a monotonous variation of variables (Spearman, 1904). If the data consist of N pairs of measurements (x_i, y_i), the Spearman's rank correlation coefficient ρ_s is calculated by the following method. First, the rank of x is given as $R(x)$ beginning with the smallest x. By the same way, the rank of y is given as $R(y)$ beginning with the smallest y. Then, calculate the difference between $R(x)$ and $R(y)$, as

$$d_i = R(x_i) - R(y_i). \tag{A.2}$$

ρ_{s} is defined as

$$\rho_{\mathrm{s}} = 1 - \frac{6\Sigma d_i^2}{N(N^2 - 1)}. \tag{A.3}$$

An example data is shown in table A.1, and ρ_{s} for this data set is calculated as $\rho_{\mathrm{s}} = 0.80$.

Table A.1: Example data for the estimation of Spearman's rank correlation coefficient

i	1	2	3	4	5	sum
x	15	13	21	11	19	
y	17	8	20	13	14	
$R(x)$	3	2	5	1	4	
$R(y)$	4	1	5	2	3	
d	-1	1	0	-1	1	0
d^2	1	1	0	1	1	4

Spearman's rank correlation coefficient does not assume any particular distributions (including the normal distribution) of the data. Thus, it can be used even when the distribution of the variables is unknown. If the data obey a normal distribution, it coincides the Pearson's correlation coefficient.

Bibliography

Abdo, A. A., et al. 2010, ApJS, 188, 405

Acciari, V. A., et al. 2010, ApJ, 719, L69

Abramowski, A., et al. 2011a, A&A, 531, L18

Abramowsky, A., et al. 2011b, A&A, 533, A103

Abramowsky, A., et al. 2011c, A&A, 528, A143

Aharonian, F. A., & Atoyan, A. M. 1998, Neutron Stars and Pulsars: Thirty Years after the Discovery, 439

Aharonian, F., et al. 2004a, Nature, 432, 75

Aharonian, F., et al. 2004b, ApJ, 614, 897

Aharonian, F., 2004c, Very High Energy Gamma Radiation (Singapore: World Scientific Publishing), 106

Aharonian, F., et al. 2005a, Science, 307, 1938

Aharonian, F., et al. 2005b, A&A, 435, L17

Aharonian, F., et al. 2005c, A&A, 432, L25

Aharonian, F., et al. 2006a, ApJ, 636, 777

Aharonian, F., et al. 2006b, A&A, 457, 899

Aharonian, F. et al. 2006c, A&A, 448, L43

Aharonian, F., et al. 2006d, A&A, 460, 365

Aharonian, F., et al. 2006e, A&A, 456, 245

Aharonian, F., et al. 2007, A&A, 472, 489

Aharonian, F., et al. 2008a, A&A, 477, 353

Aharonian, F., et al. 2008b, A&A, 490, 685

Aharonian, F., Buckley, J., Kifune, T., & Sinnis, G., 2008c, Reports on Progress in Physics, 71, 096901

Anada, T., et al. 2009a, PASJ, 61, S183

Anada, T., 2009b, PhD thesis, University of Tokyo

Anada, T., et al. 2010, PASJ, 62, 179

Arons, J. 2002, in Neutron Stars in Supernova Remnants, ed. Slane, P. O. & Gaensler, B. M., pp. 71, San Francisco: Astronomical Society of the Pacific

Arons, J. 2004, Advances in Space Research, 33, 466

Atoyan, A. M., & Aharonian, F. A. 1996, MNRAS, 278, 525

Balbo, M., Saouter, P., Walter, R., Pavan, L., Tramacere, A., Pohl, M., & Zurita-Heras, J. -A. 2010, A&A, 520, A111

Bamba, A., Koyama, K.,& Tomida, H. 2000, PASJ, 52, 1157

Bamba, A., Ueno, M., Koyama, K., & Yamauchi, S., 2001, PASJ, 53, L21

Bamba, A., et al. 2007, PASJ, 59, S209

Bamba, A., et al. 2009, ApJ, 691, 1854

Bamba, A., et al. 2010, ApJ, 719, L116

Bell, A. R. 1978, MNRAS, 182, 147

Bernlöhr, K., et al. 2003, Astroparticle Physics, 20, 111

Blandford, R. D., & Ostriker, J. P. 1978, ApJ, 221, L29

Blumenthal, G. R., & Gould, R. J. 1970, Reviews of Modern Physics, 42, 237

Bocchino, F., Bandiera, R., & Gerfand, J. 2010, A&A, 520, A71

Brogan, C. L., et al. 2005, ApJ, 629, L105

Camilo, F., et al. 2002, ApJ, 574, L71

Camilo, F., et al. 2004, ApJ, 611, L25

Camilo, F., et al. 2006, ApJ, 637, 456

Camilo, F., Ransom, S. M., Gansler, B. M., & Lorimer, D. R. 2009, ApJ, 700, L34

Chang, C., Konopelko, A., & Cui, W. 2008, ApJ, 682, 1177

Cocke, W. J., Disney, M. J., & Taylor, D. J. 1969, Nature, 221, 525

Daum, A., et al. 1997, Astroparticle Physics, 8, 1

Davies, B., et al. 2008, ApJ, 676, 1016

de Jager, O. C., & Djannati-Ataï, A. 2009, in Neutron Stars and Pulsars, ed. W. Becker (Berlin: Springer), 451

Djannati-Ataï, A., de Jager, O. C., Terrier, R., Gallant, Y. A., & Hoppe, S. 2007, proceedings of the 30th ICRC, arXiv:0710.2418

Dodson, R. & Golap, K. 2002, MNRAS, 334, L1

Dodson et al. 2003, ApJ, 596, 1137

Dubner, G. M., Moffett, D. A., Goss, W. M., & Winkler, P. F. 1993, AJ, 105, 2251

Eger, P., Domainko, W., & Clapson, A.-C. 2010, A&A, 513, A66

Fukazawa, Y., et al. 2009, PASJ, 61, S17

Fujinaga, T., et al. 2011, PASJ, 63, S863

Fujinaga, T., et al. 2013, PASJ, 65, in press

Fujita, Y., Hayashida, K., Takahashi, H., & Takahara, F. 2009, PASJ, 61, 1229

Funk, S. et al. 2007, A&A, 470, 249

Gaensler, B. M., et al. 2002, ApJ, 569, 878

Gaensler, B. M. & Slane, P. O. 2006, ARAA, 44, 17

Gallant, Y. A. 2007, Ap&SS, 309, 197

Garmire, G. P. 1997, BAAS, 190, 34.04

Gold, T. 1969, Nature, 221, 25

Goldreich, P., & Julian, W. H. 1969, ApJ, 157, 869

Gotthelf et al. 2002, ApJ, 567, L125

Gotthelf, E. V. and Halpern, J. P. 2008, ApJ, 681, 515

Gotthelf, E. V. and Halpern, J. P. 2009, ApJ, 700, L158

Green, A. J., Cram, L. E., Large, M. I., & Ye, T. 1999, ApJS, 122, 207

Green, D. A. 2004, Bull. Astr. Soc. India, 32, 335

Green, D. A. 2009, Bull. Astr. Soc. India, 37, 45

Guseinov, O. H., Yerli, S. K., Ozkan, S., Sezer, A., & Tagiyeva, S. O. 2004, Astronomical and Astrophysical Transactions, 23, 357

Helfand, D. J., Collins, B. F., & Gotthelf, E. V. 2003, ApJ, 582, 783

Hess, V. F. 1912, Phys. Zeits., 13, 1084

Hester, J. J. 2008, ARA&A, 46, 127

Hillas, A. M. 1996, Space Science Review, 75, 17

Hinton, J. A. 2007, ArXiv e-prints, 712, arXiv:0712.3352

Hinton, J. A., et al. 2007, A&A, 476, L25

Hinton, J. A., et al. 2009, ApJ, 690, L101

Hofmann, W. 2001, Proc. of the 27th International Cosmic Ray Conference, Hamburg, 2001, M. Simon, E. Lorenz, M. Pohl (Eds.), pp. 2785

Holder, J., et al. 2008, in AIP Conf. Proc., 1085, 657

Ishisaki, Y., et al. 2007, PASJ, 59, S113

Jansen, F., et al. 2001, A&A, 365, L1

Johnston, S., et al. 1992, MNRAS, 255, 401

Kalberla, M., et al. 2005, A&A, 440, 775

Kargaltsev, O., Pavlov, G. G., & Wong, J. A. 2008, arXiv:0805.1041

Kargaltsev, O., & Pavlov, G. G. 2008, in AIP Conf. Proc., 983, 40 Years of Pulsars: Millisecond Pulsars, Magnetars and More, ed. Bassa et al. (New York: AIP), 171

Kaspi, V. M., Roberts, M. S. E., & Harding, A. K. 2006, in Compact Stellar X-ray Sources, ed. W. Lewin, M. van der Klis. (Cambridge: Cambridge University Press), 279

Kataoka, J. PhD thesis, University of Tokyo, 2000

Kennel, C. F., & Coroniti, F. V. 1984, ApJ, 283, 694

Kirsch, M. G., et al. 2005, Proc. SPIE, 5898, 224

Kishishita, T. et al. 2012, ApJ, 750, 162

Kokubun, M., et al. 2007, PASJ, 59, S53

Koyama, K., Awaki, H., Kunieda, H., Takano, S., & Tawara, Y. 1989, Nature, 339, 603

Koyama, K., Petre, R., Gotthelf, E. V., Hwang, U., Matsuura, M., Ozaki, M., & Holt, S. S. 1995, Nature, 378, 255

Koyama, K., Kinugasa, K., Matsuzaki, K., Nishiuchi, M., Sugizaki, M., Torii, K., Yamauchi, S., & Aschenbach, B. 1997, PASJ, 49, L7

Koyama, K., et al. 2007, PASJ, 59, S23

Kushino, A., Ishisaki, Y., Morita, U., Yamasaki, N. Y., Ishida, M., Ohashi, T., & Ueda, Y. 2002, PASJ, 54, 327

LaMassa, S. M., Slane, P. O., & de Jager, O. C. 2008, ApJ, 689, L121

Lyne, A. G., Pritchard, R. S., & Graham-Smith, F. 1993, MNRAS, 265, 1003

Lyne, A. G., Pritchard, R. S., Graham-Smith, F., & Camilo, F., 1996, Nature, 381, 497

Livingstone, M. A., Kaspi, V. M., & Gavriil F. P. 2005, ApJ, 633, 1095

Livingstone, M. A., Kaspi, V. M., Gavriil, F. P., Manchester, R. N., Gotthelf, E. V. G., Kuiper, K., 2007, Ap&SS, 308, 317

Livingstone, M. A., Kaspi, V. M., 2011, ApJ, 742, 31

Manchester, R. N., & Taylor, J. H. 1977, Pulsars (San Francisco: Freeman)

Manchester, R. N., Hobbs, G. B., Teoh, A., & Hobbs, M. 2005, AJ, 129, 1993

Matsumoto, H., et al. 2007, PASJ, 59, S199

Mattana, F., et al. 2009, ApJ, 694, 12

Melatos, A. 1998, Mem. Soc. Astron. It., 69, 1009

Mitsuda, K., et al. 2007, PASJ, 59, S1

Morsi, H. W. & Reich, W. 1987, A&AS, 71, 189

Nakamura, R., et al. 2009, PASJ, 61, S197

Nakamura, R., Bamba, A., Dotani, T., Ishida, M., Yamazaki, R., & Kohri, K. 2012, ApJ, 746, 134

Nolan, P. L., et al. 2012, ApJS, 199, 31

Pacini, F., & Salvati, M. 1973, ApJ 186, 249

Prigozhin, G., Burke, B., Bautz, M., Kissel, S., Lamarr, B. 2008, IEEE Transactions on Electron Devices, 55, 2111

Porquet, D., et al. 2003, A&A, 401, 197

Porter, T. A., Moskalenko, I. V., & Strong, A. W., 2006, ApJ, 648, L29

Punch, M., 2001, Proc. of the 27th International Cosmic Ray Conference, Hamburg, 2001, M. Simon, E. Lorenz, M. Pohl (Eds.), 2814

Ray, P. S., et al. 2011, ApJS, 194, 17

Rees, M. J., & Gunn, J. E. 1974, MNRAS, 167, 1

Reich, W. 2002, proceedings of the 270th WE-Heraeus Seminar on "Neutron Stars, Pulsars and Supernova Remnants", eds. W. Becker, H. Kesch, & J. Truemper, MPE report 278, pp. 1–12

Revnivtsev, M., Sazonov, S., Gilfanov, M., Churazov, E., & Sunyaev, R. 2006, A&A, 452, 169

Richards, D. W., & Comella, J. M. 1969, Nature, 222, 551

Rishbeth, H. 1958, Australian Journal of Physics, 11, 550

Romani, R. W., Ng, C.-Y., Dodson, R., & Brisken, W., 2005, ApJ, 631, 480

Roy, J., Gupta, Y, & Lewandowski, W., 2012, MNRAS, 424, 2213

Rybicki, G. B., & Lightman, A. P. 1979, New York, Wiley-Interscience, 1979. 393

Serlemitsos, P., et al. 2007, PASJ, 59, S9

Slane, P., Hughes, J. P., Edgar, R. J., Plucinsky, P. P., Miyata, E., Tsunemi, H., & Aschenbach, B. 2001, ApJ, 548, 814

Sokolsky, P. 1989, Frontiers in Physics, 76

Spearman, C. 1904, The American Journal of Psychology, 15, 72

Staelin, D.H., & Reifenstein, E. C. III. 1968, Science, 162, 1481

Stephenson, F. R, & Green, D. A. 2002. Historical Supernovae and Their Remnants (Oxford: Oxford University)

Strüder, L., et al. 2001, A&A, 365, L18

Takahashi, T., et al. 2007, PASJ, 59, S35

Tanaka, S. J., & Takahara, F. 2010, ApJ, 715, 1248

Tanaka, S. J., & Takahara, F. 2011, ApJ, 741, 40

Tawa, N., et al. 2008, PASJ, 60, S11

Tian, W. W., & Leahy, D. A. 2008, MNRAS, 391, L54

Trimble, P. 1973, PASP, 85, 279

Terrier, R., et al. 2008, proc. 4th meeting on High Energy Gamma-ray Astronomy, AIP 1085, 316

Tsujimoto, M., et al. 2011, A&A, 525, 25

Turner et al. 2001, A&A, 365, L27

Uchiyama, H., et al. 2009a, PASJ, 61, S9

Uchiyama, H., et al. 2009b, PASJ, 61, S189

Uchiyama, Y., et al. 2008, PASJ, 60, S35

Velusamy, T. & Becker, R. H. 1988, AJ, 95, 1162

Weekes, T. C., et al. 1989, ApJ, 342, 379

Weekes, T. C. 1996, Space Science Review, 75, 1

Weisskopf, M. C., Tananbaum, H. D., Van Speybroeck, L. P., & O'Dell, S. L. 2000a, in J. E. Truemper and B. Aschenbach (eds.), Proc. SPIE, 4012, 2

Weisskopf, M. C., et al. 2000b, ApJ, 536, L81

Yamauchi, S., et al. 2009, PASJ, 61, S225

Yamazaki, R., Kohri, K., Bamba, A., Yoshida, T., Tsuribe, T., & Takahara, F. 2006, MNRAS, 371, 1975

Yuasa, T., et al. 2008, PASJ, 60, S207

Acknowledgement

Advisors of Docter Thesis

- Professor Tadayasu Dotani: I am grateful to give me opportunity of studying at ISAS/JAXA. I am happy that Dotani-sensei allowed me to experience various activities including this work.
- Dr. Aya Bamba at Aoyama Gakuin University: strongly supported my studies for five years.

Powerful Supporters of Docter Thesis

- Dr. Masanobu Ozaki: many thanks! Ozaki-san kindly helped and encouraged me every day.
- Dr. Koji Mori at University of Miyazaki: I am pleased to discover Suzaku J1427–6051 together.

Other Members of Dotani Laboratory
Mr. Chikara Natsukari, Dr. Keiko Matsuta, Dr. Takayasu Anada, Mr. Kazuma Shimizu, Mr. Masachika Iwai, Mr. Masaharu Izawa, Mr. Keisuke Kondo & Ms. Aya Koyama

Other Supporters
Mr. Shoichi Kimura at University of Miyazaki, Professor Gerd Pühlhofer at Universität Tübingen, Suzaku Team, XMM-Newton Team, Chandra Team, H.E.S.S. Collaboration, & VERITAS Team.

SXI Collaborators; SXI was another important work in my PhD life.

- Osaka University: Dr. Naohisa Anabuki, Professor Hiroshi Tsunemi, Dr. Kiyoshi Hayashida, Dr. Hiroshi Nakajima, Mr. Shutaro Ueda & many
- University of Miyazaki: Dr. Makoto Yamauchi, Mr. Shoichi Aoyama, Mr. Yusuke Nishioka, Mr. Taku Murayoshi, Mr. Satoshi Oura, Mr. Junpei Nagai, Mr. Yusuke Koura & many
- Kogakuin University: Dr. Takayoshi Kohmura, Mr. Shoma Ikeda, Mr. Kenta Kaneko & many
- The University of Tokyo: Dr. Junko Hiraga
- Yokohama National University: Mr. Hidenori Kawano & many
- Rikkyo University: Dr. Hiroshi Murakami
- Tsukuba Space Center (TKSC), JAXA: Dr. Hiroshi Tomida & Dr. Masashi Kimura
- Kyoto University: Professor Takeshi Tsuru, Dr. Hiroyuki Uchida & many

I hope ASTRO-H/SXI will be succeeded and bring us lots of new discoveries in Astrophysics.

Special Thanks to Mr. Kei Saitou at JMA, my parents, my sister & Ms. Mika Mori.

Financial Supports

- Japan Society for the Promotion of Science (JSPS) young research fellowship, no. 23-9676
- The Global Center of Excellence Program by Ministry of Education, Culture, Sports, Science and Technology (MEXT), Japan, through the "Nanoscience and Quantum Physics" project of the Tokyo Institute of Technology
- Research Assistant at Japan Aerospace Exploration Agency
- International Physics Leadership Program, Tokyo Institute of Technology

I am grateful to all of people supporting my graduate university life. Thank you so much.

Takahisa Fujinaga